THERMO-HYDRO-MECHANICAL COUPLED ANALYSIS IN LOW PERMEABILITY MEDIA UNDER NUCLEAR REPOSITORY CONDITIONS

A Thesis

by

FERNANDO LUIS APONTE RIVERA

Submitted to the Office of Graduate and Professional Studies of
Texas A&M University
in partial fulfillment of the requirements for the degree of

MASTER OF SCIENCE

Chair of Committee,	Marcelo Sánchez
Committee Members,	Charles Aubeny
	Eduardo Gildin
Head of Department,	Robin Autenrieth

December 2013

Major Subject: Civil Engineering

ABSTRACT

The design of underground repositories to storage high level radioactive waste is based on the multi barrier concept that consists of placing natural and artificial barriers around the radioactive material for isolation. The artificial barrier is commonly made of expansive clay (e.g. bentonite) that is subjected to heating and hydration resulting in Thermo-Hydro-Mechanical (THM) coupled phenomena. Experimental evidence has shown an important reduction in the hydration rate of the clay at advanced stages of infiltration tests under non-isothermal conditions. Traditional models have had problems to properly reproduce the hydraulic behavior observed in some experiments, overestimating the hydration rate and underestimating the time required to reach fully saturation conditions.

This thesis presents THM modeling of the FEBEX bentonite based on a mathematical framework suitable for problems in low permeability media. In addition, phenomena not included in traditional models like the threshold hydraulic gradient, thermo-osmosis and double structure are incorporated in the proposed framework to explain the reduction in the hydration rate.

In order to assess the performance of the models, infiltration laboratory tests performed under isothermal and non isothermal conditions and the mock-up large scale test carried out by CIEMAT, are presented. Additionally, a synthetic in-situ exercise sponsored by the eFEBEX project to study the THM evolution of a full scale bentonite buffer under typical repository conditions is also discussed. All numerical simulations

were carried out with the finite element program CODE_BRIGHT and divided into four cases: a reference case, (based on the standard THM formulation) and the other three correspond to advance model incorporating the following phenomena: the threshold hydraulic gradient, thermo-osmosis and double structure effects.

The models incorporated in the existing THM formulation enable the improvement of numerical predictions of the experimental data obtained from the infiltration tests and mock-up experiment by reproducing the reduction in the hydration rate inside the bentonite. It has been observed that the double structure model that considers the two dominant pore levels and material fabric changes in the FEBEX bentonite provided a more satisfactory reproduction of the long-term experimental results.

ACKNOWLEDGEMENTS

I would like to express my gratitude to all the people that in some way helped me during my years as a graduate student at Texas A&M University. First of all, I like to thank my advisor and committee chair, Dr. Marcelo Sánchez, for giving me the opportunity to work in this project and for his guidance and support throughout the course of this research. It has been an enriching learning experience that contributed to my professional growth. Also, I want to thank Dr. Giovanna Biscontin for helping me to obtain the financial aid for my last year of studies with the award of the Peter C Foster Fellowship. This award was very important to me because not only helped me financially but also motivated me to continue with my goal of completing my Master's degree. In addition, I want to thank all the professors that through their courses I had the opportunity of expanding my knowledge in different areas of Geotechnical Engineering. A special mention goes to: Dr. Jean-Louis Briaud, Dr. Charles Aubeny, Dr. Zenon Medina-Cetina and Dr. Robert Lytton.

It is important to recognize the work done by the ENRESA and CIEMAT team in the past years. Their experimental work on the FEBEX project has been relevant to perform the numerical analysis presented in this thesis. Another recognition goes to Maria Villar for her interest and support by providing the data necessary to complete this project.

My appreciation goes to all my classmates that joined me during this part of my professional career. I would like to thank Axel Montalvo for convincing me to come to

TAMU and be part of this great program of study. Thank you for motivating me despite my financial issues. Also, I want to mention some of my classmates that joined me during this journey: Rehan Khan, Mackenzie Garton, Randal Hartsfield, Patricia Varela, Shola, Adam White, Ivonne Romero, Marcus Rasulo, Mojdeh, Francisco Grajales, Mehdi, Mohsen and Gang. It was a pleasure to meet you and shared ideas with you during our problem solving discussions. Another mention goes to my research group mates: Lakshman Dontha and Ajay Shastri. I really appreciated your help clarifying my doubts with CODE_BRIGHT and other concepts related to my research.

Finally, I would like to thank my family for their unconditional support during my time as a graduate student. My gratitude goes to my parents Fernando Aponte and Linda Rivera that regardless of the distance that separated us, their love and support always motivated me to keep working on my graduate studies. To my wife, Ivonne Andujar, who has been always there for me, I would like to dedicate this thesis. Thank you for your love, support and patience throughout this process.

TABLE OF CONTENTS

Page

Page

LIST OF FIGURES

Page

Page

Page

Page

Page

Page

Page

Page

Page

LIST OF TABLES

Page

Page

Page

1. INTRODUCTION

1.1 Background And Significance

According to the International Atomic Energy Agency (IAEA), in 2002 nuclear power accounted for an electricity production of 2574 TWh, nearly 16 % of the total electricity generated in the world and about 30 % in OECD European countries. The increase in nuclear power generation has largely arisen from improved plant productivity rather than from new facilities coming into operation (Gens, 2003). In many countries around the world where nuclear power production takes place, the power generation involves the following operations: extraction of mineral ores with fissile materials (e. g. uranium), chemical purification & fuel manufacturing, reactor operation and spent fuel management as Figure 1.1 shows. The mentioned operations give rise to radioactive wastes that must be disposed in an adequate manner. The waste management problem is typically approached by the concentration and isolation of contaminants especially for high level nuclear waste (HLW). Several procedures have been considered to address the problem of radioactive waste disposal. These procedures include: space disposal, ice sheet disposal, ocean bed disposal, disposal beneath the seabed, nuclear transmutation and geological disposal (Gens, 2003). However, deep geological disposal is an intensively studied option for long term confinement of heat emitting, high level nuclear waste.

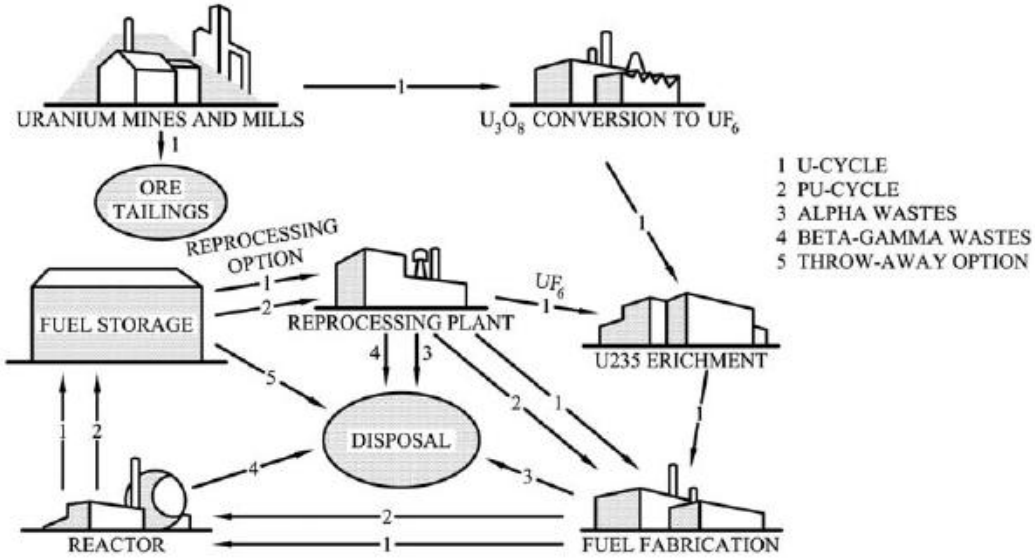

Figure 1.1. Nuclear fuel cycle and principal radioactive wastes generated. (Chapman and McKinley, 1987)

The construction of deep repositories will involve the excavation of series of tunnels through the host rock a few hundred meters below the ground surface (Figure 1.2). The design of these repositories to storage the nuclear waste, resort to the multi-barrier concept to achieve the required degree of waste isolation. This concept is based on placing several barriers, both natural and artificial between the potentially harmful waste and the environment. The natural barrier is the host rock and the artificial barriers consisted of the solid matrix of the waste itself (the metallic canister enclosing the waste) and the backfill (the sealing material placed around the canisters to fill the cavities where they are placed). This backfill it is also called an engineered barrier and is often composed of compacted expansive clay. Bentonite has commonly used as the component of this barrier because of its high swelling capacity and low permeability.

The low permeability in the bentonite is due to the higher concentration of Na-montmorillonite, a clay mineral that swells in water (Steefel et al., 2010).

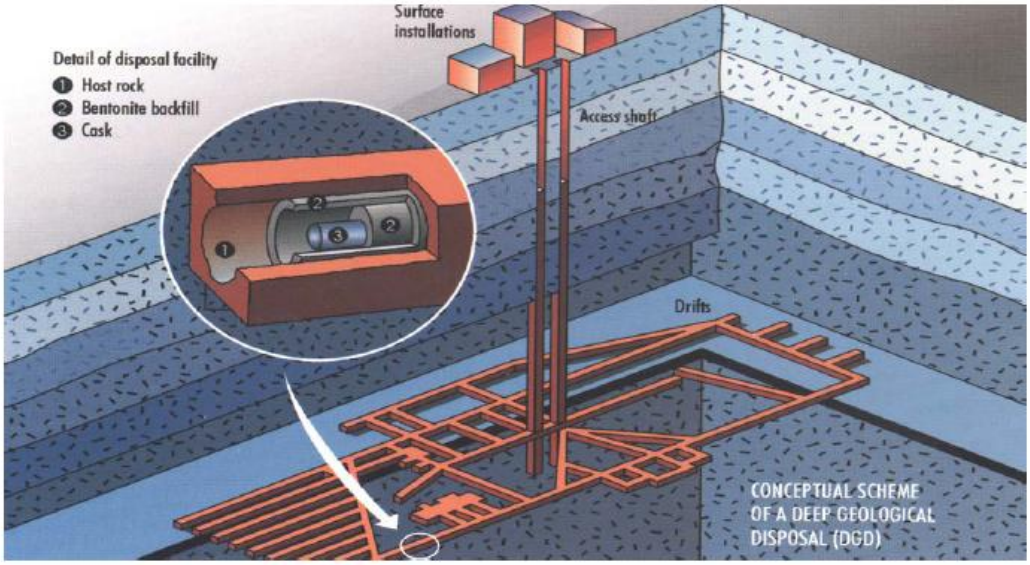

Figure 1.2 Conceptual of a deep geological disposal (Gens, 2003).

The engineered clay barrier and adjacent host rock will be subjected to the heating effect of the nuclear waste and also to various associated hydraulic and mechanical phenomena. In addition, the compacted bentonite is initially unsaturated and will be subjected to hydration from the surrounding rock developing swelling pressures; letting to a thermo-hydro-mechanical (THM) coupled phenomena. In order to achieve a good and safe design for these repositories, it is important to understand the main THM processes and their couplings. Recent studies have been discussed the effect of these processes on the behavior of the bentonite buffer. In addition, other areas of interest include: the hydration of the barrier and the time required for full saturation; the

homogenization, gaps and bentonite pellets; the piping, erosion and chemical interactions as mentioned in the report by Steefel et al., 2010.

In the last few years, several large and medium scales tests have been performed around the world to examine the interaction of the host rock with the engineered barrier. The tests are mainly focused in expansive clays to study their behavior as sealing materials for nuclear waste repositories. These hydration tests are performed under confined and non-isothermal conditions in order to have a better representation of the repository's environment. Typically, the clay is compacted at a given density and is enclosed inside a cylindrical structure where it is constrained to prevent any deformation due to swelling. The clay is hydrated at a given liquid pressure from one end and is heated at a given temperature from the other end. The evolution of temperature, relative humidity and water intake are measured by sensors placed in different locations along the barrier. In many of these tests like the ones carried out by the Atomic Energy of Canada Limited (AECL) and those sponsored by ENRESA, an unexpected reduction in the hydration rate inside the bentonite barrier was observed.

Since 1980, the AECL has operated an Underground Research Laboratory (URL) near Lac du Bonnet in Manitoba to study different aspects related to the design and construction of a deep geologic repository in the granitic rocks of the Canadian Shield. In addition, several experiments have been carried out to observe the performance of repository sealing components and systems. Two of these experiments are: the buffer-container experiment (BCE) and the isothermal buffer-rock-concrete plug interaction test (ITT) (Dixon et al., 2002). These tests were performed having in mind the following

objectives: measurement and examination of the rate of water uptake by moisture distribution inside the buffer; the swelling characteristics of the buffer; the swelling induced pressures within the buffer mass and on the host rock; the rates of change of pore-water pressures in the buffer and the surrounding rock and some chemical changes within the buffer as a result of thermal and hydraulic processes.

The BCE and ITT were performed in boreholes 5 m deep by 1.24 m of diameter excavated using a high pressure water jet drill. The buffer (barrier) material was compacted in 50 mm thick lifts inside the boreholes by a dynamic impact hammer. Several instruments were installed within the buffer. In order to provide vertical restraint due to swelling, a rigid steel cap was installed for the BCE while the ITT had a 1.25 m thick concrete block placed over the barrier. In the BCE, an internal heater was installed to simulate the heat emitted by the nuclear waste while the ITT was performed at isothermal conditions (no heater was installed). The BCE and ITT were monitored for 2.5 and 6.5 years respectively, as they hydrated from the host rock.

The hydraulic results from the ITT showed that after the test was over, the barrier had taken on approximately 70 % of the water required to reach fully saturation. In this test, the water up take was lower than the predicted measurements in a pre test inflow test. The difference between the measurements and predicted water content was due to an apparent decrease in the rate of water from the host rock to the barrier inside the borehole. Post test monitoring of groundwater reported a 35 % reduction in the rate of groundwater inflow to the borehole with an installed barrier. One of the possible mechanisms responsible for this reduction in the inflow rate is the partial plugging of the

pores in the granite by bentonite intrusion (Dixon et al., 2002). For the same experiment, Thomas et al., 2003 explained the slowdown of the hydration rate by considering changes in the clay microstructure. This is an issue that is receiving examination as it has an impact on the development of water intake models.

Another relevant project is the *FEBEX* (Full-scale Engineering Barrier Experiment) sponsored by ENRESA. This project consists of three parts: an in situ test, under natural conditions and at full scale at Grimsel, Switzerland; the *mock-up* test, at almost full scale and a series of laboratory tests carried out at the facilities of CIEMAT in Madrid, Spain. In these tests it was also observed a trend to a very low rate hydration compared to the predicted one (Sánchez and Gens, 2001). It was found out that an important part of the clay barrier is still unsaturated after eight years of hydration. Experimental evidence showed that the rate of hydration in the clay barrier depends on the properties of the bentonite, the surrounding media hydraulic properties, waste temperature, buffer thickness and geometry (Villar et al., 2012). In order to find an explanation to this apparent decay in the hydration of the barrier, different aspects were considered. First, it was explored whether minor modifications of the constitutive laws in the model were possible to explain and reproduce more accurately the evolution of the test. Other aspect considered was the performance of the hydration system. It was explored whether there was any piece in the hydration system that may blocked the flow of water and therefore the hydration rate. It was confirmed by experimental tests that there was no obstruction in the hydration system.

In order to explain the behavior of the engineered barrier, different THM models were developed. However, traditional THM models are not able to capture the trend of the experimental data from different hydration tests. This discrepancy between the measured and computed values was mainly due to the fact that the models overestimated the hydration rate of the clay sample. The THM formulation proposed by Olivella et al., 1994 and the corresponding computer code CODE_BRIGHT have been used to described and analyze the mentioned behavior of the clay barrier. However, the models based on this formulation under predict the time required to reach fully saturation of the engineered barrier according to Sánchez et al., 2005; Sánchez et al., 2012. The tendency to a very low hydration rate observed at advanced stages of the mentioned experiments, led to significant differences between model predictions and measurements. This may be caused either by inaccuracies in parameter values, or by a faulty conceptual model of the THM processes (Steefel et al., 2010). This situation has an effect on the reliability of the long term predictions, especially the one related to the time required to reach the full saturation of the clay barrier. In an effort to explain the complex behavior of the bentonite, other phenomena have been included to the conventional THM models. These phenomena include: the effect of microstructural evolution (Sánchez et al., 2005; Sánchez et al., 2012), the existence of different states of water in the bentonite, the presence of a threshold hydraulic gradient for water flow and thermo-osmosis (Zheng and Samper, 2008; Zheng et al., 2010).

1.2 Objectives And Thesis Organization

The aim of this thesis is to study the THM phenomena observed in expansive clays used as sealing materials (barriers) under unsaturated conditions in the design of nuclear waste repositories. In order to explain this coupled behavior, first it is necessary to perform a series of tests at different scales to simulate the conditions expected in a nuclear repository. Throughout this process, the main THM variables (temperature, relative humidity, water intake, stresses) can be measured and relevant experimental data can be collected. These data can be used later to assessed the performance of the THM models by the comparison of measurements with numerical predictions.

The following activities were performed to fulfill the aim of this thesis:

- Discuss the main physical and engineering properties of FEBEX bentonite obtained through a series of tests performed during the FEBEX project.
- Discuss the complete THM mathematical framework proposed by Olivella et al., 1994 based on balance equations, constitutive laws and equilibrium restrictions.
- Study other phenomena like the threshold hydraulic gradient, thermo-osmosis and double structure to the original THM formulation in an effort to explain the reduction in the hydration rate observed in the FEBEX bentonite.
- Describe two infiltration laboratory tests and the mock-up experiment carried out by CIEMAT under typical repository conditions.

- Analyze the performance of the Operational Base Case (OBC) model, based on the original THM formulation by the comparison of the numerical results with the experimental data obtained from the laboratory and mock-up infiltration tests.
- Analyze the performance of the threshold hydraulic gradient (THG), thermo-osmosis (THO) and double structure (DS) models by the comparison of the numerical results with the experimental data obtained from the laboratory and mock-up infiltration tests.
- Describe a synthetic in-situ exercise sponsored by the eFEBEX project to study the THM evolution of a full scale bentonite buffer under typical repository conditions.
- Perform a numerical analysis to study the THM evolution of an in-situ full scale bentonite buffer under repository conditions. In this exercise, numerical predictions of the main THM variables are obtained from the Operational Base Case (OBC) and thermo-osmosis (THO) models for a period of 1000 years.

This thesis is divided into seven major sections, references and appendix. The following summarizes the content in each section.

Section 2 presents a complete THM mathematical framework proposed by Olivella based on balance equations, constitutive laws and equilibrium restrictions. In addition, the threshold hydraulic gradient, thermo-osmosis and the double structure approach proposed by Sánchez et al., 2005 are also discussed.

Section 3 discusses the most relevant physical and engineering properties of the FEBEX bentonite obtained from different experiments carried out during the FEBEX project. The main thermal, hydraulic and mechanical properties are presented.

Section 4 describes the small scale infiltration tests performed by CIEMAT on 40 cm cells under thermal and isothermal conditions. The experimental measurements of temperature and relative humidity are compared with the numerical results obtained from THM models. The numerical analysis is divided into five cases where the phenomena of threshold hydraulic gradient, thermo-osmosis and double structure are considered.

Section 5 describes the mock-up test carried out by CIEMAT under repository conditions. The experimental measurements of the principal THM variables are compared with the numerical results obtained from THM models. The numerical analysis is divided into four cases where the phenomena of threshold hydraulic gradient, thermo-osmosis and double structure are considered.

Section 6 presents a synthetic case where a full scale bentonite buffer is being simulated under typical repository conditions. The numerical analysis is performed based on the Operational Base Case and thermo-osmosis models.

Section 7 presents the main conclusions of all sections and provides suggestions for future research.

2. FEBEX BENTONITE

The FEBEX bentonite is a type of clay extracted from the Cortijo de Archidona deposit at Almeria, Spain. This deposit was selected by ENRESA as the ideal material for the backfilling and sealing of HLW repositories. The main reasons for this selection include the high content of montmorillonite, large swelling pressure, low permeability, suitable thermal conductivity, good retention properties and the ease of compaction to fabricate the bentonite blocks. These characteristics make this bentonite the suitable clay material to manufacture the blocks of the Mock-up and in-situ tests for the FEBEX project.

Several years prior to FEBEX project and following the selection of the mentioned deposit, various characterization and behavior studies were performed by different organizations like CIEMAT, CSIC-Zaidín, UPC-DIT and GRS. These studies allowed ENRESA to develop a complete database on the bentonite properties. The physic-chemical properties as well as the thermo-hydro-mechanical characteristics of the FEBEX bentonite can be found in the final reports of the FEBEX project (ENRESA 2000). This section includes a summary of the results of the tests performed prior to the FEBEX project to determine the most relevant properties of the FEBEX bentonite.

2.1 Mineralogy, Chemical Composition And Fabric

The FEBEX bentonite has a very high content of montmorillonite (type dioctahedric smectite). Based on X-ray refraction, the smectitic phases are made of a smectite-illite mixed layer with 10 to 15 percent of illite layers. This study also revealed that the montmorillonite content in the bentonite varies between 89 % and 95 % as Table 2.1 shows.

Table 2.1 Content of minerals in FEBEX bentonite (ENRESA, 2000).

Mineral	**Content (%)**
Smectite	**92 ± 3**
Quartz	**2 ± 1**
Plagioclase	**2 ± 1**
Cristobalite	**2 ± 1**
K-Feldspars	**Traces**
Tridymite	**Traces**
Calate	**Traces**

In addition to the high content of smectite and the minerals included in Table 2.1, there are other minerals in the FEBEX bentonite. These minerals contribute to approximately 0.8 percent of the bentonite composition and include: mica (biotite, sericite, muscovite), chlorite, non-differentiated silicates (Al, K, Fe, Mg, Mn), augite-diopside, hypersthene, hornblende, oxides (ilmenite, rutile, magnetite, Fe-oxides),

phosphates (apatite, xenotime, monacite) and other non-differentiated minerals of titanium. The identification of these minerals has been determined by weight from dense concentrates and SEM observations.

The chemical composition of an aqueous extract of bentonite/water ratio of ¼ is presented in Table 2.2 (Fernández et al., 2003; ENRESA, 2000). A special attention is brought to the content of chlorides and sulphates present in the bentonite as trace elements due to their influence on the pore water chemistry.

Table 2.2 Trace elements in the ¼ bentonite/water aqueous extract as determined by two laboratories. Concentrations related to the dry mass of clay (mmol/100g) (ENRESA, 2000).

Laboratory	**pH**	**Cl^-**	**SO_4^{2-}**	**HCO_3^-**	**Na^+**	**K^+**	**Mg^{2+}**	**Ca^{2+}**	**Al^{3+}**	**SiO_2**
CIEMAT	**8.73**	**1.98**	**0.98**	**1.18**	**5.02**	**0.073**	**0.055**	**0.05**	**0.013**	**0.145**
UAM	**7.93**	**2.03**	**1.84**	**1.56**	**6.04**	**0.062**	**0.146**	**0.067**	**-**	**-**

Table 2.3 shows the average content values of the exchangeable cations and the cation exchange capacity (CEC) determined by CSIC-Zaidin and CIEMAT using different laboratory methods. The values reported by CSIC-Zaidin were determined by the displacement of 1M NH_4AcO at a pH of 7 after washing of soluble salts (ENRESA, 2000). On the other hand, CIEMAT used 0.5M $CsNO_3$ (Fernández et al., 2003). These values were recalculated to give the sum of cations equal to CEC. The high values of CEC obtained in these tests are due to the high content of montmorillonite in the FEBEX bentonite.

Table 2.3 Average content values of exchangeable cations and CEC in meq/100g (ENRESA, 2000).

Exchangeable cations and CEC	CSIC-Zaidin	CIEMAT
Ca^{2+}	**43 ± 5**	**42 ± 3**
Mg^{2+}	**32 ± 3**	**32 ± 2**
Na^{+}	**24 ± 4**	**25 ± 2**
K^{+}	**2.1 ± 0.2**	**2.5 ± 0.3**
CEC	**101 ± 4**	**102 ± 4**

The fabric of this material was studied by polarizing optical microscopy of thin sections of compacted FEBEX bentonite. This material is mainly composed of clay aggregates and the remaining textural elements include glassy materials, volcanic rock fragments, quartz and feldspars. The amount of the remaining elements has been performed by a measure of the areas of these elements.

In addition to the quantification of the textural elements in the FEBEX bentonite, the pore size distribution was determined. Bentonite powder of a grain size less than 1mm was studied by N_2 adsorption isotherms and blocks of bentonite with a dry density of 1.75 g/cm^3 were tested using the mercury intrusion method. Table 2.4 and 2.5 show the results obtained from these tests.

Table 2.4 Pore size distribution of bentonite powder (ENRESA, 2000).

Method	Pore diameter (μm)	Quantity (%)
N_2-adsorption	**0.150 to 0.045**	**36 ± 8**
	0.045 to 0.020	**25 ± 4**
	0.020 to 0.006	**20 ± 4**
	0.006 to 0.003	**11 ± 4**
	< 0.003	**8 ± 2**

Table 2.5 Pore distribution of bentonite compacted blocks (ENRESA, 2000).

Method	Pore diameter (μm)	Quantity (%)
Mercury intrusion	**200 to 6**	**23 ± 6**
	6 to 0.1	**26 ± 6**
	0.1 to 0.006	**50 ± 10**

2.2 Identification Properties

The results presented in Table 2.6 are called the identification properties. These properties are obtained through simple tests to give us an idea of the type of physic-chemical behavior expected in a clay material. These tests were performed by CIEMAT and UPC-DIT.

Table 2.6 Identification properties of FEBEX bentonite (ENRESA, 2000).

Property	CIEMAT	UPC-DIT
Water content (%)	**13.7 ± 1.3**	**13.3 ± 1.3**
Liquid limit (%)	**102 ± 4**	**93 ± 1**
Plastic limit (%)	**53 ± 3**	**47 ± 2**
Plasticity index	**49 ± 4**	**46 ± 2**
Specific weight	**2.70 ± 0.04**	**-**
Grain-size distribution (%)		
Fraction less than 74 μm	**92 ± 1**	**87**
Fraction less than 2 μm	**68 ± 2**	**45**
Specific surface (m^2/g)		
Total	**725 ± 47**	**-**
External, BET	**32 ± 3**	**-**

The hygroscopic water content was determined in equilibrium with the air in the laboratory at a temperature of 21 ± 3 °C, a relative humidity of 50 ± 10 % and total suction of 100 MPa. The values obtained from this property resulted to be very similar in both laboratories. However, the values determined for the liquid limit showed some discrepancy with CIEMAT reporting a higher value. Despite the difference observed with this property, the reported values are considered too low for a bentonite with a very high content of montmorillonite and a high concentration of sodium as exchangeable cation. It is important to recall that the liquid limit is an indicator of the mechanical behavior of clays. In relation to mineralogical composition, a low liquid limit implies

that the physical behavior of the clay does not correspond to its mineralogical characteristics.

Regarding the grain size distribution, the values for the fraction less than 74 μm and 2 μm were determined. It should be noted that the results for the fraction less than 2 μm (clay size) obtained by CIEMAT and UPC-DIT showed a considerable difference. It is important to mention that the previous treatment made to the bentonite to determine the grain size distribution has an effect on the proportion of the clay fraction. This discrepancy may be explained by the fact that CIEMAT used a very strong dispersion procedure while UPC-DIT worked with standard geotechnical methods.

2.3 Mechanical Properties

The FEBEX bentonite is known for the high content of montmorillonite, a clay mineral that swells in contact with water. As a result, this expansive clay develops swelling pressures that are relevant to the design of barriers in nuclear waste repositories. In an effort to determine these pressures, CIEMAT performed swelling pressure tests using conventional oedometers on samples saturated with distilled water. During this study, a regression curve for the swelling pressures was developed as a function of dry density. The exponential regression is expressed by the equation below:

$$P_s = e^{(6.77\rho_d - 9.07)} \tag{2.1}$$

where P_s is the swelling pressure in MPa and ρ_d the dry density of the FEBEX bentonite in g/cm^3. According to this equation, a sample with a dry density of 1.6 g/cm^3 can

develop a swelling pressure close to 6 MPa. The difference between the experimental values and the values calculated by the equation is about 25 %. This discrepancy can be larger for higher dry densities, mainly due to the natural variability of bentonite and technical limitations (ENRESA, 2000).

In addition, swelling under load tests were performed on samples with dry density of 1.60 g/cm^3 and loads between 0.1 and 3.0 MPa. Granitic and saline water were used to saturate the samples. The granitic water was very similar to the one used for saturation in the mock up test. On the other hand, the saline water was made of a synthetic product with the similar chemical composition to that of the bentonite interstitial water. Additional tests have been performed with specimens compacted to dry densities of 1.50 and 1.70 g/cm^3 saturated with granitic water and others with samples compacted to dry densities of 1.70 g/cm^3 saturated with saline water. As anticipated, the specimens compacted to a dry density of 1.50 g/cm^3 experienced lower amount of strain on saturation with granitic water than the specimens compacted to a dry density of 1.60 g/cm^3. The samples compacted to a dry density of 1.70 g/cm^3 experienced higher strain under the same load in tests with the same load with both granitic and saline water.

The obtained values of strain are not particularly dependent on the type of water used for saturation. However, the tests performed with saline water showed higher strain values than those performed with granitic water and the values for distilled water being the highest.

2.4 Hydraulic Properties

The hydraulic conductivity of FEBEX bentonite specimens saturated with distilled water is exponentially related to their dry density according to the following equations (ENRESA, 2000):

$$\log k_w = -6.00\rho_d - 4.09 \tag{2.2}$$

for densities between 1.30 and 1.47 g/cm^3

$$\log k_w = -2.96\rho_d - 8.57 \tag{2.3}$$

for densities between 1.47 and 1.84 g/cm^3. In these expressions, k_w is the saturated hydraulic conductivity in m/s and ρ_d the dry density in g/cm^3. The values of hydraulic conductivity were in the order of 10^{-14} m/s. For example, a bentonite compacted to a dry density of 1.60 g/cm^3 has a saturated permeability of around 5.0 x 10^{-14} m/s. The variation in the experimental values with respect to the predicted ones is small for low densities. However, for high density values, this variation can reach an average of 30 %. These empirical relationships were determined based on tests performed by CIEMAT at room temperature considering the type of water used for saturation (saline or granitic) and the direction of the measurements (parallel or perpendicular to the compaction effort). None of these aspects had a relevant influence on the measurements with the exception of the use of saline water for saturation that yields a higher hydraulic conductivity.

On the other hand, the unsaturated hydraulic conductivity depends on the degree of saturation and may be expressed as the product of the relative permeability times the

saturated hydraulic conductivity. This dependence on the degree of saturation is commonly expressed by an exponential law for the relative permeability:

$$k_r = S_r^n \tag{2.4}$$

where k_r is the relative permeability and S_r is the degree of saturation.

In order to obtain the values of unsaturated hydraulic conductivity and their dependence on the degree of saturation, CIEMAT performed infiltration tests in small teflon cells. In these tests, the water content was measured throughout the sample at different times after the initiation of the infiltration process. The intrinsic permeability and the exponent in the exponential law can be estimated by means of parameter identification methods similar to those used in groundwater engineering and geophysics. The values of permeability obtained from these tests were in the order of 10^{-21} m^2 for a porosity of 0.4.

In addition, other infiltration tests have been performed by UPC-DIT to study the possible desaturation at the interface between the granite and the bentonite. In this test, a hydraulic gradient was applied across a sample of granite in contact with another sample of bentonite. The test was carried out in a triaxial cell with a confinement pressure of 0.8 MPa. The specimens were compacted to an initial dry density of 1.76 g/cm^3 with a water content of 13 %. The measurements of water content inside the bentonite sample were used to estimate a new value of the exponent in the relative permeability law.

Additionally, the unsaturated hydraulic conductivity may be determined by thermo-hydraulic tests with prescribe heat and water flows (ENRESA, 2000) in which

the exponent of the relative permeability law can be estimated. Table 2.7 shows the estimated values of the exponent “n” based on different experiments.

Table 2.7 Values of the exponent "n" in the relative permeability law estimated from different experiments (ENRESA, 2000).

Experiment	Value of "n"
Water infiltration in small teflon cells	**4.64**
Water infiltration in bentonite in contact with granite	**3.50**
Heat and water flow experiment 1	**3.06**
Heat and water flow experiment 2	**1.10**
Heat and water flow experiment 3	**1.68**

The relationship between suction and water content (characteristic or retention curve) considering the initial dry density can be expressed by the following equation (ENRESA, 2000):

$$w = (45.1\rho_{d0} - 39.2) - (18.8\rho_{d0} - 20.34)\log s \qquad (2.5)$$

where w is the water content in percent, s the suction in MPa and ρ_{d0} the initial dry density of the FEBEX bentonite. This empirical relationship was determined by CIEMAT based on suction/water content tests in unconfined conditions performed on compacted bentonite samples for three suction values and subsequently wetting and drying paths.

The retention curve of the bentonite was also determined under confined conditions based on two kinds of tests. CIEMAT used controlled suction oedometers to

prevent the swelling of the clay by applying the appropriate loads. On the other hand, UPC used special containers made of metal to maintain a constant volume in the sample while the water vapor in the clay changes with the atmosphere. As expected, minor volume changes occurred in both tests.

The results obtained from these experiments can be fitted by the van Genuchten expression:

$$S_r = S_{r0} + \left(S_{r\max} - S_{r0}\right)\left[1+\left(\frac{s}{P_0}\right)^{\frac{1}{1-\lambda}}\right]^{-\lambda} \tag{2.6}$$

or a similar expression that is more appropriate for higher values of suction:

$$S_r = S_{r0} + \left(S_{r\max} - S_{r0}\right)\left[1+\left(\frac{s}{P_0}\right)^{\frac{1}{1-\lambda}}\right]^{-\lambda}\left[1-\frac{s}{P_s}\right]^{\lambda_s} \tag{2.7}$$

where S_r is the degree of saturation, S_{r0} residual degree of saturation, $S_{r\max}$ maximum degree of saturation, s suction in MPa and P_0 in MPa, P_s in MPa, λ, λ_s are material parameters. The parameters used to fit the experimental values are show in Table 2.8.

Table 2.8 Parameters for Van Genuchten expressions (ENRESA, 2000).

Dry density (g/cm^3)	**Equation**	**P_0 (MPa)**	**λ**	**Sr0**	**Srmax**	**Ps (MPa)**	**λ_s**
1.70-1.75	**Van Genuchten, 3.6**	**90**	**0.45**	**0.00**	**1.00**	**-**	**-**
1.70-1.75	**Van Genuchten, 3.7**	**100**	**0.45**	**0.01**	**1.00**	**1500**	**0.05**

In order to describe the thermal effects on the retention curve, samples of FEBEX bentonite were compacted to dry densities under different temperatures (Villar et al., 2004). During the experiments, the samples were confined in constant volume cells to prevent any volume change. The cells were placed in desiccators with sulphuric acid solutions of various concentrations to impose different values of suction (Villar and Gómez-Espina, 2009). The data obtained from these laboratory tests were fitted by the following empirical equation:

$$w = (a + bn)\left[1 + \left(\frac{s}{P_0 e^{-\eta(n-n_0)} e^{-\alpha(T-T_0)}}\right)^{\frac{1}{1-\lambda}}\right]^{-\lambda} \tag{2.8}$$

where w is the water content in percent, n the porosity, s the suction in MPa and T the temperature in °C. The values of the parameters a, b, P_0, η, n_0, α, T_0 and λ are shown in Table 2.9.

Table 2.9 Values of parameters in Equation 3.8 (Villar and Gómez-Espina, 2009).

Parameter	a	b	P_0 (MPa)	λ	η	n_0	α (1/°C)	T_0 (°C)
Value	**10.96**	**41.89**	**12.68**	**0.211**	**7.97**	**0.40**	**0.00647**	**20**

2.5 Thermal Properties

The thermal conductivity of the FEBEX bentonite was determined in compacted samples of various dry densities and different water contents. An empirical correlation that relates the thermal conductivity with the degree of saturation was determined based on the results obtained in the laboratory tests performed by CIEMAT (ENRESA, 2000).

$$\lambda = \frac{A_1 - A_2}{1 + e^{(S_r - x_0)/d_x}} + A_2 \tag{2.9}$$

In this equation, λ is the thermal conductivity in W/m·K, S_r is the degree of saturation, A_1 is the value of thermal conductivity when $S_r = 0$, A_2 is the thermal conductivity at saturation ($S_r = 1$), x_0 is the degree of saturation at which the thermal conductivity is the average between the extreme values and d_x is a parameter. Table 2.10 shows the value of each term in this equation.

Table 2.10 Parameters used in equation 2.9 (ENRESA, 2000).

Term	Value
A_1	**0.57 ± 0.02**
A_2	**1.28 ± 0.03**
x_0	**0.65 ± 0.01**
d_x	**0.100 ± 0.016**

3. THEORETICAL FORMULATION

A complete description of the THM formulation adopted for the analysis is presented in Olivella et al., 1994, only a brief description is included here. This formulation considers the main thermal, hydraulic and mechanical phenomena. The problem is approached using a multiphase, multi species formulation that expresses mathematically the main THM phenomena in terms of the governing equations that can be divided in three groups: balance equations, constitutive equations and equilibrium restrictions.

3.1 Balance Equations

The compositional approach has been adopted to establish the mass balance equations. This approach consists of balancing the species (mineral, water and air) rather than the phases (solid, liquid and gas) as Figure 3.1 shows. In the notation, the subscript is used to identify the phase (*s* for solid, *l* for liquid and *g* for gas) and the superscript to indicate the specie (*w* for water and *a* for air).

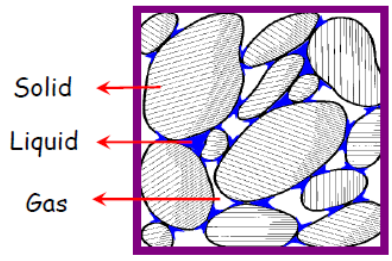

Figure 3.1 Scheme representation of the phases in the porous medium.

3.1.1 Solid Mass Balance Equation

The balance of the solid phase can be expressed as:

$$\frac{\partial}{\partial t}\left(\theta_s\left(1-n\right)\right)+\nabla\cdot\left(\mathbf{j}_s\right)=0 \tag{3.1}$$

where θ_s is the mass of solid per unit volume of solid and $\mathbf{j}_s$ is the flux of solid. From this equation, an expression for porosity variation was obtained as:

$$\frac{D_s n}{Dt}=\frac{1}{\theta_s}\left[(1-n)\frac{D_s\theta_s}{Dt}\right]+(1-n)\nabla\cdot\frac{d\mathbf{u}}{dt} \tag{3.2}$$

The equation above has been developed using the material derivative with respect to the solid that can be defined as:

$$\frac{D_s\left(\bullet\right)}{Dt}=\frac{\partial}{\partial t}+\frac{d\mathbf{u}}{dt}\cdot\nabla\left(\bullet\right) \tag{3.3}$$

Equation (3.3) expresses the variation of porosity caused by volumetric deformation and solid density variation.

3.1.2 Water Mass Balance Equation

Under unsaturated conditions, water is present in two phases: liquid and gas. The total mass balance can be written as:

$$\frac{\partial}{\partial t}\left(\theta_l^w S_l n+\theta_g^w S_g n\right)+\nabla\cdot\left(\mathbf{j}_l^w+\mathbf{j}_g^w\right)=f^w \tag{3.4}$$

where f^w is an external supply of water. An internal production term is not included because the total mass balance inside the medium is performed. The use of the material derivative leads to:

$$n\frac{D_s\left(\theta_l^w S_l+\theta_g^w S_g\right)}{Dt}+\left(\theta_l^w S_l+\theta_g^w S_g\right)\frac{D_s n}{Dt}+\left(\left(\theta_l^w S_l+\theta_g^w S_g\right)n\right)\nabla\cdot\frac{d\mathbf{u}}{dt}+\nabla\cdot\left(\mathbf{j}_l^{w}+\mathbf{j}_g^{w}\right)=f^w \quad (3.5)$$

3.1.3 Air Mass Balance Equation

Once the other mass balance equations have been written, it is straightforward to obtain the mass balance of air taking into account that air is the main component of the gas phase and that it may be also present as dissolved in air in the liquid phase.

$$n\frac{D_s\left(\theta_l^a S_l+\theta_g^a S_g\right)}{Dt}+\left(\theta_l^a S_l+\theta_g^a S_g\right)\frac{D_s n}{Dt}+\left(\left(\theta_l^a S_l+\theta_g^a S_g\right)n\right)\nabla\cdot\frac{d\mathbf{u}}{dt}+\nabla\cdot\left(\mathbf{j}_l^{a}+\mathbf{j}_g^{a}\right)=f^a \quad (3.6)$$

3.1.4 Momentum Balance Equation

If the inertial terms are neglected, the momentum balance equation reduces to the equilibrium of stresses:

$$\nabla\cdot\sigma+\mathbf{b}=\mathbf{0} \quad (3.7)$$

where $\boldsymbol{\sigma}$ is the stress tensor and $\mathbf{b}$ is the vector of body forces.

3.1.5 Internal Energy Balance Of The Medium

The equation for internal energy balance for the porous medium is established taking into account the internal energy in each phase (E_s, E_l, E_g):

$$\frac{\partial}{\partial t}\left(E_s\rho_s\left(1-n\right)+E_l\rho_l S_l n+E_g\rho_g S_g n\right)+\nabla\cdot(\mathbf{i}_c+\mathbf{j}_{Es}+\mathbf{j}_{El}+\mathbf{j}_{Eg})=f^Q \qquad (3.8)$$

where $\mathbf{i}_c$ is energy flux due to conduction through the porous medium, the other fluxes ($\mathbf{j}_{Es}$, $\mathbf{j}_{El}$, $\mathbf{j}_{Eg}$) are advective fluxes of energy caused by mass motions and f^Q is an internal/external energy supply. In this case, this term accounts for instance, energy dissipation due to medium deformation which is not explicit because it is negligible in most cases. The use of the material derivative allows obtaining an equation formally similar to the mass balance of water. The reason for the similarity is that both water and internal energy are considered present in the three phases.

Hence, only one equation is required which expresses the balance of internal energy in the porous medium as a whole. In problems involving geological materials, this equation usually reduces to the balance of enthalpy. The reason for this is that the variations of temperature produce enthalpy variations which are very large compared with the energy variations supplied from deformation work.

The fluxes in the divergence term include conduction of heat and advection of heat caused by the motion of every species in the medium. A non-advective mass flux causes an advective heat flux because a specie inside a phase moves and transports

energy. Contrary to what happens with the movement of a contaminant in a groundwater system, the diffusive term for heat transport (conduction of heat) is much larger than the term concerning hydromechanical dispersion non-advective (flux caused by the velocity of fluids). For this reason, this term is usually neglected.

3.2 Constitutive Equations

The constitutive equations establish the link between the independent variables (or unknowns) and the dependent variables. There are several categories of dependent variables depending on the complexity with which they are related to the unknowns. The governing equations are finally written in terms of the unknowns when the constitutive equations are substituted in the balance equations. The constitutive equations for the thermal, hydraulic and mechanical problem are presented next.

3.2.1 Thermal

Conductive heat flow is assumed to be governed by Fourier's law:

$$\mathbf{i}_c = -\lambda \nabla T \tag{3.9}$$

Based on experimental results of FEBEX Bentonite (ENRESA, 2000) the following law has been adopted:

$$\lambda = \lambda_{sat}^{S_l} \lambda_{dry}^{(1-S_l)} \tag{3.10}$$

where λ is the global thermal conductivity of the porous medium and S_l is the volumetric liquid fraction. λ_{sat} = 1.15 and λ_{dry} = 0.47 W/mºC have been obtained based on experimental measurements as Figure 3.2 shows.

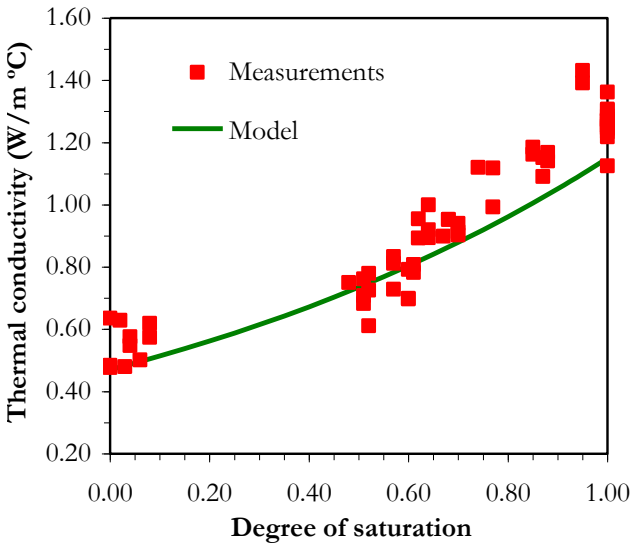

Figure 3.2 Thermal conductivity law adopted for the FEBEX bentonite.

The total internal energy for the medium is computed by the addition of the internal energy of each phase (Olivella et al., 1994).

$$E = E_s \rho_s (1-n) + E_l \rho_l S_l n + E_g \rho_g S_g n \tag{3.11}$$

where E_s, E_l and E_g are the specific internal energies corresponding to each phase, i.e., the internal energy per unit mass of phase. ρ_s, ρ_l, ρ_g, are the densities of the three phases, n is the porosity and S_g is the gas fraction with respect to the pore volume.

The gas phase energy is usually expressed as (Olivella et al., 1994):

$$E_g \rho_g = \left(E_g^w \omega_g^w + E_g^a \omega_g^a \right) \rho_g = E_g^w \theta_g^w + E_g^a \theta_g^a \tag{3.12}$$

where $E^w{}_g$ and $E^a{}_g$ are the specific internal energies of water and air species respectively, that is, the internal energy per unit of mass of species. $\omega^w{}_g$ and $\omega^a{}_g$ are the mass fraction of water and air species in gas phase, respectively. This additive decomposition is admissible for the gaseous phase in the assumption of mixture of gasses. It is not so direct that the same decomposition is also valid for the liquid phase. However, the same assumption will be made since the significance of the internal energy of dissolved air is small (Olivella et al., 1994; Gens and Olivella, 2000):

$$E_l \rho_l = \left(E_l^w \omega_l^w + E_g^a \omega_l^a \right) \rho_l = E_l^w \theta_l^w + E_g^a \theta_l^a \tag{3.13}$$

The values of the specific internal energies for the individual species are (Gens and Olivella, 2000):

$E^w{}_l$ = 4180.0 (T-T_0) J/kg; $E^w{}_g$ = 2.5e^6+1900.0 (T-T_0) J/kg; $E^a{}_g$ = 1006.0 (T-T_0) J/kg, and $E^a{}_g$ = 1006.0 (T-T_0) J/kg.

The law obtained from the experimental data of FEBEX bentotine and suggested in ENRESA (1998) has been used for the internal energy per unit mass of solid phase. This expression is given by:

$$E_s = E_s^o T + c_p T^2 \tag{3.14}$$

where the two models parameters are: $E^0{}_s$ = 732.52 and c_p =1.38 (ENRESA, 1998). For the steel, the values adopted for these parameters are $E^0{}_s$ = 480 and c_p =0 (Sears and Zemansky, 1966).

3.2.2 Hydraulic

Regarding the hydraulic problem, the general Darcy's law can relate the unsaturated flow with the fluid pressures with the following expression:

$$\mathbf{q}_\alpha = -\mathbf{K}_\alpha \left(\nabla P_\alpha - \rho_\alpha \mathbf{g}\right) \tag{3.15}$$

where the subscript α refers to the phase as $\alpha = l$ for the liquid phase and $\alpha = \mathrm{g}$ for the gas phase. P_α is the phase pressure, ρ_α is the phase density and $\mathbf{g}$ is the gravity vector. $\boldsymbol{K}_\alpha$ is the permeability tensor that depends on fluid viscosity, degree of saturation and pore structure. The permeability tensor is not constant. However, it depends on other variables:

$$\mathbf{K}_\alpha = \mathbf{k}\frac{k_{r\alpha}}{\mu_\alpha} \tag{3.16}$$

where $\mathbf{k}$ is the intrinsic permeability tensor, μ_α and $k_{r\alpha}$ are the dynamic viscosity and relative permeability of the α phase, respectively.

The intrinsic permeability depends on the pore structure. This dependence is considered in terms of porosity. Two laws are being used in the analysis. In the first law, the intrinsic permeability of the bentonite is a function of the porosity:

$$\mathbf{k} = k_0 \frac{n^3}{\left(1-n\right)^2}\frac{\left(1-n_0\right)^2}{n_0^3}\mathbf{I} \tag{3.17}$$

where k_0 is the reference permeability at the reference porosity n_0. The second approach corresponds to an exponential law, presented as follows:

$$\mathbf{k} = k_0 \exp[b\left(n-n_0\right)]\mathbf{I} \tag{3.18}$$

where k_0 is the intrinsic permeability for a reference porosity n_0, b is a model parameter and **I** is the identity tensor. The model parameters (k_0 = 5.0 x 10^{-20} m^2; n_0 = 0.14 and b = 50) have been determined from back calculations of the results of permeability tests under isochoric conditions (Figure 3.3).

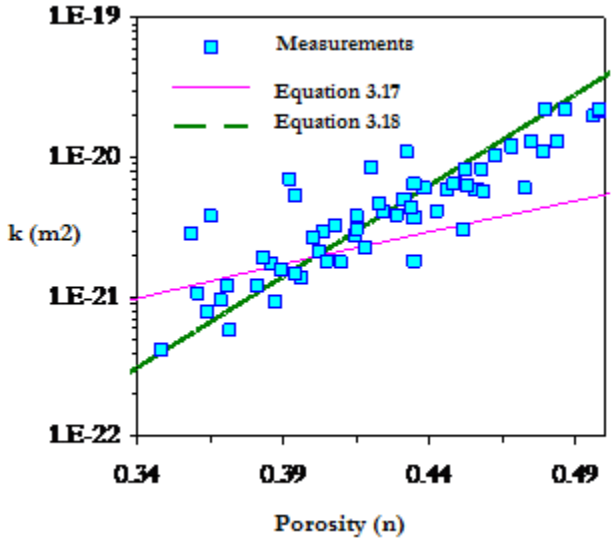

Figure 3.3 Variation of saturated permeability with porosity. Experimental data and adopted models for the intrinsic permeability law.

The relative permeabilities for the liquid and gas phase depend on the degree of saturation and can be expressed as:

$$a)\ k_{rl} = S_{el}^{\ n} \qquad b)\ k_{rg} = \left(1 - k_{rl}\right) \tag{3.19}$$

where:

$$S_{el} = \frac{S_l - S_{lr}}{S_{ls} - S_{lr}} \tag{3.20}$$

S_{lr} , S_{ls} and n are model parameters. Equation (3.19) considers the decrease in hydraulic permeability as the degree of saturation decreases. This variation is very difficult to determine directly and it is necessary to resort to indirect ways of estimation.

To establish the link between the degree of saturation and suction, the retention curve (Figure 3.4) was used with the following expression:

$$S_{el} = \left[1+\left(\frac{s}{P_o}\right)^{\frac{1}{1-\lambda_o}}\right]^{-\lambda_o} f_d \tag{3.21}$$

$$f_d = \left(1-\frac{s}{P_d}\right)^{\lambda_d} \tag{3.22}$$

where s is the suction, P_o is the air entry value and λ_o is a model parameter. The function f_d is used to obtain more reasonable values at high suctions.

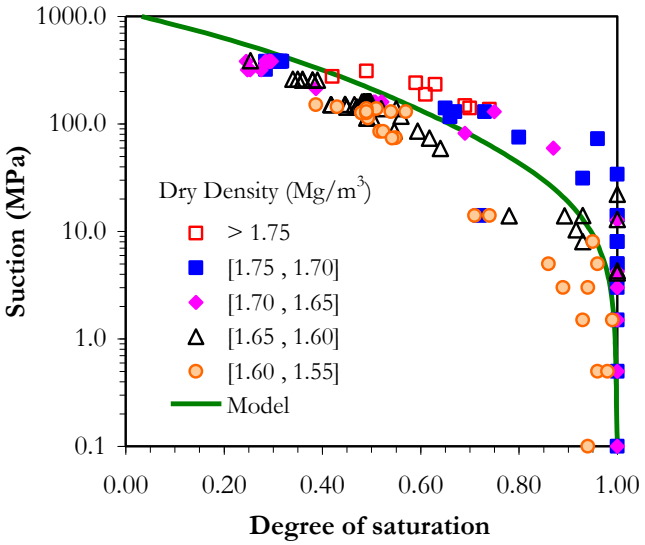

Figure 3.4 Retention curve adopted in the analyses, together with the experimental data of FEBEX bentonite (symbols).

The Fick's law has been used to explain the diffusion process occurring in the system. This law describes the water vapor diffusion in the gas phase and air diffusion in water. In addition, with this expression the non-advective fluxes of species inside the fluid phases can be computed. It also expresses them in terms of gradients of mass fraction of species through a hydrodynamic dispersion tensor that includes both molecular diffusion and mechanical dispersion (Olivella et al., 1994; Gens and Olivella, 2000):

$$\mathbf{i}_\alpha^i = -\mathbf{D}_\alpha^i \nabla \omega_\alpha^i \qquad i = w, a; \qquad \alpha = l, g \tag{3.23}$$

where $\mathbf{D}^i{}_\alpha$ is the dispersion tensor of the medium.

For vapor diffusion, the following expression for the hydrodynamic dispersion tensor is adopted (Olivella et al., 1994):

$$\mathbf{i}_g^w = -\mathbf{D}_g^w \nabla \omega_g^w = -\left(n \rho_g S_g \tau D_m^w \mathbf{I} + \rho_g \mathbf{D}'_g \right) \nabla \omega_g^w \tag{3.24}$$

where $\mathbf{D}_g{}^w$ is the dispersion tensor, τ is the tortuosity, $D_m{}^w$ is the dispersion coefficient corresponding to molecular diffusion of vapor in air and D'_g is the mechanical dispersion tensor. The molecular diffusion coefficient is given by (Olivella et al., 1994; Gens and Olivella 2000):

$$D_m^w = 5.9x10^{-12} \frac{\left(273.15 + T\right)^{23}}{P_g} \tag{3.25}$$

where $D_m{}^w$ is in m^2/s, P_g is in MPa and T in ºC.

The mechanical dispersion can be defined with the following expression (Olivella et al., 1994; Gens and Olivella, 2000):

$$\mathbf{D}_g^{'} = -\mathbf{q}_g \mathbf{I} + \left(d_l - d_t\right)\frac{\mathbf{q}_g \mathbf{q}_g^t}{\left|\mathbf{q}_g\right|} \tag{3.26}$$

where d_t and d_l are the transversal and longitudinal dispersivities, respectively.

Finally, the diffusion of air in the liquid phase can be written as:

$$\mathbf{i}_l^a = -\mathbf{D}_l^a \nabla \omega_l^a = -\left(n\rho_l S_l \tau D_m^a \mathbf{I} + \rho_l \mathbf{D}_l^{'}\right)\nabla \omega_l^a \tag{3.27}$$

3.2.3 Mechanical

The mechanical constitutive law adopted is the Barcelona Basic Model (BBM). The BBM is an elasto-plastic strain hardening model which extends the concept of critical state for saturated soils to unsaturated conditions and it is capable to reproduce the behavior observed under these conditions. This model takes into account two independent stress variables: the net stress (σ), defined as the excess of the total stresses over the gas pressure ($\sigma_t - \boldsymbol{I} p_g$) and the matric suction (s), defined as the difference between gas pressure and liquid pressure. The BBM was created in terms of the three stress invariants (p, J, θ), suction and temperature. The stress invariants are defined as follows:

$$p = \left(\frac{1}{3}\right)\left(\sigma_x + \sigma_y + \sigma_z\right) \tag{3.28}$$

$$J^2 = \frac{1}{2trace\left(s^2\right)} \tag{3.29}$$

$$\theta = -\frac{1}{3}\sin^{-1}\left(1.5\sqrt{3}\det s / J^3\right) \tag{3.30}$$

$$s = \sigma - pI \tag{3.31}$$

where ***I*** is the identity tensor. In this model the yield surface depends also on the matric suction. The trace of the yielding function on the p-s plane is called the LC (Loading-Collapse) curve. This curve represents the position where the activation of permanent deformations due to loading increments or wetting takes place. The position of the LC curve is given by p_0^*, the pre consolidation yield stress for saturated conditions. Pre consolidation pressure is affected by the temperature assuming that temperature increases reduce the size of the yielding surface and the strength of the material. This is a common behavior for saturated soils as established in Hueckel and Borsetto, (1990) and can also be extended to unsaturated conditions as recent experimental studies show. The BBM yield surface can be expressed as:

$$F_{LC} = 3J^2 - \left[\frac{g(\theta)}{g(-30^\circ)}\right]^2 M^2 (p + p_s)(p_0 - p) = 0 \tag{3.32}$$

where M is the slope of the critical state, p_0 is the unsaturated isotropic pre consolidation stress at a specific value of suction and p_s takes into account the dependence of shear strength on suction and temperature. In addition, $g(\theta)$ represents the Lode's angle function. When yielding takes place, the increment of plastic deformation is defined as:

$$\varepsilon_{LC}^{\dot{p}} = \lambda_{LC} \frac{\partial G}{\partial \sigma} \tag{3.33}$$

where λ_{LC} is the plastic multiplier and G is the plastic potential determined as follows:

$$G = \alpha_G 3J^2 - \left[\frac{g(\theta)}{g(-30^\circ)}\right]^2 M^2 (p + p_s)(p_0 - p) = 0 \tag{3.34}$$

α_G is determined according to Alonso et al., 1990.

The hardening law is expressed as a rate relation between the volumetric plastic strain and the saturated isotropic pre consolidation stress p_0^* according to:

$$\frac{\dot{p}_0^*}{p_0^*} = \frac{(1+e)}{(\lambda_{(0)} - \kappa)} \varepsilon_v^{\dot{p}} \tag{3.35}$$

where e is the void ratio, ε_v^p is the volumetric plastic strain, κ is the elastic compression index for changes in p and $\lambda_{(0)}$ is the stiffness parameter for changes in p for virgin states of the soil in saturated condition.

Due to the high compaction to which the bentonite has been subjected, the description of the behavior of the material inside the yield surface is relevant. According to the model parameters, it is expected that the stress path will lie inside the BBM yield surface. The variation of stress-stiffness with suction and the variation of swelling with stress and suction have been taken into account. The elastic model can be expressed as follows:

$$\dot{\varepsilon}_v^e = \frac{\kappa}{(1+e)} \frac{\dot{p}}{p} + \frac{\kappa_s}{(1+e)} \frac{\dot{s}}{(s+0.1)} + (\alpha_0 + \alpha_2 \Delta T)\dot{T} \tag{3.36}$$

$$\dot{\varepsilon}_s^e = \frac{J}{G_t} \tag{3.37}$$

where κ_s is the macrostructural elastic stiffness parameter for changes in suction, G_t is the shear modulus; α_0 and α_2 are model parameters related to temperature. κ, κ_s and G_t can be determined according to:

$$\kappa = \kappa_i (1 + \alpha_s s) \tag{3.38}$$

$$\kappa_s = \kappa_{s0}\left(1+\alpha_{sp}\ln p/p_{ref}\right) \tag{3.39}$$

$$G_t = \frac{3(1-2\mu)K}{2(1+\mu)} \tag{3.40}$$

where μ is the Poisson's coefficient, α_s and α_{sp} are model parameters and K is the bulk modulus.

3.3 Equilibrium Restrictions

Another type of relationships that relate dependent variables with unknowns are the equilibrium restrictions. They are obtained assuming chemical equilibrium for dissolution of the different species (air and vapor) in phases (liquid, gas).

The vapor concentration in the gaseous phase is governed by the psychometric law, which can be defined as (Gens and Olivella, 2000):

$$\theta_g^w = \left(\theta_g^w\right)^0 \exp\left(\frac{\Psi M_w}{R(273.15+T)\rho_l}\right) \tag{3.41}$$

where $\theta_g{}^w$ is the vapor concentration in the gas phase; $(\theta_g{}^w)^0$ is the vapor concentration in the gas phase in equilibrium with a liquid at the sample temperature; Ψ is the total water potential of the water, in this case it is related to suction (Ψ = P_l - P_g); M_w is the molecular mass of the water (0.018 kg/mol) and R the gas constant (8.314 J/mol/ºK). The gases law relates vapor density and vapor pressure (Olivella et al., 1994):

$$\left(\theta_g^w\right)^0 = \frac{M_w P_{v(T)}}{R(273.15+T)} \tag{3.42}$$

For pure water, the vapor pressure has been approximate as (Olivella et al., 1994):

$$P_{v(T)} = 136075 \exp\left(\frac{-5239.7}{273.15 + T}\right) \tag{3.43}$$

To define the amount of air dissolved in water, Henry's law is adopted. This law expresses a linear relationship between the concentration of air in dissolution and the partial pressure of air (P_a) in the gaseous phase:

$$\theta_l^a = \omega_a^l \rho_l = \frac{P_a}{H} \frac{M_a}{M_w} \rho_l \tag{3.44}$$

where M_a is the molecular mass of the air (0.02895 kg/mol), and H is Henry's constant (1000 MPa).

3.4 Non-Traditional Models

In order to understand the hydration in the bentonite is necessary to explain the water flux in a porous medium. A characteristic feature of all tight media is the smallness of the pores through which flow occurs. With a large fraction of the pore fluid near to the solid surfaces, the physicochemical phenomena may have an effect in the fluid flow. This can be translated to non-hydraulic flow effects which include those that do not follow Darcy's law. This kind of flow also is moved by driving forces (osmotic or coupled flow) other than the hydraulic gradient (Neuzil, 1986). This behavior has been observed particularly on unsaturated clays under relatively low hydraulic gradients. It is expected that non-Darcian flow behavior becomes more significant under the mentioned conditions due to the fact that pore water exists as water films. As a result, it should be

subjected to strong interactions within the clay surface. In Dixon et al., 1992, it is reported that Darcy's simple relationship for flow did not appear to apply to some fine grained soils containing highly active clay minerals.

After Dixon et al., 1992, other flow-hydraulic gradient relations have been proposed by several authors. Hansbo (2001) reported that water flux is proportional to a power function of the hydraulic gradient when the gradient is less than a critical value and the relationship between water flux and hydraulic gradient becomes linear for large gradient values. He explained this behavior by establishing that a certain hydraulic gradient is required to overcome the maximum biding energy of mobile pore water.

In Zou (1996), a non linear flux-gradient relation depending on the activation energy of pore liquid was proposed. It was assumed that the activation energy of pore water in clay or other fine-grained materials is not only variable with the distance from the solid particle surface, but also with the flow velocity of pore water. The proposed relation, with some empirical parameters, was able to fit a number of data sets that show non-linear flux-gradient relationships at low hydraulic gradients and linear relationships at high gradients.

Recently, numerical models are being developed based on the theory that the water in the pores behaves as a non-Newtonian fluid (Wu and Pruess, 1998; Liu et al., 2012; Liu and Birkholzer, 2012). The model proposed by Liu et al., 2012 for flow under unsaturated conditions in clay, considers the pore water as a non-Newtonian fluid. The theoretical development of this model is based on the hypothesis that pore water in clay materials is non Newtonian and that the flow is driven by the hydraulic gradient. The

derivation of the model begins expressing the shear stress of fluid as a function of the apparent viscosity and the shear rate. Then a relationship between the flux and the hydraulic gradient for a capillary tube is derived in order to establish the corresponding correlations for clay materials. The following expression was obtained at the end of the derivation:

$$q = -K\left(\left|\frac{dH}{dx}\right|\right)^{1/n} i \tag{3.45}$$

where H is the hydraulic head, K is the hydraulic conductivity and i is the unit vector for the hydraulic gradient. In general, n can be considered a measure of non Newtonian behavior that may be saturation or capillary pressure dependent. The relationship between hydraulic conductivity for a capillary tube and its radius R is the foundation for studying relative permeability under unsaturated conditions (Liu et al., 2012). The complete derivation of this relation can be found in Liu et al., 2012.

The work presented by Cui et al., 2008 on measurements of unsaturated hydraulic conductivity for a compacted sand-Bentonite mixture was used to study the capability of the model proposed by Liu et al., 2012. Cui et al., 2008 used the instantaneous profile method to determine the unsaturated hydraulic conductivity for infiltration tests of a vertical sand-Bentonite column. The sand-Bentonite mixture was directly compacted in a metallic cylinder (50 mm in diameter and 250 mm high). The bottom of the test column was connected to a water source and the upper end to an air source at atmospheric pressure. Vertical distributions of capillary pressure were measured as a function of time at different locations along the column. The relation

between water content and capillary pressure was independently measured. This relation enables to estimate the vertical distributions of water content from the capillary pressure measurements. Water flux as a function of capillary pressure and hydraulic gradient was estimated at a specific location in the column based on the estimated vertical distributions at different times and on the mass balance at each location within the soil column. Figure 3.5 shows estimated water flux as a function of hydraulic gradient under several capillary pressures. It can be noted that evident non linear behavior rises at all the different capillary pressures, indicating that Darcy's law does not applied for the range of hydraulic gradient values under consideration. It is observed that equation 3.45 (solid lines) matches very well with the data (scatter points) for the six values of capillary pressures.

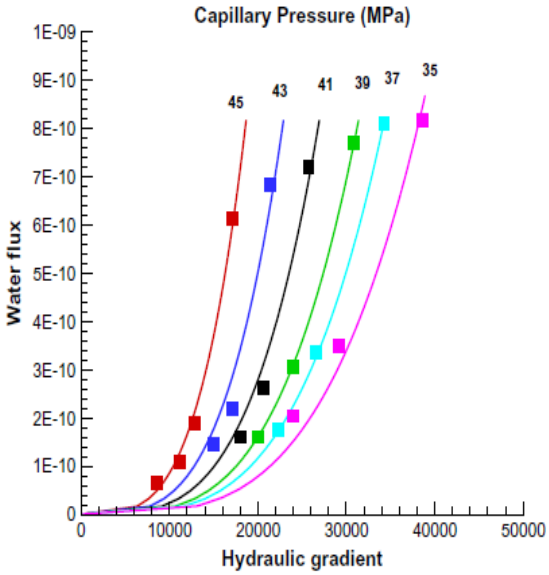

Figure 3.5 Comparison between calculated (solid lines) and estimated (scatter points) of water flux as a function of hydraulic gradient for different capillary pressures (Liu et al., 2012).

The models presented in this section are based on phenomena associated with the reduction of the hydration rate inside the clay bentonite. The models presented in this section are the threshold hydraulic gradient (THG), thermo-osmosis (THO) and double structure (DS).

3.4.1 Threshold Hydraulic Gradient

It has been documented in the literature that water flow in clays cannot be well described by Darcy's law ($Q = -KAi$), which establishes that water flux is proportional to the hydraulic gradient. Hansbo (2001) reported that water flux is proportional to a power function of the hydraulic gradient when the gradient is less than a critical value and the relationship between water flux and hydraulic gradient becomes linear for large gradient values. He explained this behavior by establishing that a certain hydraulic gradient is required to overcome the maximum biding energy of mobile pore water.

In Dixon et al., 1992; Dixon et al., 1999 it is also reported that Darcy's simple relationship for flow did not appear to apply to some fine grained soils containing highly active clay minerals. From several laboratory tests, it seems that the following expression described the flow correctly:

$$Q = -KA\left(i - i_0\right) \tag{3.46}$$

In this expression, Q, K, A and i have the same meaning as in the original equation of Darcy's law. The term i_o is an apparent threshold gradient below which no flow occurs. Associated with the threshold hydraulic gradient is the critical hydraulic

gradient i_c which is the hydraulic gradient below which the flow is non Darcian. Figure 3.6 defines this concept graphically.

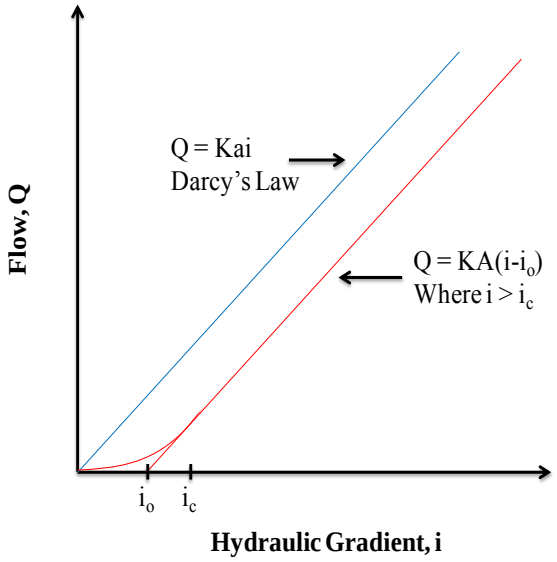

Figure 3.6 Graphical definition of Darcian and non Darcian flow. The terms i_c and i_o are the critical and threshold hydraulic gradients respectively (Dixon et al., 1992).

3.4.2 Thermo-Osmosis

In general terms, the hydraulic gradient is the main mechanism of the movement of water in soils ruled by the Darcy's law. However, at advanced stages of experimental infiltration tests under non-isothermal conditions, the hydraulic gradient becomes smaller and it is possible that coupled phenomena or a thermo-osmotic flow could have an effect on the behavior of the system, slowing down the hydration in the zones close to the heat source. The magnitude of this phenomenon will depend on the relation between the two gradients associated to each mechanism and on the relationship between the

phenomenological coefficients of each flow. Figure 3.7 shows a schematic representation of this phenomenon. The K_{HT} term corresponds to the phenomenological coefficient for the thermo-osmotic flow.

$$q_l = -K_{HH}\left(\nabla P_l - \rho_l g\right) - K_{HT}\nabla T$$

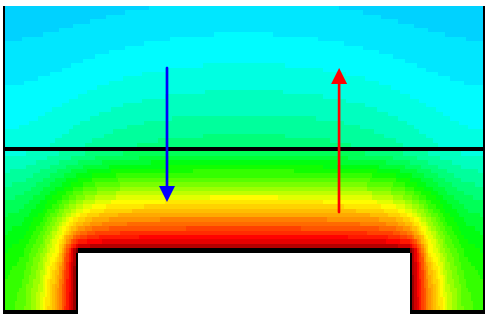

Figure 3.7 Schematic representation of the advective and thermo-osmotic flow in a typical infiltration test under non isothermal conditions.

3.4.3 Double Structure Approach

3.4.3.1 Background

Previous studies have been revealed that there is an apparent decay in the rate of the clay barrier hydration. In order to obtain reasonable long term predictions, it is important to understand this behavior. Several studies were carried out to explain the

phenomena that could cause the unexpected behavior of the barrier. Initially, some minor modifications to the constitutive laws and parameters were made to see if these changes would reproduce more closely the evolution of the test. However, it was proved that a set of constitutive equations and parameters that led to predictions consistent with the observations was not possible. Another issue considered was the possibility that the experiment was airtight or not. For the analysis, the two extreme conditions were considered: free flow of air in and out of the experiment or a completely airtight experiment. No influence on the results was observed for this condition. The hydration system of the experiment was also examined and no obstruction was found that could potentially alter the hydration of the barrier.

An aspect that had not been considered in the formulation and that may have an effect on the predictions is the nature of the fabric and microstructure of the compacted bentonite during the hydration process.

Mercury Intrusion Porosimetry (MIP) tests were performed by CIEMAT to examine the pore size distribution of compacted samples of FEBEX bentonite with different dry densities (ρ_d = 1.5 mg/m^3 and ρ_d = 1.8 mg/m^3). The predominant values are 10 nm that correspond to pores inside the clay aggregates and 10 μm (for ρ_d = 1.8 mg/m^3) to 40 μm (for ρ_d = 1.5 mg/m^3) that depends on the compaction dry density. These larger voids would correspond to inter-aggregate pores that may or may not be saturated and provide the pathways for the movement of free water. The two dominant pore sizes could be associated with two structural levels: the macrostructure (related to

the arrangements of clay aggregates and the macropores between them) and the microstructure (associated with the active clay minerals) as Figure 3.8 shows.

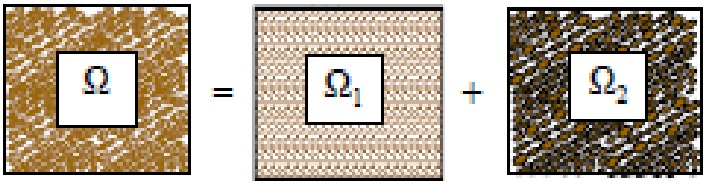

Figure 3.8 Schematic representation of the double structure in clay bentonite. Clay (Ω), microstructure (Ω_1) and macrostructure (Ω_2).

The fabric of expansive clays is changing during the hydration process. Some techniques like the ESEM (Environmental Scanning Electron Microscope) and SEM (Scanning Electron Microscope) are being used to analyze the fabric changes of FEBEX bentonite during a progressive wetting. Suction changes were applied under constant volume conditions and for a specific value of dry density (around 1.40 Mg/m^3). At the end, there was a difference between the final values of dry densities that is due to the rebound experience by the bentonite after unloading. These tests are mainly qualitative; however, they show the progressive occlusion of the macropores due to swelling of microstructure.

3.4.3.2 Numerical Model

The distinction between the macro and microstructure provides the opportunity to consider the main phenomena that affect the behavior of each structural level and the interactions between them. The complete definition of the double structure model

requires the proposal of laws to describe the macrostructural level, the microstructural level and the interaction between both structural levels. This model has been explained in detail in Sánchez et al., 2005. In addition, the ability to reproduce and predict the mechanical behavior of FEBEX bentonite under different stress paths involving loading, suction and temperature changes have been also demonstrated.

3.4.3.2.1 Microstructural Level

The microstructure is the base of the basic physic-chemical phenomena occurring at clay particle level. The microstructural strains are considered to be volumetric non linear elastic. These strains are proportional to the microstructural effective stress ($\hat{p}$) through a microstructural bulk modulus (K_m) according to Sánchez et al., 2012:

$$\hat{p} = p + \chi\left(s + s_0\right) \tag{3.47}$$

$$\dot{\varepsilon}_{vm} = \frac{\dot{\hat{p}}}{K_m} = \frac{\dot{p}}{K_m} + \chi\frac{\dot{s}}{K_m} \tag{3.48}$$

where the subscripts m and v refer to the microstructural level and volumetric strain respectively; p is the net mean stress, s_o the osmotic suction and $(s + s_o)$ is the total suction. The χ parameter was included to consider the possibility that the micropores may become unsaturated. For the analysis it has been assumed that the microstructure is saturated (χ = 1). Under saturated conditions, the mean effective stress controls the mechanical behavior at the microstructural level according to Gens and Alonso (1992).

The exponential type model suggested by Alonso (1998) has been adopted according to the following expression of the microstructural modulus (K_m):

$$K_m = \frac{e^{-\alpha_m \hat{p}}}{\beta_m} \tag{3.49}$$

where α_m and β_m are model parameters. This model has its origins in the exponential model describing the clay interlayer distance as a function of effective stress in double layers theories according to Alonso (1998).

The Neutral Line (NL) concept is introduced corresponding to a constant microstructural effective stress ($\hat{p}$) and no microstructural deformation (Sánchez et al., 2012). This line divides the p- s space in two parts, defining two general stress paths. These two stress paths are identified as MC for microstructural contraction when $\hat{p}$ is increased and MS or microstructural swelling when $\hat{p}$ is decreased.

3.4.3.2.2 Interaction Between Structural Levels

In this approach, it is assumed that the macrostructure is affected by the deformations occurring at the microstructural level (Alonso, 1990). The model assumes that the permanent deformations of the macrostructure caused by microstructural effects ($\dot{\varepsilon}^{p}_{vM\rightarrow m}$), are proportional to the microstructural strains in relation to interaction functions (f) (Sánchez et al., 2005; Alonso, 1990). This can be written mathematically as:

$$\dot{\varepsilon}^{p}_{vM\rightarrow m} = f\,\dot{\varepsilon}_{vm} \tag{3.50}$$

The interaction functions can be defined as f_c for microstructural contractions paths and f_s for microstructural swelling paths. These two functions depend on the ratio of p/p_0, which is a measure of the degree of openness of the macrostructure relative to the stress state applied. The interaction functions can be expressed as follows (Sánchez et al., 2012):

$$f_c = 1 + 0.9 \tanh\left(20\left(p/p_0\right) - 0.25\right) \tag{3.51}$$

$$f_s = 0.8 - 1.1 \tanh\left(20\left(p/p_0\right) - 0.25\right) \tag{3.52}$$

The total plastic macrostructural strains ($\dot{\varepsilon}_v^p$) are determined as the sum of the plastic deformations generated when yielding of the macrostructure takes place and the inelastic strains induced by the microstructure through the interaction process (Sánchez et al., 2005). This can be expressed as follows:

$$\dot{\varepsilon}_v^p = \dot{\varepsilon}_{vLC}^p + \dot{\varepsilon}_{vM\to m}^p \tag{3.53}$$

The coupling between macro and microstructural levels is given by p_0^* which depends on the total plastic volumetric strain. In this manner, it is considered that the changes occurring at the microstructural level can affect the global arrangements (skeleton) of clay aggregates.

3.4.3.2.3 Hydraulic Behavior

Apart from the free water, the rest of the water in clay is affected by physic-chemical phenomena occurring at clay particle (microstructural) level. This water in the

vicinity of the particles is strongly attached to the clay surface and it is practically immobile according to Hueckel and Borsetto (1990). Based on the previous ideas, it is assumed that the macropores are the main paths for the movement of water.

In the majority of the flow models, the dependence of permeability on the pore structure is introduced through a relationship between permeability and total porosity. Knowing that the macroporosity is the void fraction that has the main influence on the water flow due to hydraulic, it is proper to relate the intrinsic permeability in terms of macropore changes. This double structure model has the advantage that the two pore levels are explicitly considered, the changes in the macro and microstructure can be tracked and finally can be used to update the permeability field (Sánchez et al., 2005). The following expression suggests that the intrinsic permeability is a function of the macroporosity:

$$k = k_0 e^{b\left(\phi_M - \phi_{M_0}\right)} I \tag{3.54}$$

where ϕ_M is the macroporosity, k_0 is the intrinsic permeability for a reference porosity (ϕ_{M0}), b is a model parameter and $\boldsymbol{I}$ is the identity tensor. The model parameters (k_0= 5.0 x 10^{-20} m^2; ϕ_{M0}= 0.14 and b = 50) have been determined from back calculations of the results of permeability tests under isochoric conditions (Sánchez et al., 2005).

4. INFILTRATION TESTS

Conducting large scale tests is complicated and requires a large economic inversion. Therefore, small scale laboratory tests are being used to study the complex behavior of the clay barrier in a more rapid and economic way. These tests were carried out at CIEMAT laboratories on small cells of different lengths (8 cm, 40 cm and 60 cm) in which the compacted bentonite is subjected simultaneously to heating and hydration in opposite directions through an isothermal and thermal gradient process (Villar et al., 2012). During the test, water intake, relative humidity and temperature have been measured as a function of time with a series of sensors placed on specific locations along the cells.

This section will be focused on the description and experimental results of the 40 cm infiltration tests under isothermal and non-isothermal conditions. In addition, the THM formulation will be validated by the comparison of the numerical results with the experimental measurements.

4.1 Description Of The Tests

In order to obtain some experimental data to study the performance of the proposed models, two laboratory tests were performed. The infiltration tests are being performed by CIEMAT (Villar and Gómez-Espina, 2009; Sánchez et al., 2007) in cylindrical cells with an internal diameter of 7 cm and inner length of 40 cm as shown in

Figure 4.1. These cells were made of Teflon to prevent the lateral heat conduction and also covered with steel semi cylindrical pieces to avoid the deformation of the cell caused by bentonite swelling as Figure 4.2 shows. Five blocks of FEBEX clay were compacted with a compaction pressure of 30 MPa and piled up inside each cell with their hygroscopic water content of 14 % at an initial dry density of 1.65 g/cm^3. The two blocks placed at the ends of each cell have a length of 5 cm and the other three in the middle have a length of 10 cm.

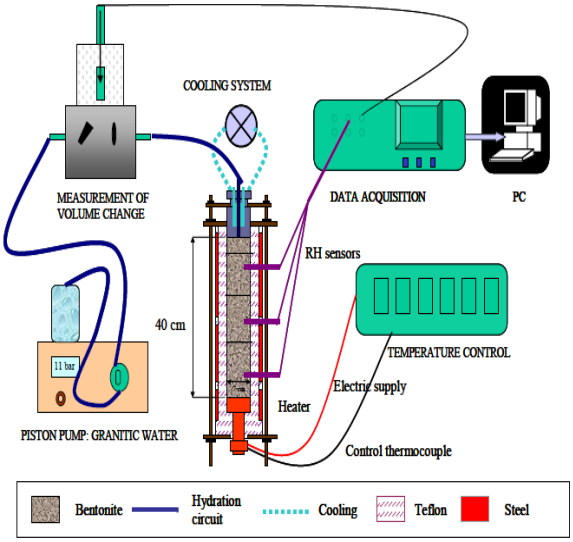

Figure 4.1 Experimental setup for infiltration tests (M.V. Villar and R. Gómez-Espina, 2009).

The hydration process was initiated by the injection of granitic water through the upper part of the cell at a pressure of 1.2 MPa. This simulates the saturation of the clay barrier due to the water flowing from the host rock. In one of the tests, the geothermal test (GT40), the clay was heated through the bottom of the cell at a temperature of 100°C

to simulate the emitting heat from the nuclear waste. On the other hand, for the isothermal test (I40) the bottom of the cell was not heated, so it was performed at room temperature between 20°C and 30°C. The cells were instrumented with sensors placed inside the clay at a spacing of 10 cm (10 cm, 20 cm and 30 cm from the bottom of the cell) to measure the temperature and relative humidity. The sensors used are the VAISALA HMP237 with the humidity sensor HUMICAP that changes its dielectrical characteristics with small variations in humidity. The temperature was measured with the Pt100 temperature sensing system. In addition to temperature and relative humidity, water intake was measured by electronic volume change measurement systems with a resolution of 0.001 cm^3.

Figure 4.2 Infiltration cells in operation: isothermal, I40 (left) and thermal gradient, GT40 (right) (M.V. Villar and R. Gómez-Espina, 2009).

4.2 Numerical Results

The experimental results from the laboratory tests were used to obtain the parameters of the constitutive models for the thermal, hydraulic and mechanical problems, as explained in section 3. With those constitutive laws the infiltration tests were modeled to explain the behavior of the bentonite cell under isothermal and non-isothermal conditions. The results correspond to temperature and relative humidity measurements made by the sensors located along the cells for a period of 10 years (3600 days). The following plots show the comparison of the measurements with the model predictions of the evolution of temperature and relative humidity in different locations of the cell: 30 cm (0.30 m), 20 cm (0.20 m) and 10 cm (0.10 m) from the heat source.

The problem was approached with a 1D mesh composed of 50 linear elements and 51 nodes. The numerical simulations were performed using the finite element program CODE_BRIGHT and divided into five cases: Operational Base Case (OBC), Threshold Hydraulic Gradient (THG), Thermo-osmosis (THO), Double Structure (DS) and Double Structure + Thermo-osmosis (DS + THO). The numerical predictions of temperature, liquid pressure and displacements were determined directly from the program. However, the values of relative humidity were computed by the psychometric law.

4.2.1 Operational Base Case

The OBC was developed based on the Barcelona Basic Model (BBM), briefly explained in section 2.2.3. A detail representation of this model can be found in Alonso (1990). Tables 4.1, 4.2, 4.3 and 4.4 show the general, mechanical, hydraulic and thermal parameters, respectively, used during the numerical simulations for the OBC case.

Table 4.1 General parameters used in the OBC case to perform the numerical analysis for the 1D infiltration tests.

Parameter	Value
ρ_{db}	**1.65**
ω	**14.00**
G_S	**2.72**
e_{total}	**0.648**
ϕ_{total}	**0.393**

Table 4.2 Mechanical parameters used in the OBC case to perform the numerical analysis for the 1D infiltration tests.

Parameter	Value	Parameter	Value
ki0	**0.05**	xlam0	**1.5**
ks0	**0.3**	r	**0.75**
K_min	**0.1**	beta	**0.05**
phimin	**0**	roh	**0.2**
xnu	**0.4**	k	**0.1**

Table 4.2 Continued

Parameter	Value	Parameter	Value
alphass	**0**	pc	**0.1**
alphais	**-0.002**	M	**1.5**
alphasp	**-0.147**	alpha	**0.395**
pref	**0.01**	e0	**0.648**
alph0	**1.50E-04**	p0ast	**14**
Tref	**20**		

Table 4.3 Hydraulic parameters used in the OBC case to perform the numerical analysis for the 1D infiltration tests.

Parameter	Value
p0d (MPa)	**7**
sigma0	**0.072**
lamdad	**0.1**
srl	**0**
sls	**1**
p	**0**
d	**0**
sd	**0**
psec	**1100**
lambda2	**2.1**
Kxx int. perm.	**1.90E-21**
Kyy int. perm.	**1.90E-21**

Table 4.3 Continued

Parameter	Value
Kzz int. perm.	**1.90E-21**
Initial porosity	**0.4**
Minimum	**0.001**

Table 4.4 Thermal parameters used in the OBC case to perform the numerical analysis for the 1D infiltration tests.

Parameter	**Value**
λ_{dry}	**0.47**
λ_{wet}	**1.15**

The numerical results for the I40 test are presented in the following figures. Figure 4.3 shows the measurements of temperature along the cell during the test for a period of 3600 days (10 years). According to this plot, values between 18°C and 32°C were recorded. However, since this is a test with isothermal conditions (no heat is applied), it is not expected to have variation in temperature. The small variation observed could be occurred because of the seasonal temperature changes during the year. The model is set to a constant temperature of 23°C (solid line) along the entire cell and the hydration process starts with a liquid pressure of 1.2 MPa applied at the top of the sample.

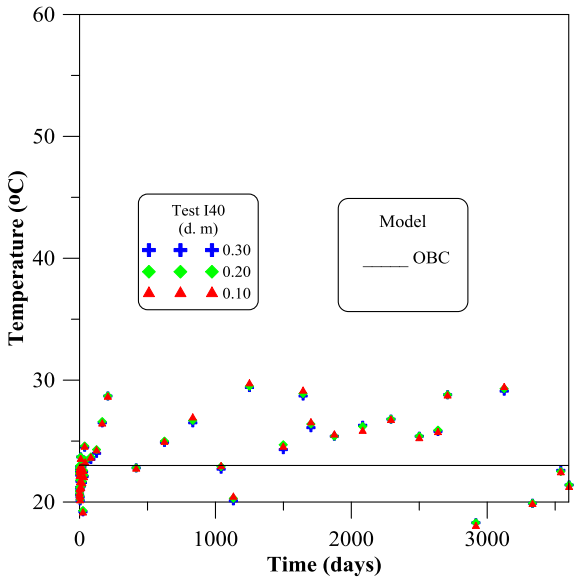

Figure 4.3 Evolution of Temperature for the I40 test: Experimental Data (scatter points) and Model Predictions (OBC) up to 3600 days (10 years) at 0.30 m, 0.20 m and 0.10 m from the bottom of the cell.

Figure 4.4 shows the data of relative humidity for the same three locations where the temperature was measured. The first thing observed from the experimental data is an increase in the relative humidity with time in all the positions. This means that a hydration process is taking place and the water is moving from one end to the other by a hydraulic gradient. However, in each location, the relative humidity is increasing at a different rate. The sensor closest to the top (hydration source), is the one showing a higher rate in the measurements. As we move further apart from the hydration source, this rate will be reduced. This is due to the fact that the path for a water particle close to the top will be longer as we move down into the cell and therefore the time for hydration at that location will increase. It is also noted that a fully saturation condition is not achieved in any location of the cell. The sensor closest to the upper end measured a

maximum value close to 93%, the one in the middle 92% and the one near the bottom end 88%.

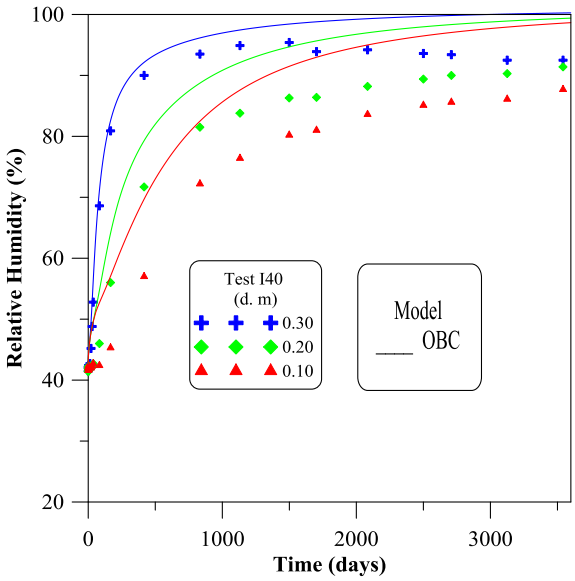

Figure 4.4 Evolution of Relative Humidity for the I40 test: Experimental Data (scatter points) and Model Predictions (OBC) up to 3600 days (10 years) at 0.30 m, 0.20 m and 0.10 m from the bottom of the cell.

Regarding the numerical results for this test, it can be seen that the model produced the general trend of the measurements but does not showed a good agreement with the experimental values. In the top end of the cell, the values of relative humidity are increasing with time up to 2500 days. After that time, the model tends to stabilize, reaching a value of 100% of relative humidity. This means that the OBC is predicting a fully saturation in this part of the cell after 3000 days approximately. In the middle of the cell (0.20 m), there is also an increase in relative humidity with time but at a lower rate. Here the model predicts a value of around 99% of relative humidity at 10 years, very close to saturation. The bottom part of the cell (0.30 m) shows a very similar behavior,

increasing the relative humidity with time but with a lower rate than the other two positions. In this location, the predicted value of relative humidity after 10 years is close to 98%. In the long term, it is expected that the model will predict values of 100% of relative humidity at the center and at the bottom of the bentonite as Figure 4.5 shows. In other words, a steady state condition will be achieved when the complete cell becomes fully saturated.

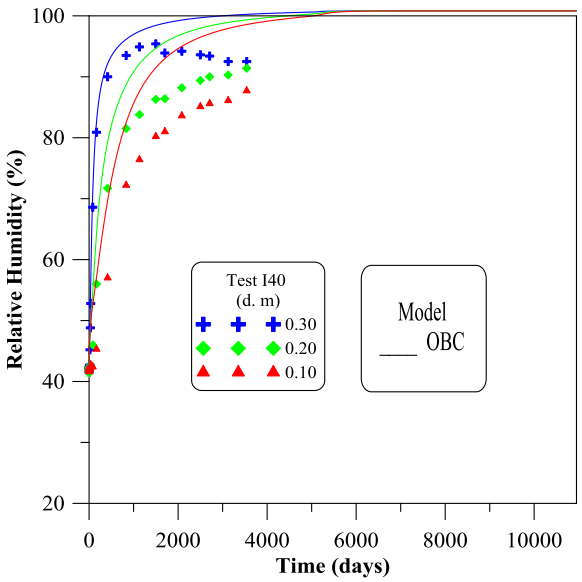

Figure 4.5 Evolution of Relative Humidity for the I40 test: Experimental Data (scatter points) and Model Predictions (OBC) up to 10950 days (30 years) at 0.30 m, 0.20 m and 0.10 m from the bottom of the cell.

If we compare the experimental values with the predicted ones, it is evident that there has been an overestimation by the model in all the positions. The numerical simulations are predicting higher hydration rates than the real ones and also showing values of relative humidity closer to saturation. This is one of the main issues found in the literature and discussed previously in section 1.1.

Figure 4.6 presents the experimental values and model predictions of temperature for the GT40 test. In this test, as it was mentioned previously, in addition to the hydration from the upper part of the cell, the bottom end is heated at a temperature of 100°C. Due to the difference in temperature between both ends, a thermal gradient is expected. Average temperatures near the 51°C were recorded by the sensor closest to the heater (0.10 m) while values around the 29°C close to the hydration source (0.30 m). In the middle of the cell (0.20 m), an average intermediate value of 36°C was measured.

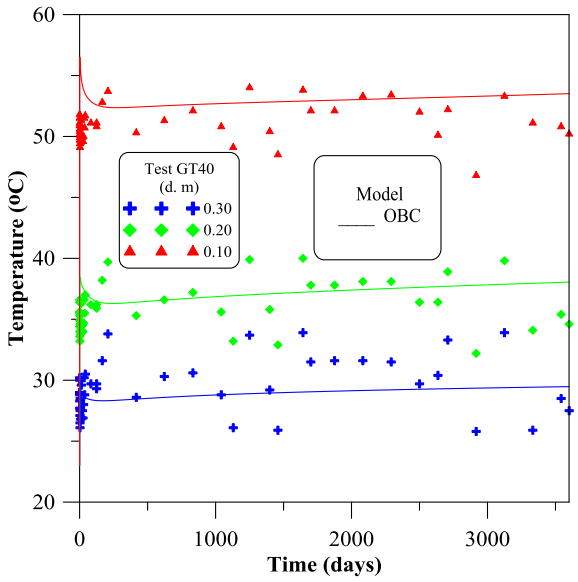

Figure 4.6 Evolution of Temperature for the GT40 test: Experimental Data (scatter points) and Model Predictions (OBC) up to 3600 days (10 years) at 0.30 m, 0.20 m and 0.10 m from the bottom of the cell.

In general, the model captures satisfactorily the average measured temperatures for each position. It is also observed that there is a slightly increase of the predicted temperature values with time in all the positions. It is evident that there is a movement of heat from the bottom of the cell to the upper part, leading to the increase in temperature

simulated by the model. This increase in temperature is expected to continue in the long term having an effect in the hydration of the bentonite as Figure 4.7 shows.

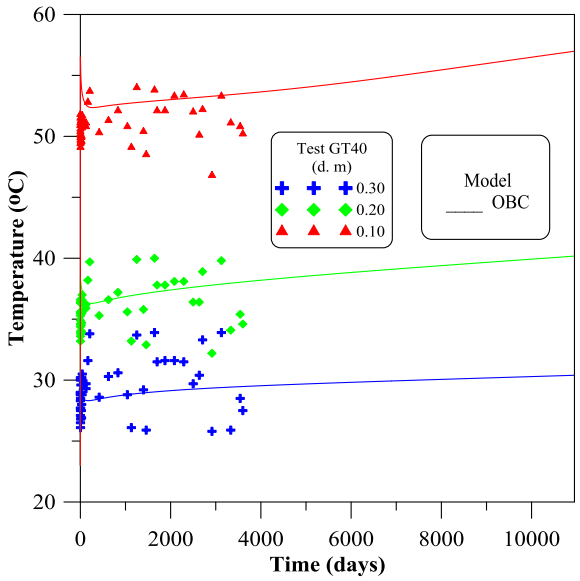

Figure 4.7 Evolution of Temperature for the GT40 test: Experimental Data (scatter points) and Model Predictions (OBC) up to 10950 days (30 years) at 0.30 m, 0.20 m and 0.10 m from the bottom of the cell.

The experimental data and numerical results of relative humidity for the GT40 test are showed in Figure 4.8. Taking a look at the measurements, it is observed that the trend is not the same in the three locations. The data recorded by the sensor located near the top of the cell (0.30 m), has a similar pattern to the one observed in the I40 test. However, the hydration rate is lower than the one observed in the isothermal test because of the thermal gradient effect. In addition, a fully saturation condition is not achieved in this position as the sensor registered a maximum value of 93%. In the mid-section of the cell (0.20 m), it is also noted an increase in the values of relative humidity but with a lower rate. A value of 80% was measured close to the end of the test, implying that the

cell in this location remained unsaturated. The location closest to the heater shows a very particular behavior. In the first 300 hours (approximately 12 days) of the test, the sensor (0.10 m) captured an increase in the measured values. In the following days, the measurements started to decrease to values around 35%. This drop in relative humidity is due to desiccation of the clay that is close to the heat source. However, the movement of water as vapor enhances the hydration process and an increase in relative humidity was recorded later on. This part of the cell is the one with the lowest hydration rate and therefore a maximum value of 43% was recorded. This implies that under these conditions, it is expected that the bentonite will remain unsaturated for many years.

The numerical results of relative humidity for this test, based on the OBC model, does not show the same trend as the experimental data points. In the top of the cell (0.30 m), the model seems to capture the tendency of the measurements at the beginning of the test. However, after some time (around 300 days), the model over predicts the hydration rate in this part of the cell. By the end of the test, as in the I40 test, the model showed a value of 100% of relative humidity. In the center of the cell (0.20 m), the simulation shows also an over prediction of the experimental values. The maximum value of relative humidity predicted by the model was around 99%. Finally, for the section closer to the heat source (0.10 m), the curve seems to have the same shape as the data points, still it can be observe a higher over estimation by the model; reaching a final value of 89%.

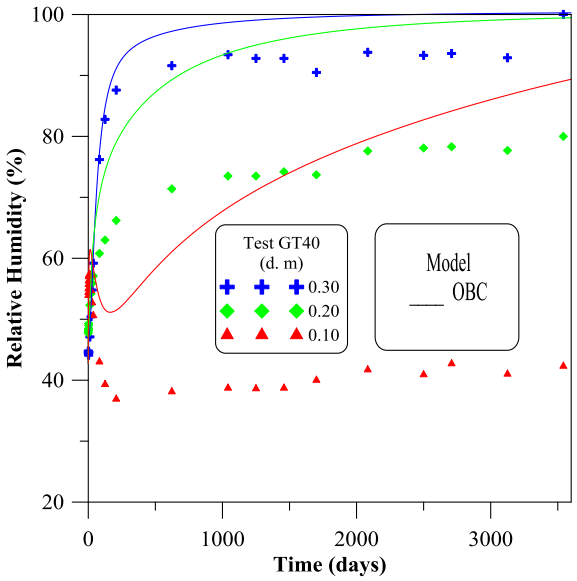

Figure 4.8 Evolution of Relative Humidity for the GT40 test: Experimental Data (scatter points) and Model Predictions (OBC) up to 3600 days (10 years) at 0.30 m, 0.20 m and 0.10 m from the bottom of the cell.

In the long term, the model predicts a fully saturation condition close to 8000 days (22 years) according to Figure 4.9. However, the low hydration rate showed by the measurements suggests that the time to reach saturation is more than the one predicted by the model.

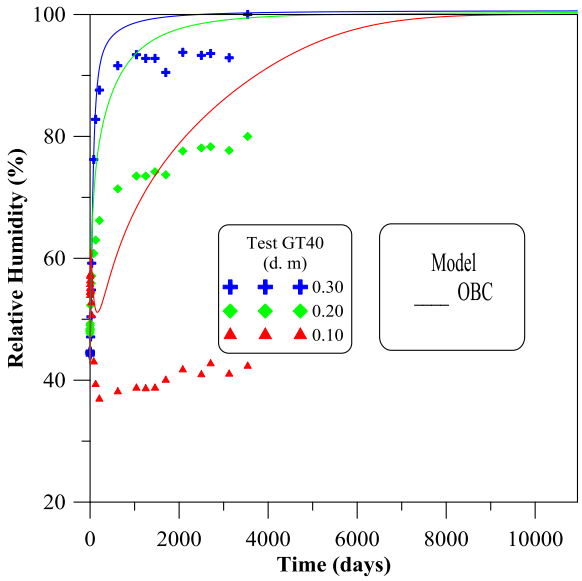

Figure 4.9 Evolution of Relative Humidity for the GT40 test: Experimental Data (scatter points) and Model Predictions (OBC) up to 10950 days (30 years) at 0.30 m, 0.20 m and 0.10 m from the bottom of the cell.

In general, we can say that the OBC model was not able to completely explain the behavior observed in the infiltration tests. In all the positions, the model over-estimated the data points giving a faster hydration rate. The low hydration rate is evident and therefore, there is a need to include other approaches to this basic case. In an effort to achieve that, other cases are presented.

4.2.2 Threshold Hydraulic Gradient

In the numerical analysis, the general, mechanical, hydraulic and thermal parameters used for this case, are the same as the ones in the OBC. However, for the THG case, the following considerations have been taking into account: a value for the

threshold gradient, a critical gradient around 1500 based on experimental evidence that showed that this gradient was around 1000 (Villar and Gómez-Espina, 2009) and a power law for the range of hydraulic gradients with non-Darcian's flow.

Table 4.5 shows the parameters used in the power law to simulate the I40 infiltration test. In addition, a graphical representation of this law with the Darcy's relationship is shown in Figure 4.10.

Table 4.5 Parameters used in the threshold hydraulic gradient power law to simulate the isothermal infiltration test.

Parameter	**Value**
J_0	**5**
power	**180**

Figure 4.11 presents the experimental measurements of relative humidity in the I40 test along with the numerical results obtained from the THG and OBC. The values predicted by the THG in all the positions are much lower than the measured ones. Maximum relative humidity values of 87%, 80% and 76% were predicted by the model for the sensors located at 0.30 m, 0.20 m and 0.10 m from the bottom of the cell respectively. In the long term, the model estimates a small increase in these values but does not predict a fully saturation condition at 30 years of hydration as Figure 4.12 shows. The parameters in Table 4.5 were used to control the hydration rate in the cell by controlling the shape and the slope of the curves obtained by the model.

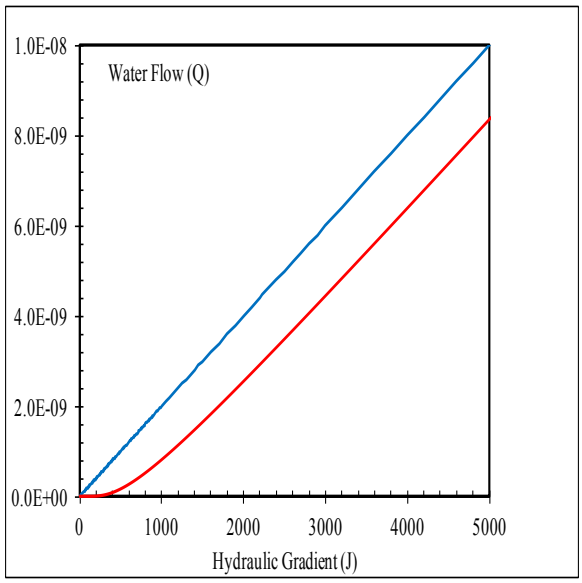

Figure 4.10 Graphical representation of Darcy's law (blue line) and power law (red line) used during the numerical analysis for the isothermal infiltration test.

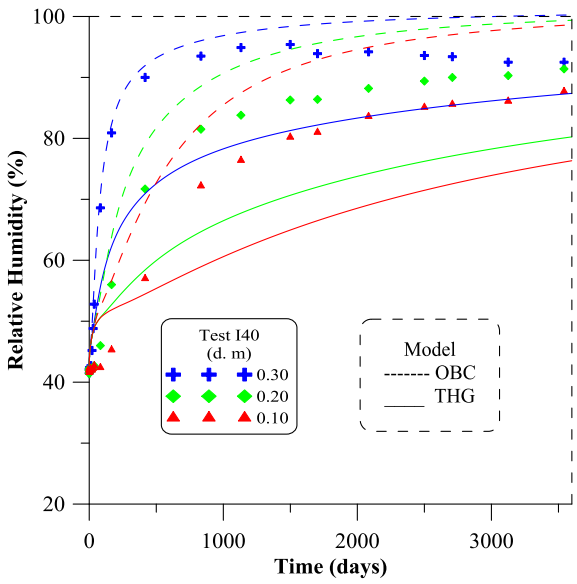

Figure 4.11 Evolution of Relative Humidity for the I40 Test: Experimental Data (scatter points) and Model Predictions up to 3600 days (10 years) for the (THG) and (OBC) cases at 0.30 m, 0.20 m and 0.10 m from the bottom of the cell.

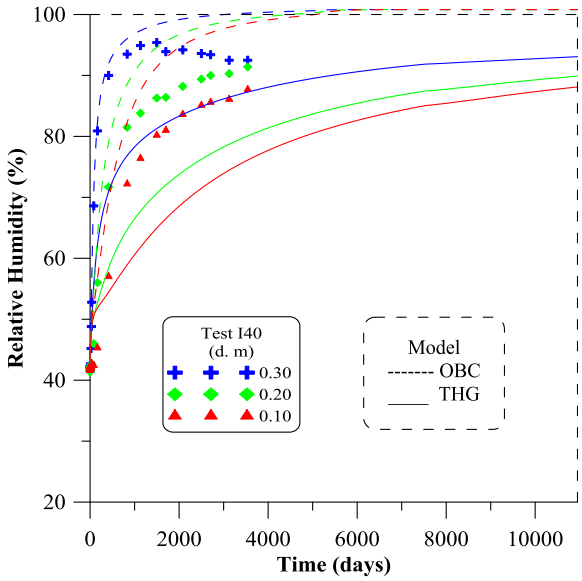

Figure 4.12 Evolution of Relative Humidity for the I40 Test: Experimental Data (scatter points) and Model Predictions up to 10950 days (30 years) for the (THG) and (OBC) cases at 0.30 m, 0.20 m and 0.10 m from the bottom of the cell.

The same approach was used to simulate the GT40 test. However, different parameters were determined in order to fit the experimental measurements. Table 4.6 shows the parameters obtained from the numerical analysis. A graphical representation of the power and Darcy's law is presented in Figure 4.13.

Table 4.6 Parameters used in the threshold hydraulic gradient power law to simulate the non-isothermal infiltration test.

Parameter	**Value**
J_0	**50**
Power	**180**

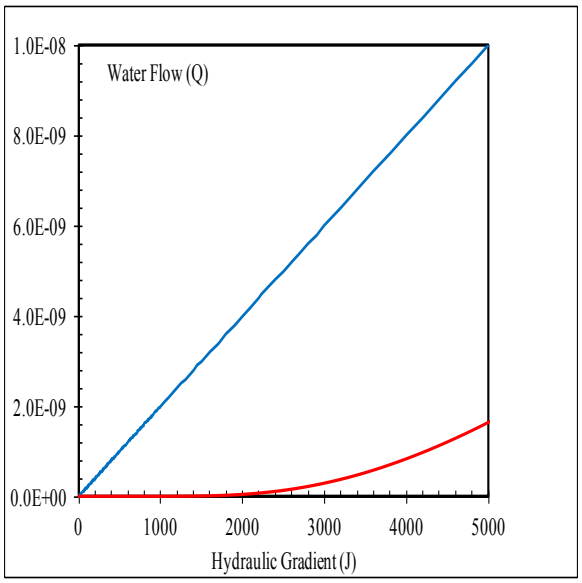

Figure 4.13 Graphical representation of Darcy's law (blue line) and power law (red line) used during the numerical analysis for the isothermal infiltration test.

If we compare the parameters in Table 4.6 with the ones used in the I40 test, we can see that the power is still the same and the threshold hydraulic gradient has changed. The gradient resulted to be ten times larger than the one used in the isothermal test. This increase led to a decrease in the water flow rate as Figure 4.13 shows.

The following figures present the measured and predicted values of temperature and relative humidity for the thermal test (GT40). Figure 4.14 shows a good agreement between the experimental and numerical results. In addition, the improvement in the simulations can be noted when we compare this approach (THG) with the previous one (OBC). The THG seems to predict more stable values of temperature than the OBC, reporting average quantities near the 28°C, 36°C and 53°C for locations at 0.30 m, 0.20 m and 0.10 m from the heater, respectively. It is also noted that the predicted values of temperature remained constant in the long term, as Figure 4.15 shows.

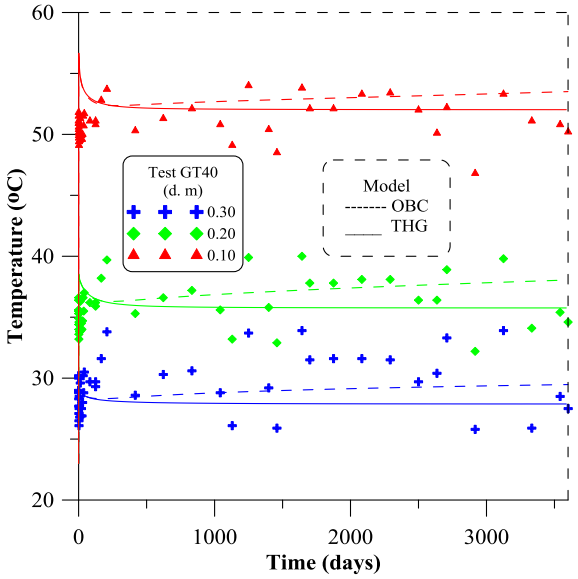

Figure 4.14 Evolution of Temperature for the GT40 Test: Experimental Data (scatter points) and Model Predictions up to 3600 days (10 years) for the (THG) and (OBC) cases at 0.30 m, 0.20 m and 0.10 m from the bottom of the cell.

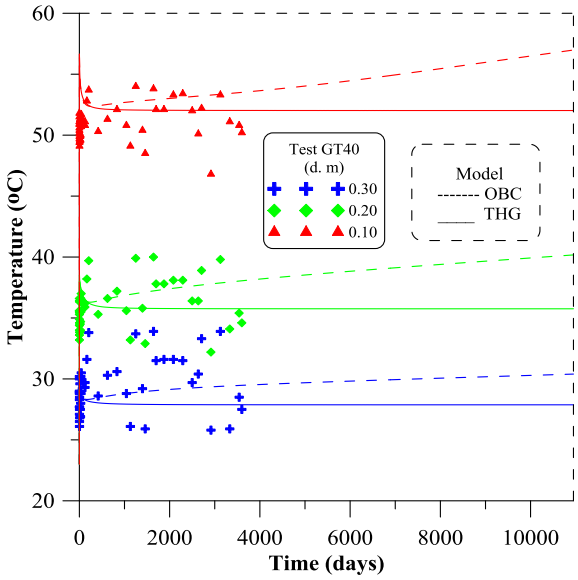

Figure 4.15 Evolution of Temperature for the GT40 Test: Experimental Data (scatter points) and Model Predictions up to 10950 days (30 years) for the (THG) and (OBC) cases at 0.30 m, 0.20 m and 0.10 m from the bottom of the cell.

The experimental and numerical results of relative humidity are displayed in Figure 4.16. According to this figure, we can observe that the model (THG) capture satisfactorily the trend of the data points in some of the positions. For the position closer to the top of the cell (0.30 m), the curve generated by the model shows a shape similar to the one observed in the data points. However, the measured values are being underestimated. A maximum value of 89% of relative humidity at the end of the test was predicted.

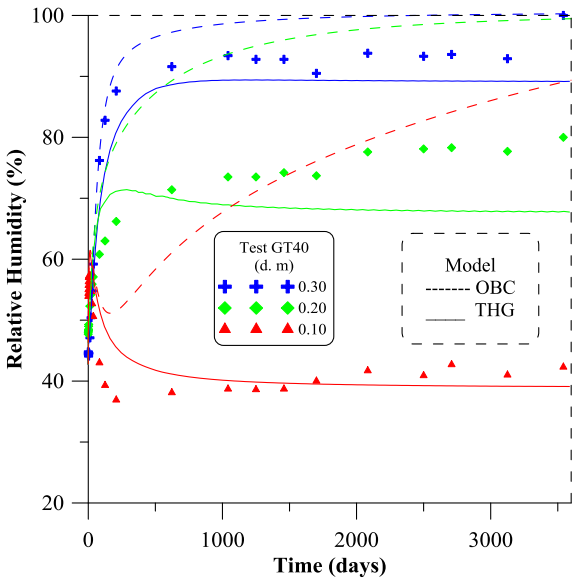

Figure 4.16 Evolution of Relative Humidity for the GT40 Test: Experimental Data (scatter points) and Model Predictions up to 3600 days (10 years) for the (THG) and (OBC) cases at 0.30 m, 0.20 m and 0.10 m from the bottom of the cell.

In the center of the cell (0.20 m), in the first 250 days, the model showed a higher rate of hydration than the experimental points leading to an over estimation of the measured values. After that, the rate of hydration decreased and at the end of the test a value of 68% of relative humidity was reported. For the location closest to the heater

(0.10 m), the numerical results obtained were very close to the data points in a range of time between the 1000 days and the end of the test, where a value of 39% was reached. It should be note also, the effect of the threshold hydraulic gradient when we compare the numerical results from this model to the ones obtained from the OBC. In this case, for the sensors located in the top and center of the cell, the model predicts an increase in the values of relative in the first 750 days. After that time, the simulations show a steady state condition where the values remain practically constant. In the sensor closest to the bottom of the cell, the model was able to capture satisfactorily the drying produced by the heater by showing a decrease in the predicted values. Later on, the model also shows a steady state condition. This steady state condition remains in the long term as Figure 4.17 shows.

In summary, there was an improvement in the numerical predictions of temperature and relative humidity. The incorporation of the threshold hydraulic gradient in the modeling allowed reproducing better the hydration rate in the bentonite by the introduction of the power law. However, there is still a significant difference between the measured and predicted values like the under estimation observed in the isothermal test and the steady state condition simulated by the model in the non-isothermal case.

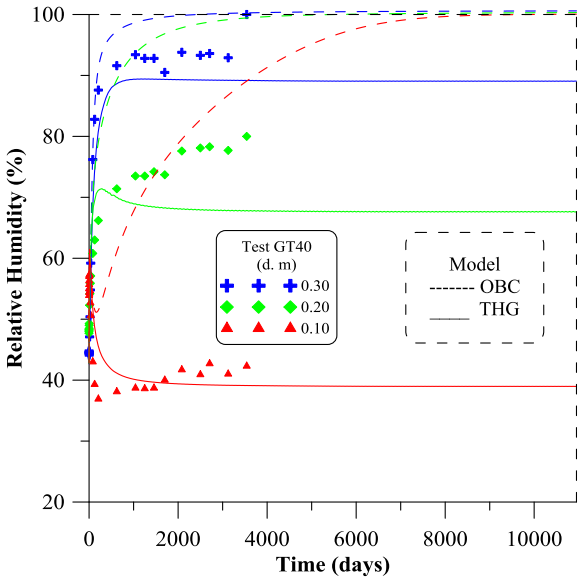

Figure 4.17 Evolution of Relative Humidity for the GT40 Test: Experimental Data (scatter points) and Model Predictions up to 10950 days (30 years) for the (THG) and (OBC) cases at 0.30 m, 0.20 m and 0.10 m from the bottom of the cell.

4.2.3 Thermo-Osmosis

The thermo-osmosis phenomenon will not take place in the isothermal case (I40 test) due to absence of thermal gradient (Figure 4.18). If we compare the numerical results obtained from the THO with the ones from the OBC, it can be noted that they are almost the same. It is important to recall that in order to have the thermo-osmosis, a difference in temperature needs to occur. Therefore, it is expected that in this case with isothermal conditions, the water will only move by a hydraulic gradient and as a result, the outputs from the simulations were equal to the base case.

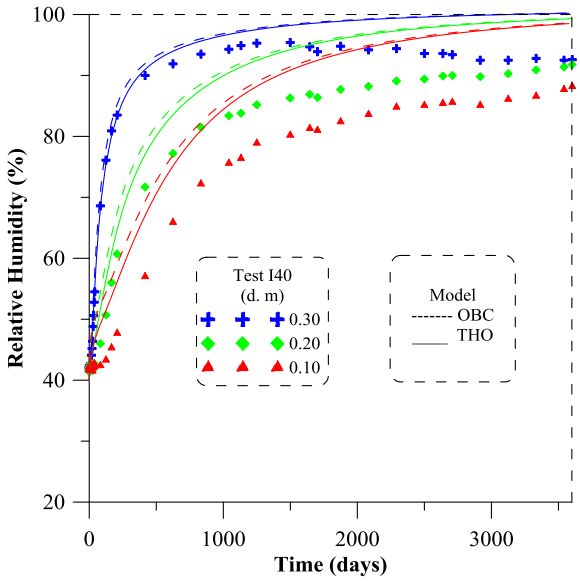

Figure 4.18 Evolution of Relative Humidity for the I40 Test: Experimental Data (scatter points) and Model Predictions up to 3600 days (10 years) for the (THO) and (OBC) cases at 0.30 m, 0.20 m and 0.10 m from the bottom of the cell.

In the thermal test (GT40), a temperature gradient is present due to the heating at the bottom of the cell. It has been demonstrated that in addition to the hydraulic gradient, the water can be move also by a thermal gradient. This particular movement of water goes from high to low temperature zones (Gurr et al., 1952). For this kind of test, we can expect a movement of water in two directions and by two different mechanisms. In one direction, the water (as liquid) will move from the top to the bottom of the cell driven by the hydraulic gradient. If thermo-osmosis is present, water will also move from bottom to top in the liquid phase driven by temperature gradient.

It is important to mention the lack of experimental data for FEBEX bentonite regarding the coefficient associated to the thermo-osmotic flow. Based on already published data for other materials (Soler, 1999; Djeran, 1993), the thermo-osmotic

constant adopted in the numerical analysis is 5.60 x 10^{-12} m^2/K/s. The general, mechanical, hydraulic and thermal parameters still the same as those used in the OBC case.

The following figures show the numerical results obtained from the THO and OBC cases with the experimental data of temperature and relative humidity. In Figure 4.19, the predicted values of temperature given by the model are lower than the ones given by the OBC. The movements of liquid water from the hot zone to the cold one induce a decrease of temperature, which is more marked near the heater. However, according to the model, the temperature will remain constant in the long term as Figure 4.20 shows.

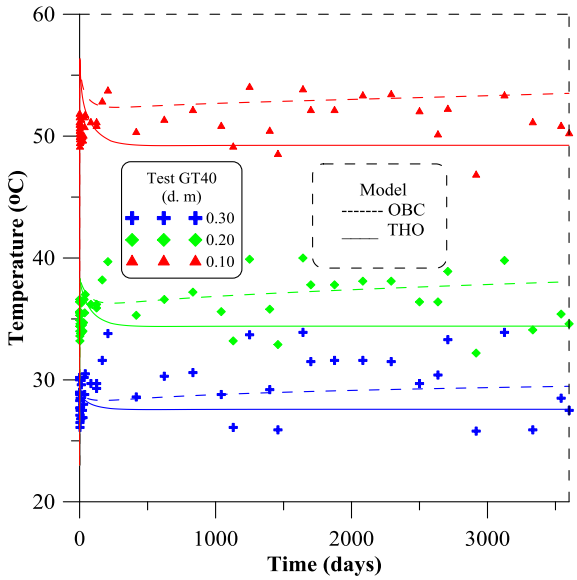

Figure 4.19 Evolution of Temperature for the GT40 Test: Experimental Data (scatter points) and Model Predictions up to 3600 days (10 years) for the (THO) and (OBC) cases at 0.30 m, 0.20 m and 0.10 m from the bottom of the cell.

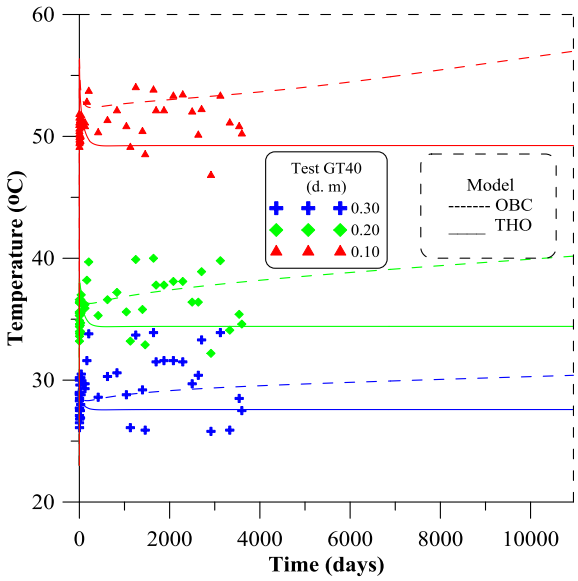

Figure 4.20 Evolution of Temperature for the GT40 Test: Experimental Data (scatter points) and Model Predictions up to 10950 days (30 years) for the (THO) and (OBC) cases at 0.30 m, 0.20 m and 0.10 m from the bottom of the cell.

Figure 4.21 presents the outputs for the values of relative humidity in the GT40 test. In general, the predicted values are closer to the data points and the behavior observed inside the cell is well captured by the model (THO). In the upper end of the cell (0.30 m), it is possible to see that during the first days of the test, the measured values are very well reproduced. However, as the time increases, a small overestimation can be noted. On the other hand, in the middle of the cell, the values are being over predicted and as the time increases, the model gets closer to the experimental values. For the location closest to the heater, the desiccation process during the first days of the experiment was well captured by the model. Conversely, the hydration that occurs after has been underestimated. Figure 4.22 shows the long term predictions of the model indicating that after 30 years, the bentonite still unsaturated.

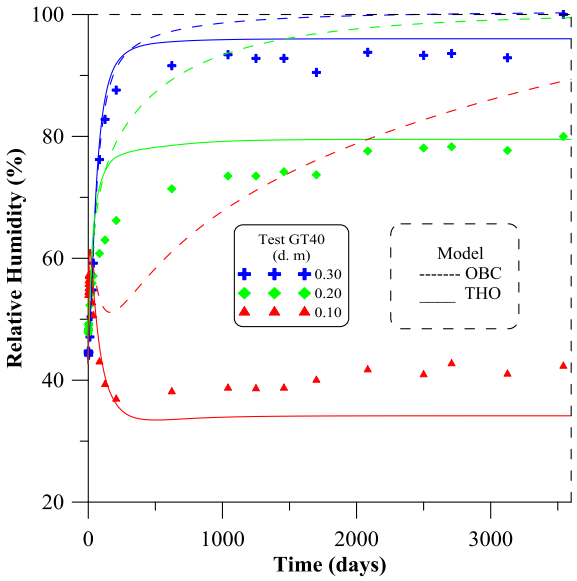

Figure 4.21 Evolution of Relative Humidity for the GT40 Test: Experimental Data (scatter points) and Model Predictions up to 3600 days (10 years) for the (THO) and (OBC) cases at 0.30 m, 0.20 m and 0.10 m from the bottom of the cell.

In general terms, the thermo-osmosis case can explain the movement of water in the bentonite by the two principal mechanisms: the hydraulic and thermal gradients. The first one, moving the water as liquid from the top (cold section) to the bottom (hot section) of the cell by the difference in liquid pressures and the second one, moving the water in the liquid phase from the bottom of the cell to the top by gradients of temperature. The inclusion of these phenomena to the analysis improved the performance of the model resulting in satisfactory predictions of the experimental measurements.

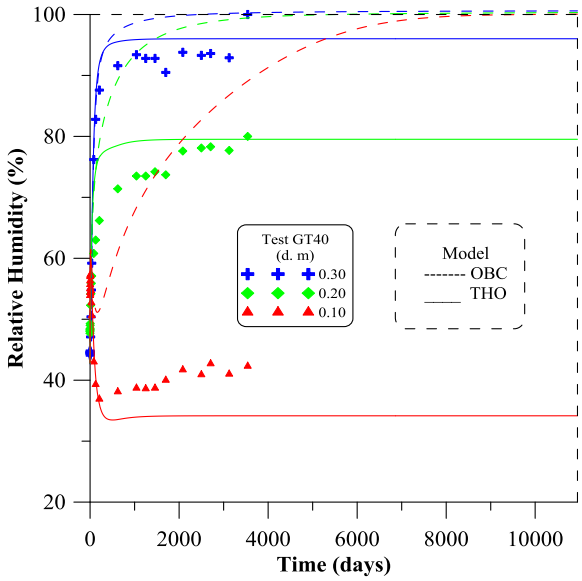

Figure 4.22 Evolution of Relative Humidity for the GT40 Test: Experimental Data (scatter points) and Model Predictions up to 10950 days (30 years) for the (THO) and (OBC) cases at 0.30 m, 0.20 m and 0.10 m from the bottom of the cell.

4.2.4 Double Structure

The Double Structure (DS) approach explained in section 3.3 is used to perform the numerical analysis in the infiltration tests. The general, mechanical, hydraulic and thermal parameters are included in Tables 4.7, 4.8, 4.9 and 4.10 respectively.

Table 4.7 General parameters used in the DS case to perform the numerical analysis for the 1D infiltration tests.

Parameter	Value
ρ_{db}	**1.74**
ρ_{dg}	**1.70**
ω	**14.00**
G_S	**2.72**
e_{total}	**0.563**
e_{micro}	**0.450**
e_{macro}	**0.113**
ϕ_{micro}	**0.288**
ϕ_{macro}	**0.072**
ϕ_{total}	**0.360**

Table 4.8 Mechanical parameters used in the DS case to perform the numerical analysis for the 1D infiltration tests.

Parameter	Value	Parameter	Value
ki0	**0.005**	xlam0	**0.080**
ks0	**0.001**	r	**0.900**
K_min	**0.100**	beta	**0.200**
phimin	**0**	roh	**0.200**
xnu	**0.400**	k	**0.100**
alphass	**0**	pc	**0.500**
alphais	**0**	M	**1.00**
alphasp	**0**	alpha	**0.530**

Table 4.8 Continued

Parameter	Value	Parameter	Value
pref	**0.010**	e0	**0.113**
alph0	**1.00E-05**	p0ast	**6.00**
tref	**20**		

Table 4.9 Hydraulic parameters used in the DS case to perform the numerical analysis for the 1D infiltration tests.

Parameter	Value	Parameter	Value
p0d (MPa)	**7**	psec	**1100**
sigma0	**0.072**	lambda2	**2.1**
lamdad	**0.1**	Kxx int. perm.	**5.00E-20**
srl	**0**	Kyy int. perm.	**5.00E-20**
sls	**1**	Kzz int. perm.	**5.00E-20**
p	**0**	Initial porosity	**0.14**
d	**0**	Minimum	**0.001**
sd	**0**	b	**50**

Table 4.10 Thermal parameters used in the DS case to perform the numerical analysis for the 1D infiltration tests.

Parameter	Value
λ_{dry}	**0.47**
λ_{wet}	**1.15**

The following figures show the numerical results obtained using the Double Structure model to simulate the experimental measurements of temperature and relative humidity on the isothermal and thermal tests. Figure 4.23 presents the results of relative humidity for the I40 (isothermal) test. According to this figure, the model can capture the general trend of the measurements with some discrepancy in the prediction of the real values. If we compare this model with the OBC, it can be seen that the DS model has a better prediction of the hydration rate in the three locations along the cell. This can be also seen in Figure 4.24 where the long term predictions are shown. The values of relative humidity increase with time and after 30 years, the bentonite still unsaturated. The hydration rate can be managed by the use of the permeability exponential law (Equation 3.19) where the reference porosity is the primary factor affecting the permeability of the sample. In the same way, the permeability has an effect in the flow of liquid water. However, all these parameters were determined previously from different permeability tests for this particular soil and may not be changed. On the other hand, the parameter b in Equation 3.19 can be changed to obtain a better fit of the data points. In other words, the permeability exponential law can be very useful to predict the hydraulic behavior of a certain soil by iteratively changing the parameters involved.

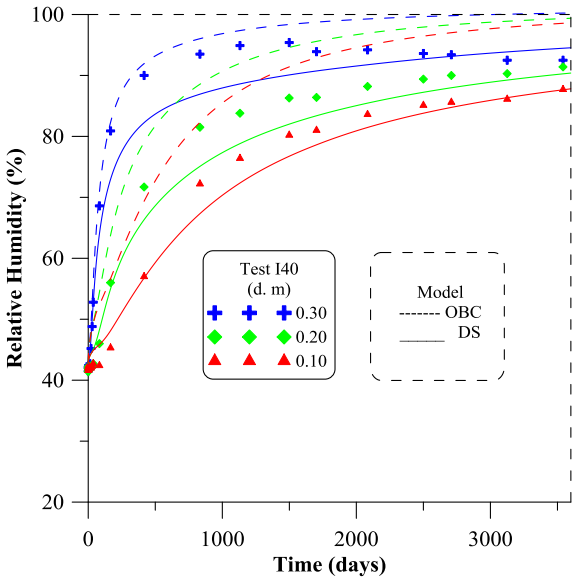

Figure 4.23 Evolution of Relative Humidity for the I40 Test: Experimental Data (scatter points) and Model Predictions up to 3600 (10 years) for the (DS) and (OBC) cases at 0.30 m, 0.20 m and 0.10 m from the bottom of the cell.

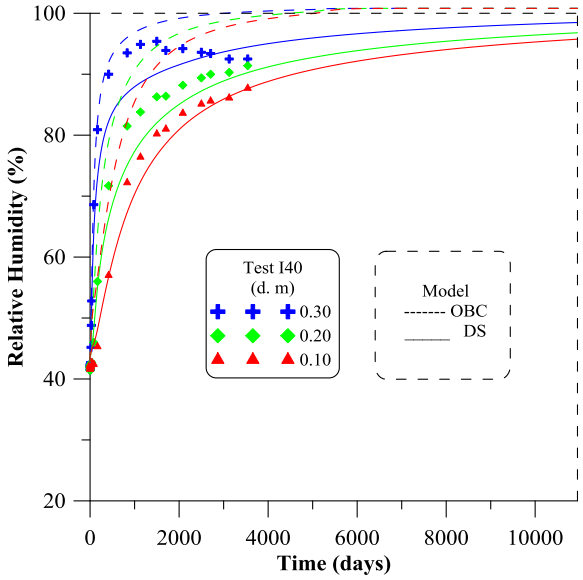

Figure 4.24 Evolution of Relative Humidity for the I40 Test: Experimental Data (scatter points) and Model Predictions up to 10950 (30 years) for the (DS) and (OBC) cases at 0.30 m, 0.20 m and 0.10 m from the bottom of the cell.

Figures 4.25 and 4.27 present the results from the simulations of temperature and relative humidity for the GT40 (thermal) test, respectively. Figure 4.25 shows how well the model estimates the measured values of temperature in the three locations for the duration of the test. In the position close to the top, the model predicted a temperature near to 29°C, same as the average measured value. In the center of the cell, the temperature reported by the model was around 38°C versus the 36°C measured by the sensor. For the location near the heater, the simulations registered a temperature of 54°C while the sensor measured 51°C. In Figure 4.26 the long term predictions of temperature are shown. The model estimates quite constant temperature values for a period of 30 years close to the average values measured by the sensors.

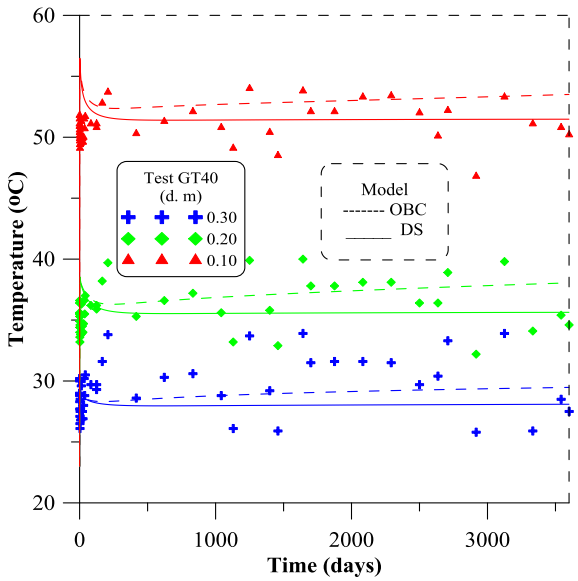

Figure 4.25 Evolution of Temperature for the GT40 Test: Experimental Data (scatter points) and Model Predictions up to 3600 days (10 years) for the (DS) and (OBC) cases at 0.30 m, 0.20 m and 0.10 m from the bottom of the cell.

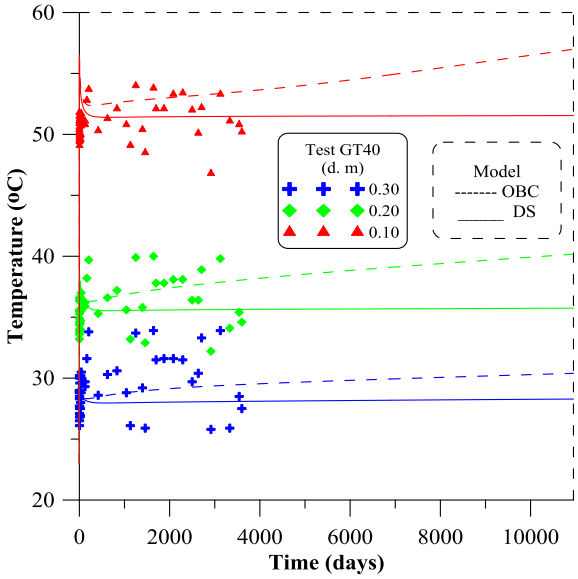

Figure 4.26 Evolution of Temperature for the GT40 Test: Experimental Data (scatter points) and Model Predictions up to 10950 days (30 years) for the (DS) and (OBC) cases at 0.30 m, 0.20 m and 0.10 m from the bottom of the cell.

Regarding the results of relative humidity, the Double Structure simulated very well the behavior observed in the experimental data. The difference between this model and the OBC is also noted. The main difference is that the OBC predicts that the clay will be fully saturated by the end of the test in some parts of the cell while the DS estimates unsaturated conditions through the entire experiment. These conditions will remain in the bentonite for more than 30 years according to the long term model predictions. Figure 4.28 show that only the sensor near to the hydration source will measure 100 % of relative humidity after 30 years. The other two sensors, the one in the center of the cell and the other close to the heater will remain under unsaturated conditions with values of 88 % and 49 % respectively. These unsaturated conditions remain in the sample due to hydro-mechanical coupled phenomena. The main factor is

the fabric of the bentonite, as it was mentioned previously. When the hydration process begins, the micropores will be filled with water and the bentonite expands. This swelling affects the macrostructure by reducing the size of the macropores and as a result there is not enough room for water to flow. Therefore, the hydration rate is reduced significantly.

The numerical results obtained from the Double Structure approach demonstrated that this model has been able to explain the behavior of the bentonite inside the cells. This analysis supports the theory that the fabric of the bentonite has an effect in the hydraulic behavior of this type of clay. However, in an effort to obtain more accurate predictions, this case was combined with the thermo-osmosis phenomenon and a new numerical analysis was performed.

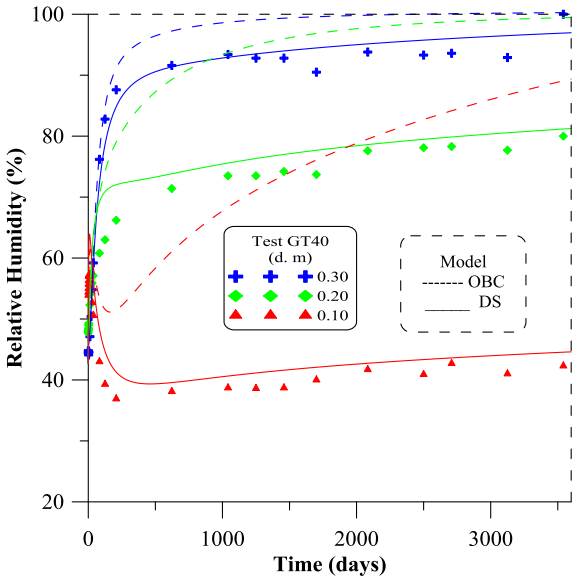

Figure 4.27 Evolution of Relative Humidity for the GT40 Test: Experimental Data (scatter points) and Model Predictions up to 3600 days (10 years) for the (DS) and (OBC) cases at 0.30 m, 0.20 m and 0.10 m from the bottom of the cell.

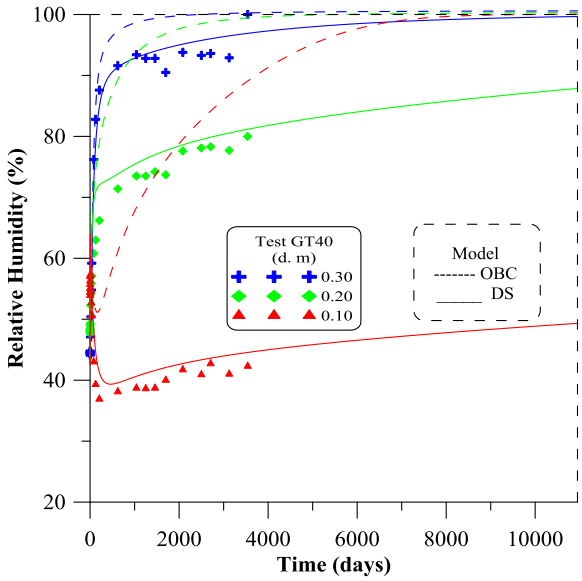

Figure 4.28 Evolution of Relative Humidity for the GT40 Test: Experimental Data (scatter points) and Model Predictions up to 10950 days (30 years) for the (DS) and (OBC) cases at 0.30 m, 0.20 m and 0.10 m from the bottom of the cell.

In addition to the numerical results of temperature and relative humidity, there are other variables that can be considered in the analysis. These variables include the void ratio and liquid degree of saturation.

The void ratio is defined as the ratio of the volume of voids to the volume of solids. This variable is a measurement of the degree of openness in the soil and can be related to its density (high void ratio implies a lower density). In this particular model, where two structural levels are considered, a void ratio for each level can be determined. The void ratio for the macrostructure is defined as the macro void ratio and the void ratio for the micro-structure is called the micro void ratio. On the other hand, the liquid degree of saturation is defined as the ratio of the volume of water to the volume of voids. This property is a measurement of the amount of water inside the pore space. The following

plots show the distribution of these variables along the cell computed for different times up to 10000 days (27 years) for the isothermal and non-isothermal case.

Figure 4.29 shows the distribution of the macro void ratio along the cell for the isothermal case. It can be noted that the macro void ratio is decreasing as the saturation progressed, with higher values near the hydration source. This implies that the volume of the macro-pores has been reduced and the macro-structure has become denser. This densification in the macro-structure is caused by the swelling behavior in the micro-structure as Figure 4.30 shows. In this figure it can be seen that as the hydration continues, the micro void ratio increases. This increase in the micro void ratio is the result of an expansion in the micro-structural level. This swelling occurring at the particle level will partially fill the voids in the macro-structure. Figure 4.31 shows the distribution of the global void ratio along the cell.

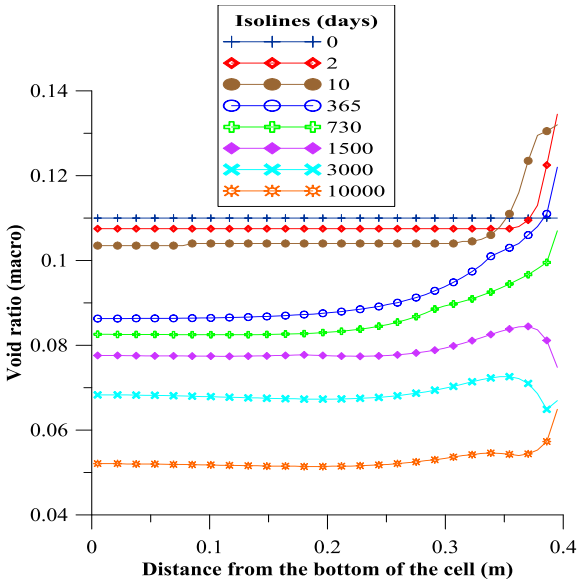

Figure 4.29 Distribution of macro void ratio along the 40 cm infiltration cell for the isothermal case. Model predictions up to 10000 days.

Regarding the results of liquid degree of saturation shown in Figure 4.32, as expected, we observed higher values close to the hydration front and lower values near the bottom of the cell. As the saturation goes on, an increase in the liquid degree of saturation can be observed in all the positions along the cell with a reduction in the hydration rate. In addition, it can be seen the similar shape of these curves with the ones showed by the micro void ratio. These results are in agreement with the adopted conceptual model that considers that a large amount of water is stored inside the micro-structure.

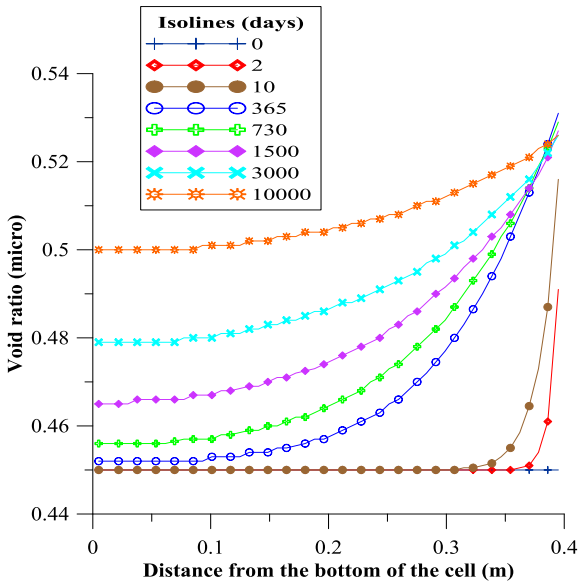

Figure 4.30 Distribution of micro void ratio along the 40 cm infiltration cell for the isothermal case. Model predictions up to 10000 days.

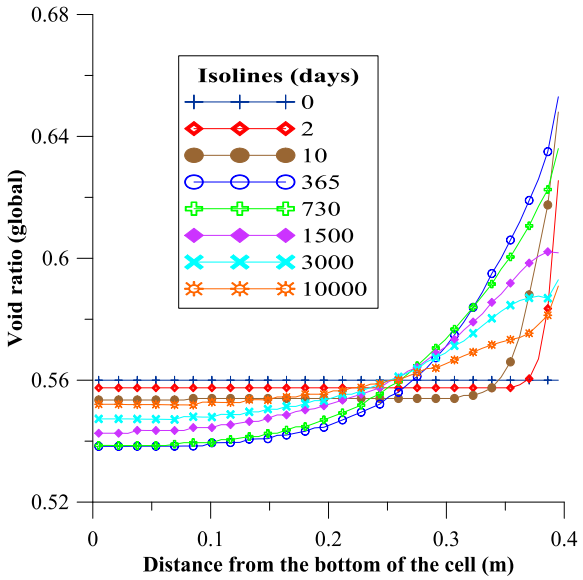

Figure 4.31 Distribution of global void ratio along the 40 cm infiltration cell for the isothermal case. Model predictions up to 10000 days.

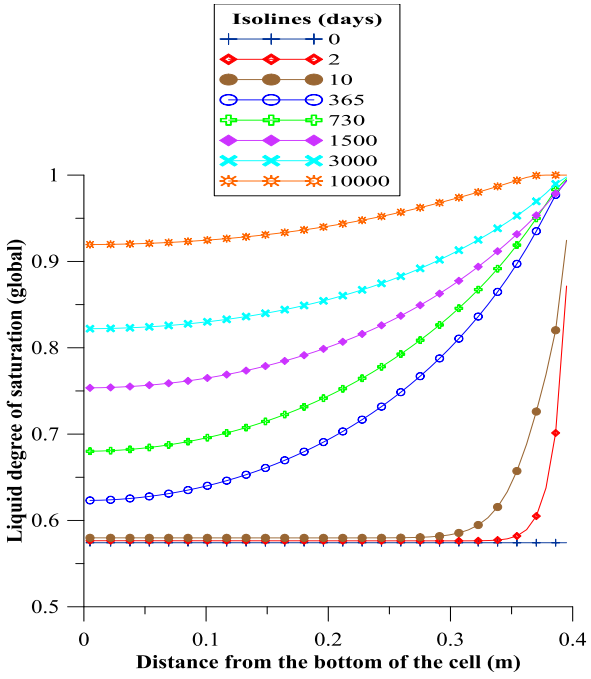

Figure 4.32 Distribution of liquid degree of saturation along the 40 cm infiltration cell for the isothermal case. Model predictions up to 10000 days.

The distribution of the macro void ratio along the cell for the non-isothermal case is shown in Figure 4.33. A swelling behavior can be seen only at the beginning of the test and for a very small zone close to the hydration front. This swelling is due to suction reduction and also to the interaction mechanism between the two structural levels. For other times and positions, the values of macro void ratio are lower than the initial ones. This is caused by micro-structural expansions (see Figure 4.34) in the external zones due to hydration under constant volume conditions. The final condition corresponds to important reductions of the macro-pores along the cell especially near the hydration source. Another important phenomenon to be considered is the macro-structural compression or collapse that can be observed across the cell moving progressively to the bottom of the cell as hydration goes on. The local wetting caused by the condensation of vapor coming from the zones close to the heater, induces a reduction in the macro void ratio. For this case as Figure 4.35 shows, the global void ratio is greater in the zones close to the hydration front and lower near the heater. In that sense, the model reproduces a decrease in the density of the bentonite in zones close to the hydration source, as saturation progresses.

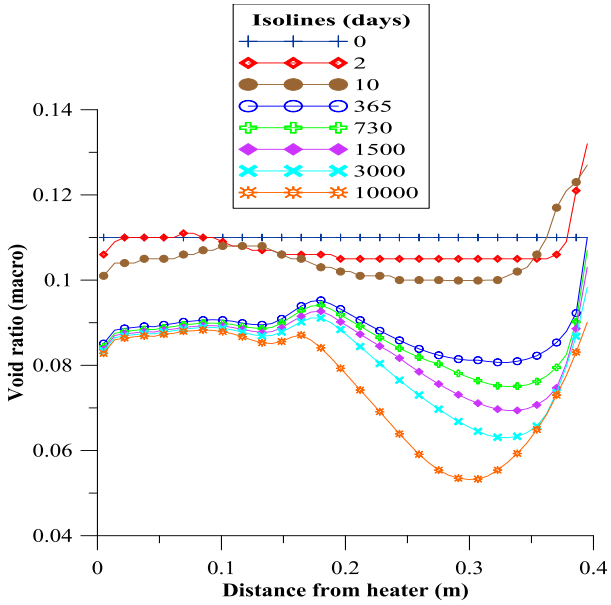

Figure 4.33 Distribution of the macro void ratio along the 40 cm infiltration cell for the non-isothermal case. Model predictions up to 10000 days.

Regarding the results of liquid degree of saturation shown in Figure 4.36, as expected, we observed higher values close to the hydration front and lower values near the bottom of the cell. As the saturation goes on, an increase in the liquid degree of saturation can be observed in all the positions along the cell with a reduction in the hydration rate. In addition, it can be seen the similar shape of these curves with the ones showed by the micro void ratio as occurred in the previous case.

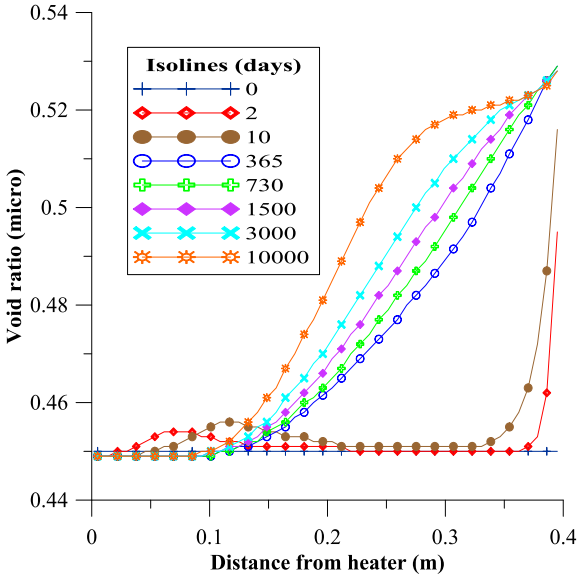

Figure 4.34 Distribution of the micro void ratio along the 40 cm infiltration cell for the non-isothermal case. Model predictions up to 10000 days.

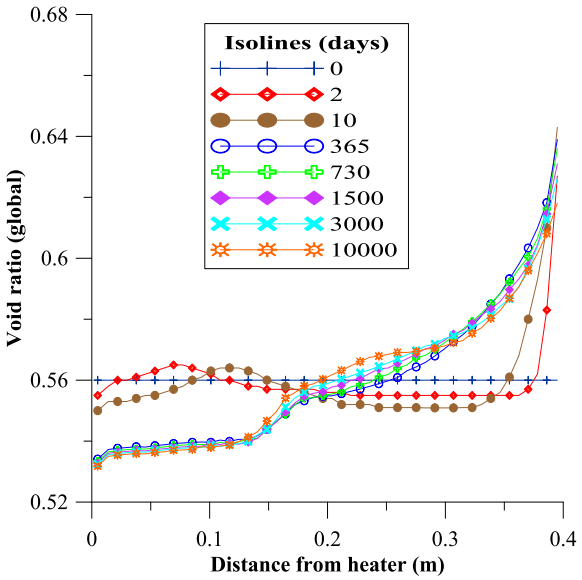

Figure 4.35 Distribution of global void ratio along the 40 cm infiltration cell for the non-isothermal case. Model predictions up to 10000 days.

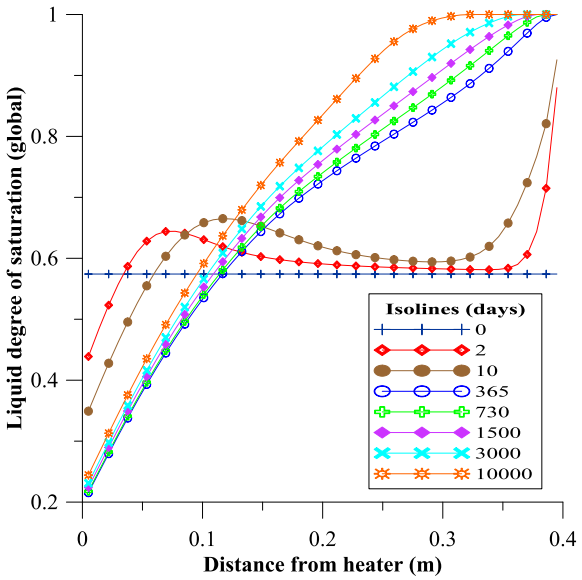

Figure 4.36 Distribution of liquid degree of saturation along the 40 cm infiltration cell for the non-isothermal case. Model predictions up to 10000 days.

4.2.5 Double Structure - Thermo-Osmosis

The last numerical case is presented in this section. This case is based on a combination of the Double Structure and Thermo-osmosis approach. The main objective is to achieve the best possible model to obtain more accurate results. To perform the simulations, the parameters from the two models were combined to obtain the best fit. Since the thermo-osmosis only occurs under thermal conditions, the modeling only covered the GT40 test.

Figure 4.37 shows the evolution of temperature in the different positions along the cell. It is clearly showed that the model predictions of the measured values were very

precise. In the long term, Figure 4.38 shows that predicted values will remain constant through the first 30 years.

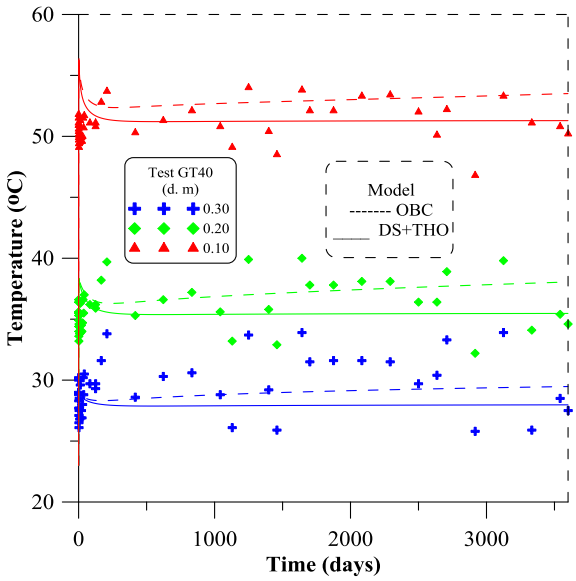

Figure 4.37 Evolution of Temperature for the GT40 Test: Experimental Data (scatter points) and Model Predictions up to 3600 days (10 years) for the (DS + THO) and (OBC) cases at 0.30 m, 0.20 m and 0.10 m from the bottom of the cell.

Figure 4.39 presents the numerical results of relative humidity. It is observe from this figure how well the model can precisely explain the behavior of the bentonite under the experimental conditions. According to the model, the maximum values of relative humidity until the end of the test (10 years) near the top (0.30 m), in the center (0.20 m) and close to the heater (0.10 m) were 97 %, 80 % and 43 % respectively. In the long term (Figure 4.40), after the first 30 years, the model shows almost constant values of relative humidity.

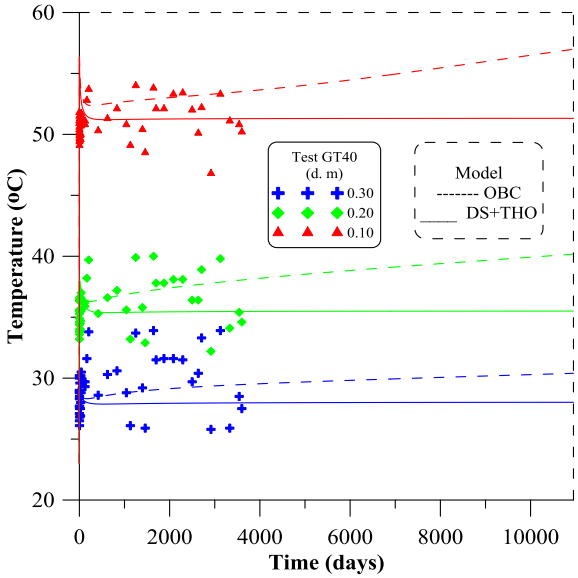

Figure 4.38 Evolution of Temperature for the GT40 Test: Experimental Data (scatter points) and Model Predictions up to 10950 days (30 years) for the (DS + THO) and (OBC) cases at 0.30 m, 0.20 m and 0.10 m from the bottom of the cell.

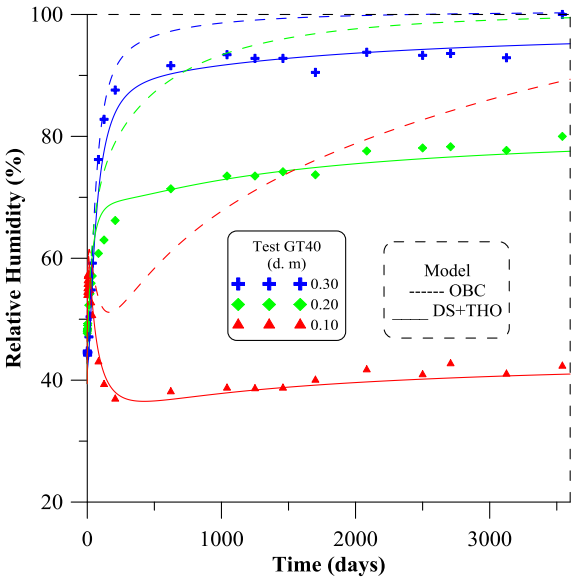

Figure 4.39 Evolution of Relative Humidity for the GT40 Test: Experimental Data (scatter points) and Model Predictions up to 3600 days (10 years) for the (DS + THO) and (OBC) cases at 0.30 m, 0.20 m and 0.10 cm from the bottom of the cell.

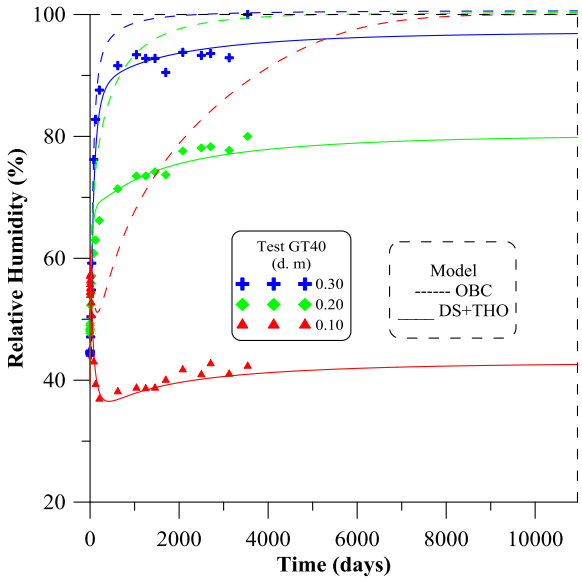

Figure 4.40 Evolution of Relative Humidity for the GT40 Test: Experimental Data (scatter points) and Model Predictions up to 10950 days (30 years) for the (DS + THO) and (OBC) cases at 0.30 m, 0.20 m and 0.10 cm from the bottom of the cell.

The combination of the Double Structure and Thermo-osmosis cases makes this model capable to reproduce the thermo-hydro-mechanical (THM) phenomena observed in the infiltration test under non-isothermal conditions.

5. THE MOCK-UP TEST

The infiltration tests carried out at CIEMAT laboratories and discussed in the previous section together with the laboratory experiments presented in section 2 are mainly used to complete the information obtained from two other large scale tests: the in-situ test and the mock-up test. The full scale in-situ test operates under natural conditions at the underground laboratory at the Grimsel test site in Switzerland while the mock-up test is performed at almost full scale under well controlled initial and boundary conditions at CIEMAT facilities in Madrid, Spain. These all three tests are part of the FEBEX project whose main goal is to study the behavior of the barrier components in the near field of a high level radioactive waste repository in crystalline rock.

In this section, a full description of the main components and operation of the mock-up test will be discussed. In addition, the experimental measurements of temperature, relative humidity, water intake and total pressure will be compared with the model predictions obtained from the THM formulation. The numerical results will be divided into four cases based on the approach used: Operational Base Case (OBC), Threshold Hydraulic Gradient (THG), Thermo-osmosis (THO) and Double Structure (DS).

5.1 Description Of The Mock-Up Test

The mock-up test simulates almost at full scale the components of the engineered barrier system (EBS) based on the Spanish disposal reference concept which consists on placing the waste canisters horizontally in drifts surrounded by a clay barrier made from highly bentonite blocks. In this experiment the heterogeneities of the natural system are avoided, the hydration process is controlled and the boundary conditions are better defined than in the in-situ test. This facilitates the verification of the predictive capacity of the numerical codes developed to analyze the behavior of the near field, as only the behavior of the barrier is considered (ENRESA, 2000).

The main components of the mock-up test consist of five basic units: the confining structure with its hydration system, the clay barrier, heat system and heater control system (HCS), instrumentation and data acquisition system (DAS). Figure 5.1 shows a schematic representation of the mock-up test with all of its physical components.

5.1.1 Confining Structure And Hydration System

The confining structure is a cylindrical body made of carbon steel with an inner length of 6.00 m and an internal diameter of 1.62 m. The surface of the cylindrical structure is perforated in 234 points: 186 for the exit of sensor cables and 48 for water injection that connect the cylindrical body with the hydration system.

The hydration system consists of two stainless steel tanks 3.0 m height and 0.8 m in diameter with a total capacity of 1.3 m^3. The system injects granitic water with a salinity of 0.02 % and a pH of 8.3 for hydration of the bentonite at a constant and controlled pressure of 0.55 MPa. In order to homogenize the water supply along the periphery of the clay barrier, the internal surface of the confining structure is covered with several layers of geotextile.

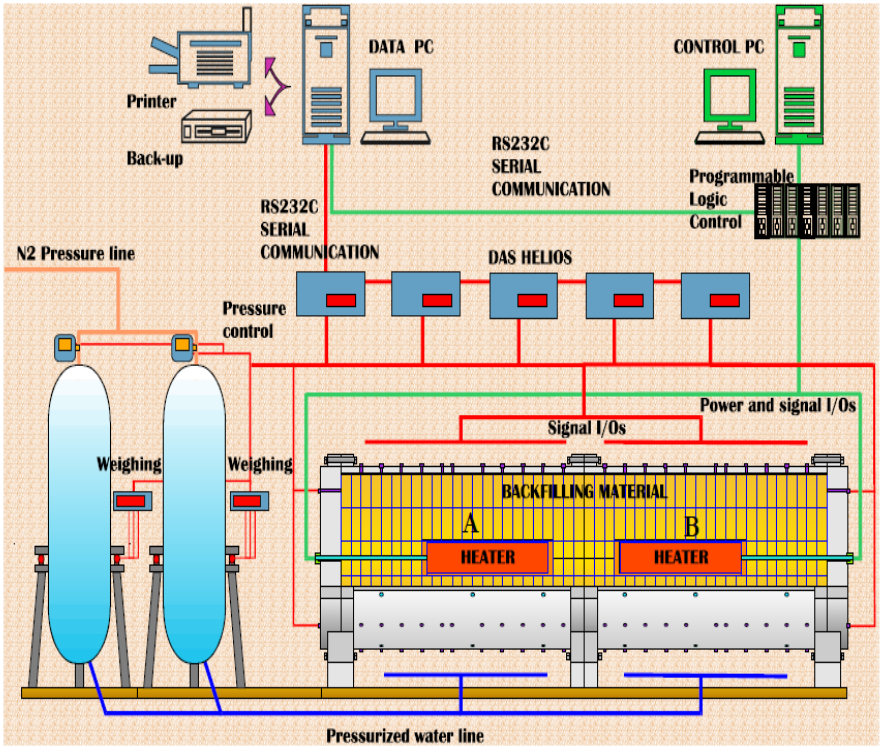

Figure 5.1 General scheme of the mock-up test (ENRESA, 2000).

5.1.2 Clay Barrier

The clay barrier is formed from highly compacted blocks of FEBEX bentonite. In total 25870 kg of bentonite were compacted to manufacture 1012 blocks. The blocks were fabricated with an average water content of 13.6 % and average dry density of 1.65 g/cm^3.

5.1.3 Heat System And HCS

The heat system consists of two carbon steel cylindrical heaters with the corresponding monitoring and control systems. Each heater is 1.62 m long and has a 0.34 m diameter. In this experiment, the heaters are in contact with the bentonite barrier having a 0.75 m horizontal separation between them. The heaters are capable of individually supply the thermal power necessary to maintain a constant temperature of 100 °C in the heater/bentonite interface.

The HCS consists of all the electrical, electronic components and computer programs for the automatic supervision of the operation and control of the power supply to the heaters, data acquisition and activation of the processes and alarms in the event of failure of any of the components (heater resistor, electronics, etc.). The control parameter for the heating is either the temperature or the supplied power. In the event of failure of any of the heating elements, the control system compensates by using the rest

of the heating elements. The nine sensors installed in each heater allow internal temperature distributions to be observed.

5.1.4 Instrumentation And DAS

In order to measure the continuous evolution of the variables in the test, the components of the system were instrumented with the appropriate temperature, total pressure, fluid pressure, relative humidity and deformation sensors. Table 5.1 shows the number and type of sensors, the variable measured and the location in the system.

The test has been divided into two zones, one including Heater A (Zone A) and the other with Heater B (Zone B). The sensors in the clay barrier have been grouped into 25 sections, 12 in each lateral zone, and one section AB which coincides with the central vertical plane. The lateral instrumented section is called Ann or Bnn, depending on the zone (A or B) and on the distance from the central vertical plane, where nn is the ordinal number of the placement. Figure 5.2 shows the two zones with the distribution of the different sections.

In addition to the sensors placed inside the clay barrier, other sensors have been installed in the confining structure and in the exterior auxiliary systems, as well as in the hydration and heater control systems.

Table 5.1 Installed instrumentation (ENRESA, 2000).

Variable	**Type of sensor**	**Area**			**Total**
		Bentonite	Confining Structure	Exterior	
Temperature	RTD Pt100	328	20		348
Room temperature	RTD Pt100			1	1
Injection pressure					
manometer	DIGIBAR II			1	1
water pressure	DRUCK 1400PTX		2		2
Mass of hydration tanks	MVD 2510				
Total pressure					50
radial	KULITE BG0234	14			
tangential	KULITE BG0234	14			
axial	KULITE BG0234	22			
Fluid pressure	KULITE HKM375	20			20
RH + Temperature	VAISALA HMP233	40			40
Deformation (Strain gages)	HBM		19		19
PLC values					
temperature	RTD Pt100			18	18
average temperature	calculated			2	2
power	calculated			2	2
DC voltages				2	2
Totals		438	41	26	505

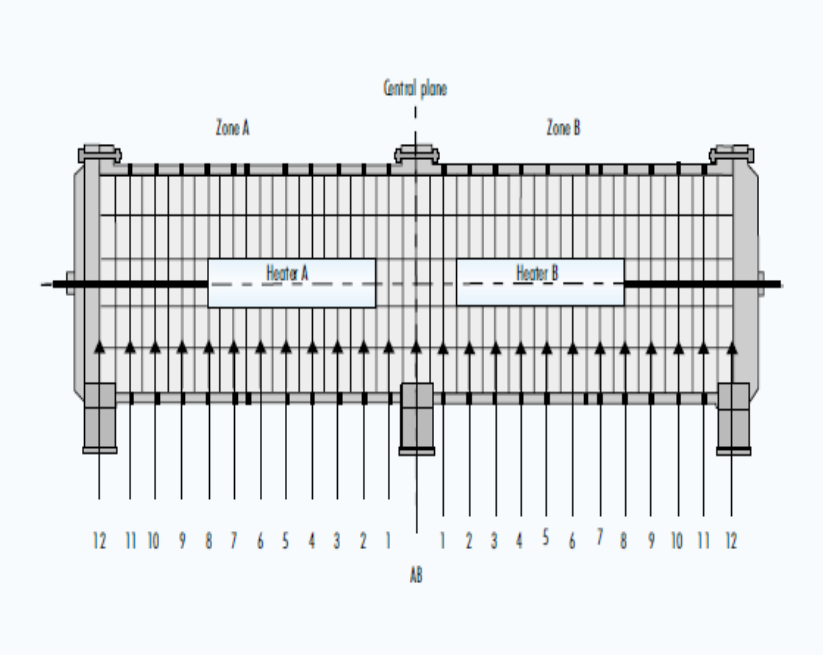

Figure 5.2 Distribution of instrumented sections (ENRESA, 2000).

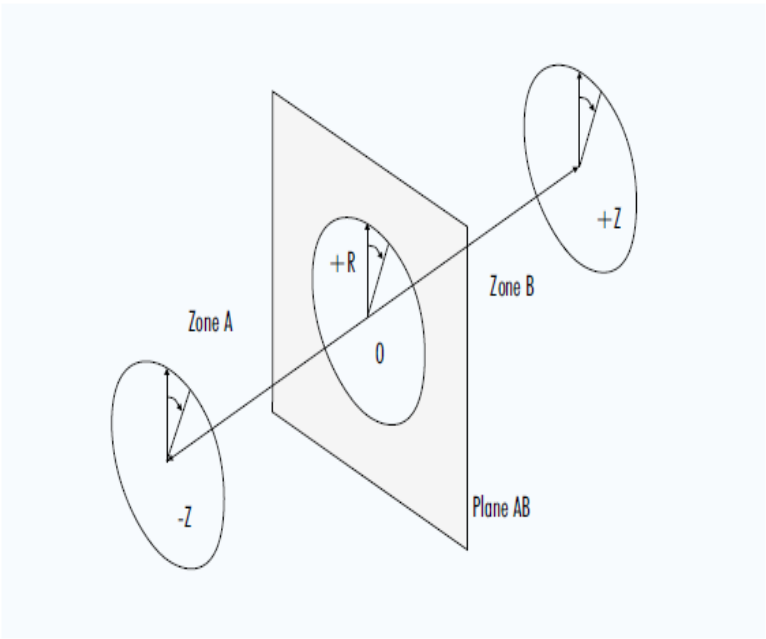

Figure 5.3 Cylindrical coordinate system in the Mock-up test (ENRESA, 2000).

5.1.4.1 Sensor Coding

A cylindrical coordinate system (Figure 5.3) has been selected to describe the distribution of sensors in the instrumented sections. In this coordinate system (R, θ and Z), the origin O is taken at the intersection of the central vertical plane AB with the longitudinal axis of the confining structure (axis Z). The variables follow the rules of the coordinate system: values of R increasing from the Z-axis, values of θ increasing from a reference radius taken at the upper vertical radius of each section and values of Z increasing from the origin to zone B.

The entire sensor coding follows these general rules with a few exceptions. A distinction has been made between four main groups of sensors: in the clay barrier, in the heaters, on the surface of the confining structure and the external sensors and instruments.

5.1.4.1.1 Sensors Within The Clay Barrier

The codification of the sensors within the bentonite is shown below. Each sensor installed is identified by an alphanumerical code as follows:

$$\alpha\alpha\_\beta\beta\ nn\_k\_l$$

αα: Sensor type according to the following keys: T (Temperature), PR (radial total pressure), PT (tangential total pressure), PZ (axial total pressure), H (fluid pressure) and V (Relative Humidity and temperature).

ββ: Zone of installation in the structure according to the following keys: A (zone A), B (zone B) and AB (central vertical plane AB).

nn: Numbering of instrumented section as installed in each zone ββ. The values range from 1 to 12, increasing with the increasing distance from the center plane AB.

k: Numbering of the radial position within the corresponding instrumented section. The values range from 1 to 4, increasing with the radius value. In the distribution of the pressure sensors, the values range from 1 to 3 corresponding to different zones in the backfill: core (1), inner ring (2) and outer ring (3).

l: Numbering of the angular order within the corresponding instrumented section. The values range from 0 to 7, increasing with the increasing angle and taking as origin the upper vertical radius and as positive sense the usual one defined in the cylindrical coordinate system. As a special case, the values range from 1 to 3 in the distribution of pressure sensors and is used only if the rest of the code is identical.

5.1.4.1.2 Temperature Sensors Within The Heater

These sensors are located on the surface of the heater and are distributed in three sections located near the front end cover (sensors numbered 1 to 4), in the control zone (sensors numbered 5 to 8) and in the solid end cover (sensor number 9). The sensors are distributed at 90º in each section, in a strip measuring less than 0.02 m in width. The control level is located in the middle of the heater and provides the average temperature value in order to calculate the power supplied to the heater.

These sensors do not follow the general codification rules and are identify by an alphanumerical code as follows:

C_PT#_α

C_PT: Temperature point on the heater.

#: Numbering of order of installation on the heater, from 1 to 9.

α: Heater, according to the following keys: A for heater installed in zone A and B for heater installed in zone B.

5.1.4.1.3. Temperature Sensors On The Confining Structure

Twenty temperature sensors have been installed on the outer surface of the confining structure at locations associated with the position of the deformation measuring points. These sensors do not follow the general codification rules and are identified by the following alphanumerical code:

T_ α_#

T: Temperature

α: Zone of installation in the confining structure, according to the following keys: A (zone A) and B (zone B).

#: Numbering of the order of installation, from 1 to 10.

5.1.4.1.4. External Sensors And Instruments

This type of sensors includes all the signals that come from external sources like room temperature or water pressure in the inner surface of the structure, from instruments like signals from the hydration system (injection pressure and weight of tanks) and also the calculated values like the injected water volume, average control temperature and power supplied.

5.1.4.2 Data Acquisition System

The Data Acquisition System (DAS) includes all the electronic components, as well as the software necessary to automatically supervise, register and store on a disk the data obtained from the test. The system is capable of acquire, adopt, display and record all the information generated by the installed instrumentation.

5.2 Numerical Results

The experimental results obtained from the mock-up test carried out by CIEMAT, were used to calibrate the models in an effort to explain the behavior of the engineering barrier under non-isothermal conditions at almost full scale. The results consist of temperature, relative humidity, water intake, total pressures and heat power measurements made by the sensors inside the system during the operational stage of the

test that began on February 1997. The experiment is still in operation but the data used for the analysis correspond to a period of almost 16 years (5806 days).

In this section, the following plots show the comparison of the measurements with model predictions of the evolution of the mentioned variables in selected instrumented sections along the system at different radial distance from the heaters. The analysis has been focused on two groups of sections: a group of sections located in the heater zone (sections A4 & B4) and the other located out of the heater zone (sections A10 & B10). This way with two extreme conditions, two patterns of behavior can be studied. Additional results can be found in section A.1 of the appendix. The symmetry of the problem was taking into account by considering one half of the test (one heater). The numerical simulations were performed using the finite element program CODE_BRIGHT and divided into four cases: Operational Base Case (OBC), Threshold Hydraulic Gradient (THG), Thermo-osmosis (THO) and Double Structure (DS).

5.2.1 Initial Conditions

The following conditions correspond to the ones measured before the start of the operational stage of the test. The bentonite barrier was initially unsaturated with an initial degree of saturation of 71.5 %. An initial uniform temperature of 20°C in the system was assumed for the analysis. Regarding the mechanical conditions, a hydrostatic stress of 0.11 MPa has been adopted. This is approximately the same to the weight of the bentonite in the longitudinal axis of the buffer (Sánchez et al., 2012).

5.2.2 Boundary Conditions

The hydraulic boundary conditions are based on the current test conditions. A 0.55 MPa water pressure was applied at the interface between the confining structure and the bentonite to start the hydration process.

The thermal boundary conditions were applied at a radius equal to 0.15 m (position of the heaters) to reproduce the experiment conditions. From day 0 to day 6, a constant power of 250 W per heater was applied. After that, from day 7 to t_{100}, the double of the power per heater (500 W) was applied. Finally, from t_{100} to the end of the test, a constant temperature of 100°C was applied. Here, t_{100} corresponds to the time at which the temperature inside the bentonite reaches 100°C. To simulate the conditions at the external boundary, the following equation was used:

$$j_e = \gamma_e \left(T^0 - T \right) \tag{5.1}$$

where j_e is the heat flow, T^0 is the prescribed temperature (20°C) and γ_e is the radiation coefficient. In this case a coefficient of 5 has been used (Sánchez et al., 2012).

Regarding the mechanical boundary conditions, a stress free condition has been adopted for the outer boundary of the steel confining structure. Since the confining structure has been considered in the analysis, strain and stresses are expected to be computed by the computer program (Sánchez et al., 2012; Sánchez et al., 2010).

5.2.3 Operational Base Case

This section presents the numerical analysis based on the OBC model. This model is the same as the one used during the simulations of the infiltration tests discussed in section 4.2.1. However, in this analysis a 2D axis-symmetric model has been adopted. Tables 5.2, 5.3 and 5.4 show the general, mechanical and hydraulic parameters used in the numerical analysis.

Table 5.2 General parameters used in the OBC case to perform the numerical analysis in the mock-up test.

Parameter	Value	Parameter	Value
ρ_{db}	**1.65**	G_S	**2.72**
ρ_{dg}	**1.77**	e_{total}	**0.648**
ω	**14.00**	φ_{total}	**0.393**

Table 5.3 Mechanical parameters used in the OBC case to perform the numerical analysis in the mock-up test.

Parameter	Value	Parameter	Value
ki0	**0.05**	xlam0	**1.5**
ks0	**0.3**	r	**0.75**
K_min	**0.1**	beta	**0.05**
phimin	**0**	roh	**0.2**
xnu	**0.4**	k	**0.1**

Table 5.3 Continued

Parameter	Value	Parameter	Value
alphass	**0**	pc	**0.1**
alphais	**-0.003**	M	**1.5**
alphasp	**-0.147**	alpha	**0.395**
pref	**0.01**	e0	**0.5881**
alph0	**1.50E-04**	p0ast	**14**
tref	**20**		

Table 5.4 Hydraulic parameters used in the OBC case to perform the numerical analysis in the mock-up test.

Parameter	**Value**	**Parameter**	**Value**
p0d (MPa)	**28**	**psec**	**1100**
sigma0	**0.072**	**lambda2**	**1.1**
lamdad	**0.18**	**Kxx int. perm.**	**1.9E-21**
srl	**0.01**	**Kyy int. perm.**	**1.9E-21**
sls	**1**	**Kzz int. perm.**	**1.9E-21**
p	**0**	**Initial porosity**	**0.399**
d	**0**	**Minimum**	**0.001**
sd	**0**		

The thermal results obtained from the analysis based on the OBC model are shown in the following figures. Figure 5.4 shows the evolution of the power applied by the heaters during the test. It can be seen that the model produced good results when they

are compared with the measurements. However, from about day 2000, the numerical results indicate a slow increment of the heat power. This is mainly due to the progressive hydration of the barrier that produces an increase in thermal conductivity. In addition to the power of the heaters, the values of temperature were computed by the model and compared with the experimental data obtained from different locations along the system. Figures 5.5 and 5.6 present the measurements and model predictions for the evolution of temperature in section 5 and section 11, respectively, at different radii. In general, the model made very good predictions of the measured values. Nevertheless, as we move closer to the heater, small discrepancies can be observed. These differences in the temperature field could be caused by the lower thermal conductivity in the interface between the heater and bentonite.

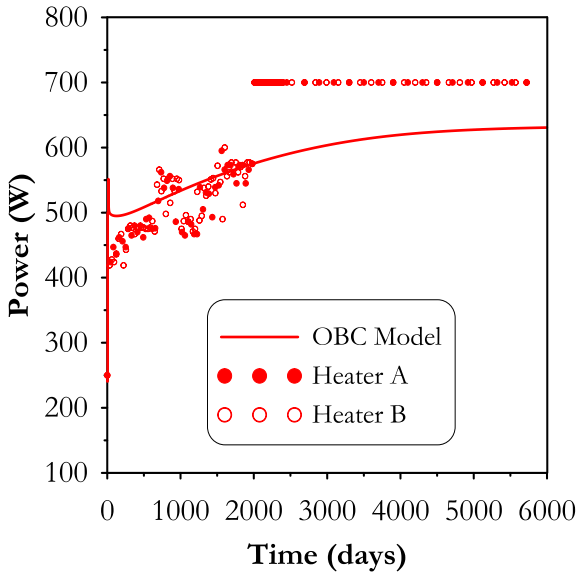

Figure 5.4 Evolution of power supplied by the heaters during the mock-up test. Measurements (scatter points) and OBC model predictions (solid line) up to 6000 days.

In order to study the hydraulic behavior in the bentonite barrier, the measurements of water intake and relative humidity obtained during the test have been compared with the predicted values computed by the OBC model. Figure 5.7 shows the experimental data and model predictions of the evolution of water intake and water intake rate.

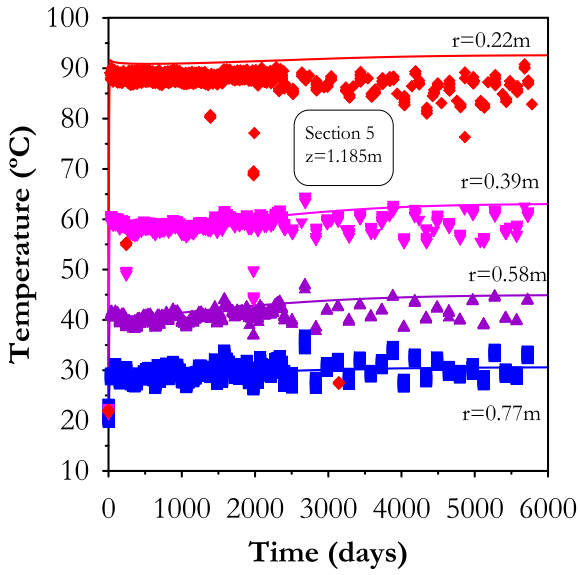

Figure 5.5 Evolution of temperature in sections A5 and B5 during the mock-up test. Measurements (scatter points) and OBC model predictions (solid line) up to 6000 (days).

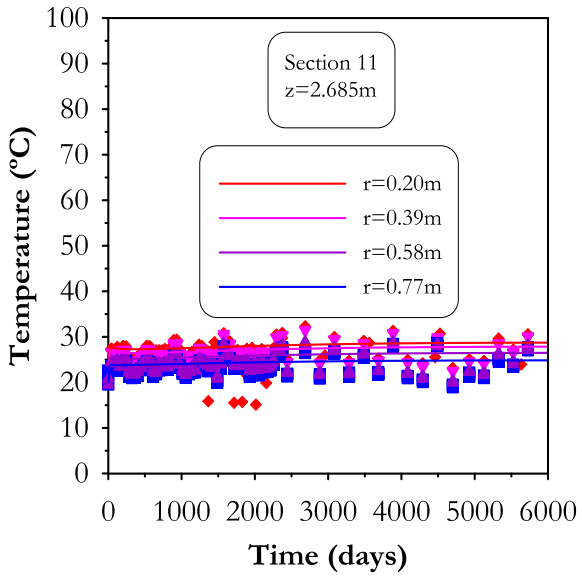

Figure 5.6 Evolution of temperature in sections A11 and B11 during the mock-up test. Measurements (scatter points) and OBC model predictions (solid line) up to 6000 (days).

According to the figure, it can be noted that the model predicts very well the measurements for the first 900 days. After that, it can be seen that the computed values are moving apart from the experimental data, predicting a higher water intake. In addition, it is observed that the model is also predicting a higher rate of hydration. This is clearly observed in the discrepancies between the measured and predicted values of the water intake rate.

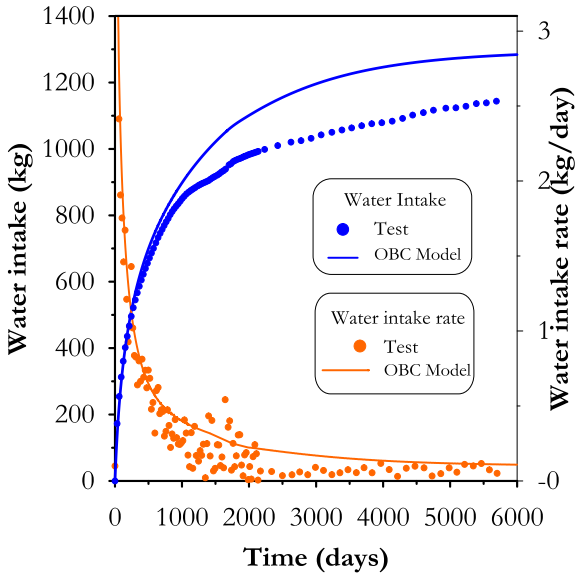

Figure 5.7 Evolution of water intake and water intake rate during the mock-up test. Measurements (scatter points) and OBC model predictions (solid line) up to 6000 (days).

Figures 5.8 and 5.9 show the experimental data and calculated values of relative humidity for section 4 (inside the heater zone) and section 10 (outside the heater zone), respectively. The measurements were taken at different radial distance from the heat source (0.70 m, 0.55 m, 0.37 m and 0.22 m). In general, up to day 900, the model is able to reproduce very well the measured values.

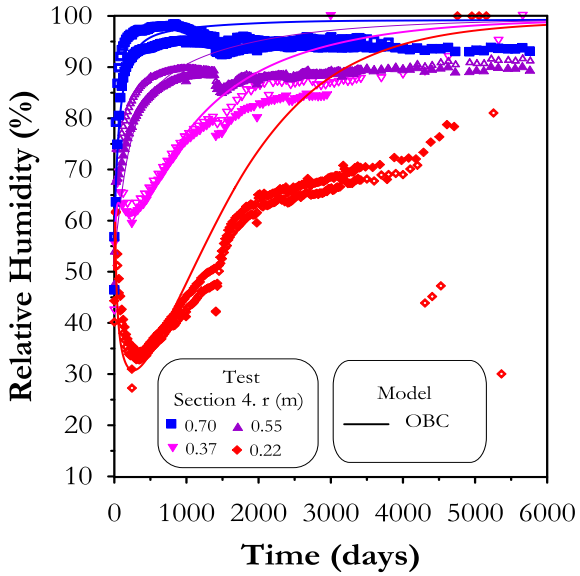

Figure 5.8 Evolution of relative humidity in sections A4 and B4 during the mock-up test. Measurements (scatter points) and OBC model predictions (solid lines) up to 6000 days.

Regarding the results observed in section 4, the locations closer to the hydration source (0.70 m and 0.55 m) experienced an increase in the relative humidity values. This is an indication of a progressive saturation in the bentonite barrier. On the other hand, in locations closer to the heater (0.37 m and 0.22 m), an initial decrease in relative humidity (drying) followed by a slow hydration is observed. This temporary wetting is due to the condensation of the water vapor coming from the area closest to the heater. After the 900 day, some differences between the data and model predictions are observed. In all of the positions, the rate of relative humidity has been overestimated by the model especially in the zones closer to the heater.

The hydraulic behavior in section 10 is not that complex compared to the one observed in section 4. In this section, all the positions experience a steady increase in the values of relative humidity implying a progressive saturation of the barrier. In addition,

there is no evidence of drying in any of the positions. In general, the model captures very well the behavior showed by the measured values at early stages of the test. However, close to the 2000 day, the model overestimates the experimental values.

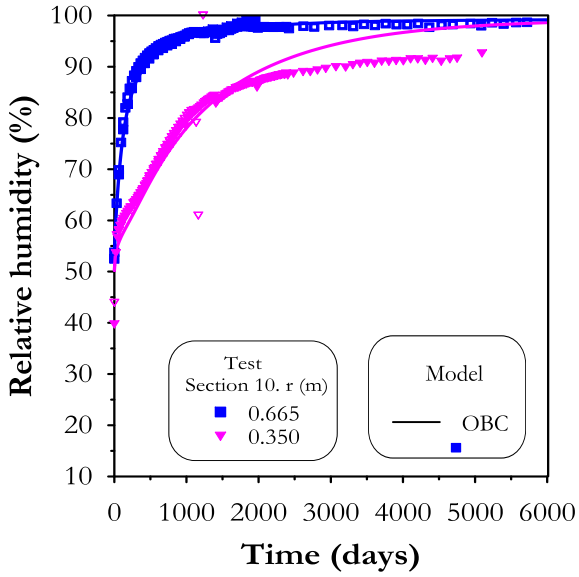

Figure 5.9 Evolution of relative humidity in sections A10 and B10 during the mock-up test. Measurements (scatter points) and OBC model predictions (solid lines) up to 6000 days.

Figures 5.10, 5.11 and 5.12 show the evolution of stresses in selected positions of the barrier during the mock-up test. Three types of stresses were recorded depending on how they were measured: tangential (P_T), longitudinal (P_Z) and radial (P_R). It can be noted that the model predicts quite well the experimental data in sections close to the heater up to day 900. This similar trend was also observed during the analysis of the evolution of the hydraulic variables. After day 900, the mechanical behavior of the bentonite is affected by the change in the hydraulic pattern. As a result, some

discrepancies between the measured and predicted values are observed. This proofs the strong hydro-mechanical coupled phenomena expected from this problem.

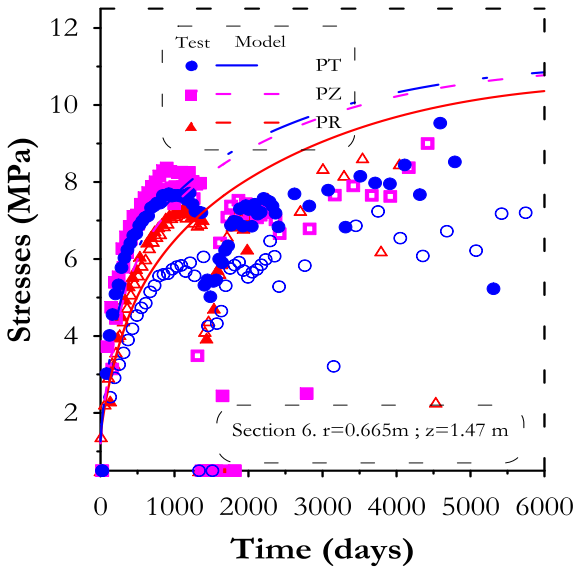

Figure 5.10 Evolution of stresses in sections A6 and B6 during the mock-up test. Measurements (scatter points) and OBC model predictions (solid lines) up to 6000 days.

In addition to the effect of the hydration pattern on the mechanical behavior, an important overheating episode also affected the trend observed in the evolution of stresses especially in sections close to the heater. During this event, the stresses decreased significantly. After this episode, the general trend was recovered but the values are much lower than the ones recorded prior to the overheating. On the other hand, the sections away from the heater were not affected by this event and the model captures satisfactorily the measured values of stresses. In these sections, values of stresses higher than 10 MPa were predicted by the model.

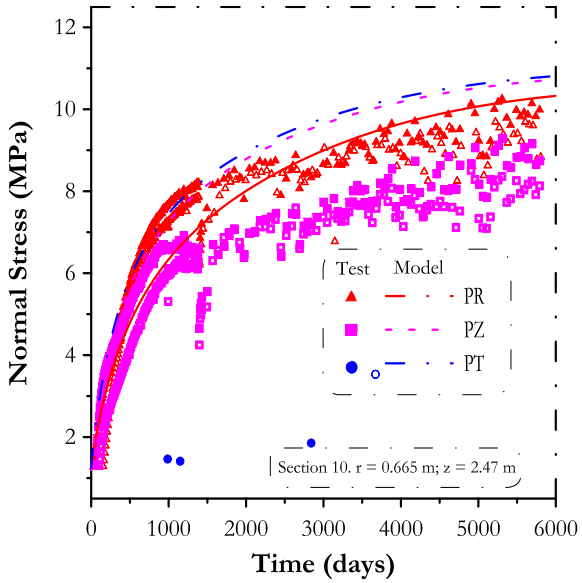

Figure 5.11 Evolution of stresses in sections A10 and B10 during the mock-up test. Measurements (scatter points) and OBC model predictions (solid lines) up to 6000 days.

In general, the OBC model predicts very well the thermal behavior inside the barrier. In addition, the model was able to capture the initial hydration in the bentonite but it overestimates the water intake and relative humidity values afterward. This is a critical issue because the model will underestimate the time required to achieve a fully saturation condition. Finally, the values of stresses are being overestimated in sections close to the heater due to the hydro-mechanical coupling of this problem.

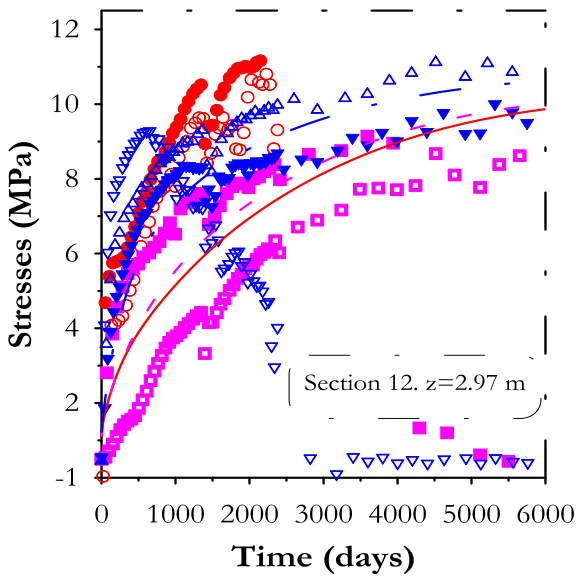

Figure 5.12 Evolution of stresses in sections A12 and B12 during the mock-up test. Measurements (scatter points) and OBC model predictions (solid lines) up to 6000 days.

5.2.4 Threshold Hydraulic Gradient

In order to explain the apparent decay in the hydration of the barrier, other phenomena are included. In this section, the threshold hydraulic (THG) approach is considered in the numerical analysis. This is the same approach used for the simulations performed on the infiltration tests. A 1D axis-symmetrical model has been adopted in the analysis. In addition, two characteristics group of sections have been considered: sections A4 & B4, near the heat source and sections A10 & B10 away from the heater. Tables 5.5, 5.6 and 5.7 show the general, mechanical and hydraulic parameters used in the numerical analysis.

Table 5.5 General parameters used in the THG case to perform the numerical analysis in the mock-up test.

Parameter	Value
ρ_{db}	**1.65**
ρ_{dg}	**1.77**
ω	**14.00**
G_S	**2.72**
e_{total}	**0.648**
φ_{total}	**0.393**

Table 5.6 Mechanical parameters used in the THG case to perform the numerical analysis in the mock-up test.

Parameter	Value	Parameter	Value	Parameter	Value
ki0	**0.05**	alphasp	**-0.147**	**roh**	**0.2**
ks0	**0.3**	pref	**0.01**	**K**	**0.1**
K_min	**0.1**	alph0	**1.50E-04**	**pc**	**0.1**
phimin	**0**	tref	**20**	**M**	**1.50**
xnu	**0.4**	xlam0	**1.5**	**alpha**	**0.395**
alphass	**0**	r	**0.75**	**e0**	**0.5881**
alphais	**-0.003**	beta	**0.05**	**p0***	**14**

Table 5.7 Hydraulic parameters used in the THG case to perform the numerical analysis in the mock-up test.

Parameter	Value	Parameter	Value
p0d (MPa)	**28**	lambda2	**1.1**
sigma0	**0.072**	Kxx int. perm.	**1.9E-21**
lamdad	**0.18**	Kyy int. perm.	**1.9E-21**
srl	**0.01**	Kzz int. perm.	**1.9E-21**
sls	**1**	Initial porosity	**0.399**
p	**0**	Minimum	**0.001**
d	**0**	powthres	**180**
sd	**0**	threshold	**50**
psec	**1100**		

The following figures show the comparison of the predicted results with the experimental measurements of water intake and relative humidity. A 1D version of the OBC model is also introduced in the analysis for comparison.

Figure 5.13 shows the evolution of water intake in the mock-up test, taking into account the phenomenon of the threshold hydraulic gradient. It can be noted the improvement in the numerical results when the THG model is applied. This means that the model is able to slow down the hydration rate in the barrier. Good numerical results are obtained up to 4000 days. After that time, a tendency of the model to reach a steady state is observed, resulting in a small underestimation by the predicted values.

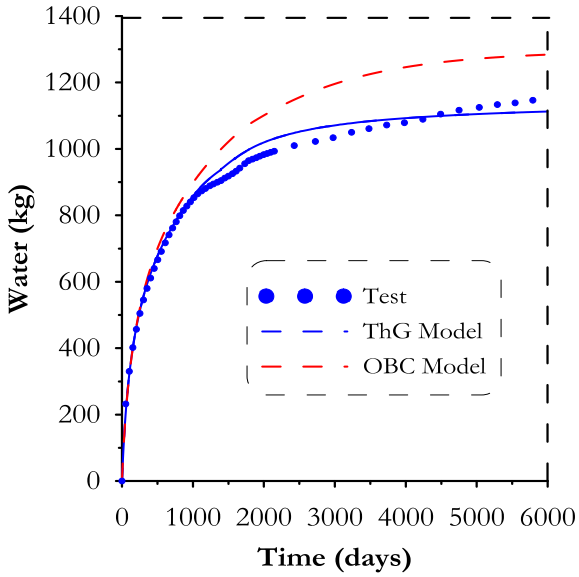

Figure 5.13 Evolution of water intake during the mock-up test. Measurements (scatter points), THG and OBC model predictions up to 6000 (days).

Regarding the results of relative humidity, it is observed that there was also an improvement in the model predictions if we compare them with the ones obtained from the OBC model. In sections close to the heater (Figure 5.14), the model is able to capture the hydraulic behavior observed in this area especially in the sensors near the heat source (0.22 m and 0.37 m). The model predicts very well the initial drying, the overheating episode and also the subsequent hydration pattern. However, in the positions where the sensors are away from the heating zone (0.55 m and 0.70 m), the model still overestimates the measured values. In sections A10 & B10, where there is no influence of the heater, the model predicts very well the trend showed by the experimental data as presented by Figure 5.15.

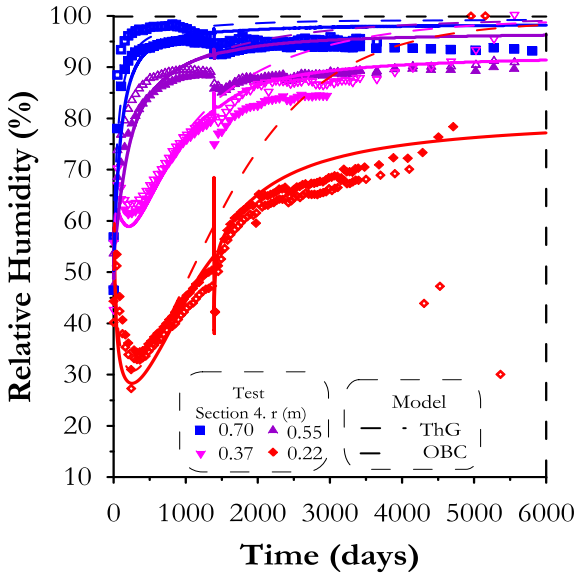

Figure 5.14 Evolution of relative humidity in sections A4 and B4 during the mock-up test. Measurements (scatter points), THG and OBC model predictions up to 6000 days.

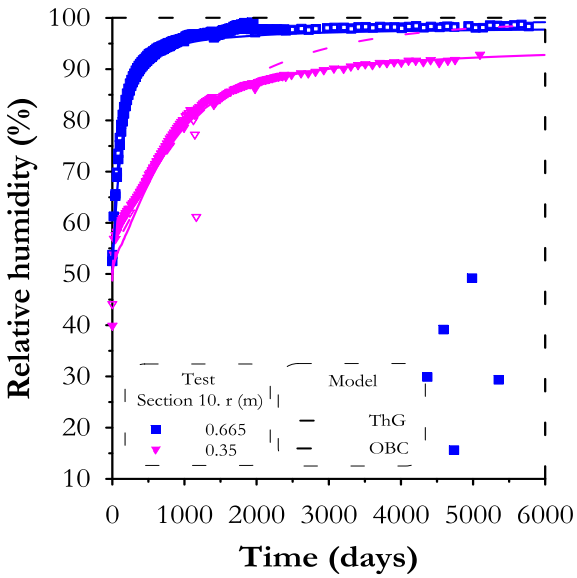

Figure 5.15 Evolution of relative humidity in sections A10 and B10 during the mock-up test. Measurements (scatter points), THG and OBC model predictions up to 6000 days.

In summary, the inclusion of the threshold hydraulic gradient (THG) model in the original formulation improved the predictions obtained in the numerical analysis. The model was able to reproduce very well the evolution of the main hydraulic variables due to its capability to slow down the hydration rate in the bentonite barrier.

5.2.5 Thermo-Osmosis

In this part of the analysis, the thermo-osmosis effect is introduced to the original formulation. This is the same phenomenon considered in the numerical simulations for the infiltration tests. It is important to recall that the thermo-osmosis is related to the movement of water as liquid in the presence of thermal gradients. At advanced stages of this test, when the hydraulic gradient becomes small, the thermal conditions start to affect the movement of water inside the barrier, controlled by the thermo-osmosis effect. Tables 5.8, 5.9, and 5.10 show the general, mechanical and hydraulic parameters respectively, used in the numerical analysis.

Table 5.8 General parameters used in the THO case to perform the numerical analysis in the mock-up test.

Parameter	Value
ρ_{db}	**1.65**
ρ_{dg}	**1.77**
ω	**14.00**

Table 5.8 Continued

Parameter	Value
G_S	**2.72**
e_{total}	**0.648**
φ_{total}	**0.393**

Table 5.9 Mechanical parameters used in the THO case to perform the numerical analysis in the mock-up test.

Parameter	Value	Parameter	Value	Parameter	Value
ki0	**0.05**	alphasp	**-0.147**	**roh**	**0.2**
ks0	**0.3**	pref	**0.01**	**K**	**0.1**
K_min	**0.1**	alph0	**1.50E-04**	**pc**	**0.1**
phimin	**0**	tref	**20**	**M**	**1.50**
xnu	**0.4**	xlam0	**1.5**	**alpha**	**0.395**
alphass	**0**	r	**0.75**	**e0**	**0.5881**
alphais	**-0.003**	beta	**0.05**	**p0***	**14**

Table 5.10 Hydraulic parameters used in the THO case to perform the numerical analysis in the mock-up test.

Parameter	Value	Parameter	Value
p0d (MPa)	**28**	lambda2	**1.1**
sigma0	**0.072**	Kxx int. perm.	**1.9E-21**

Table 5.10 Continued

Parameter	Value	Parameter	Value
lamdad	**0.18**	Kyy int. perm.	**1.9E-21**
srl	**0.01**	Kzz int. perm.	**1.9E-21**
sls	**1**	Initial porosity	**0.399**
p	**0**	Minimum	**0.001**
d	**0**	KHT	**2.73E-13**
sd	**0**		
psec	**1100**		

The following figures show the evolution of water intake and relative humidity during the mock-up test. The solid lines correspond to model predictions considering the thermo-osmosis (THO) effect and the dash lines correspond to the results obtained from the Operational Base Case (OBC). In this way, the improvements in the model predictions can be observed.

Regarding the results of the water intake (Figure 5.16), it can be seen that the inclusion of the thermo-osmosis model had an effect on the numerical results. In general, there was a reduction in the rate of water intake and the computed values became closer to the measured ones. However, after the 1000 day, there was an overestimation of the observed values.

Figure 5.17 shows the results of relative humidity in sections A4 & B4 up to 6000 days. It can be noted the overall improvement on the numerical results (especially

in the positions close to the heater) when the THO model is considered in the analysis. The model is able to capture very well the pattern showed by the observations up to 2000 days. After that time, the model predictions start to move apart from the measurements, leading to an overestimation of the experimental data. This means that in fact, in addition to the thermo-osmosis effect, there is some other phenomenon that is inducing the slow hydration rate observed in the barrier. The results in Figure 5.18 for sections A10 & B10 show no change respect to the OBC model since this part of the system is not affected by the heater and therefore the thermo-osmosis has no effect.

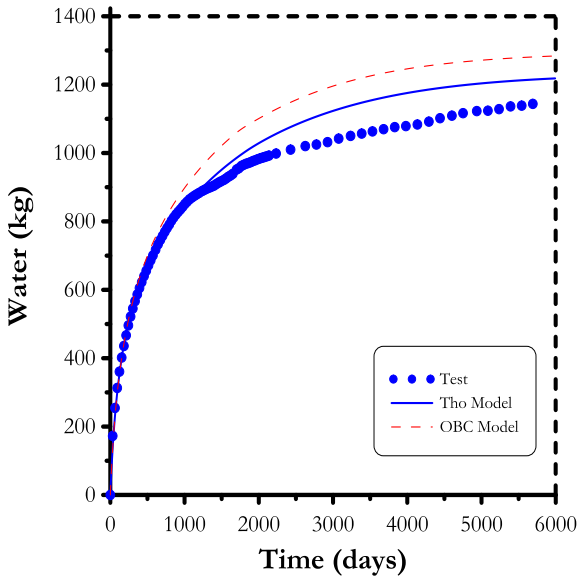

Figure 5.16 Evolution of water intake during the mock-up test. Measurements (scatter points), THO and OBC model predictions up to 6000 days.

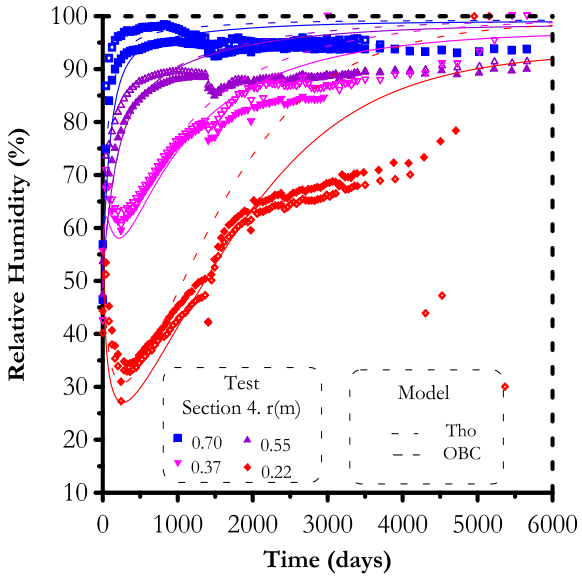

Figure 5.17 Evolution of relative humidity in sections A4 and B4 during the mock-up test. Measurements (scatter points), THO and OBC model predictions up to 6000 days.

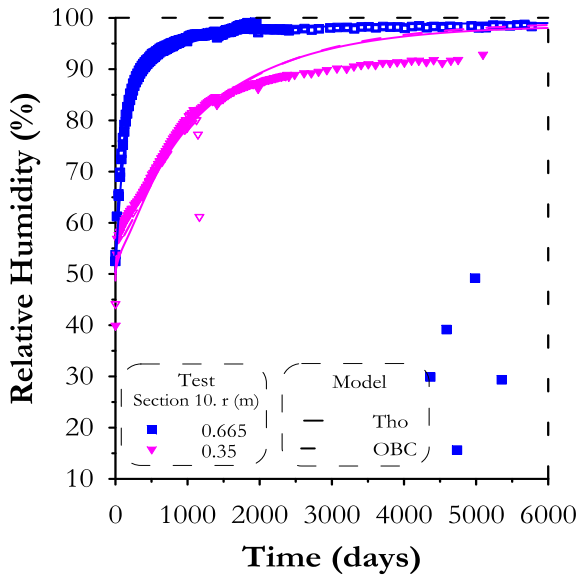

Figure 5.18 Evolution of relative humidity in sections A10 and B10 during the mock-up test. Measurements (scatter points), THO and OBC model predictions up to 6000 days.

In summary, the addition of the thermo-osmosis effect to the original formulation contributed to the improvement of the model predictions by slowing the hydration rate inside the barrier. This results in good agreement between observations and computed values especially in zones near the heat source. Nevertheless, the model overestimates the values at advanced stages of the test (after 2000 days). This suggests that there are other phenomena that slow down the hydration inside the bentonite.

In the following section, the double structure model studied in section 3.4.2, is introduced to the analysis to be able to explain the complex hydraulic behavior of the bentonite barrier by considering changes in the material fabric.

5.2.6 Double Structure

In the following section, the double structure model has been used in the analysis to predict the main THM variables measured during the mock-up test. In this analysis, a 1D axis-symmetric model has been adopted to study two groups of sections: sections A4 & B4, located inside the heater zone and sections A10 & B10, located outside the heater zone. It is important to recall that this model considers the changes in the fabric of the material by identifying two dominant levels of pore sizes that exist in compacted bentonite. It also distinguished the behavior of the two structural levels (microstructure and macrostructure) and the interaction between them.

The following figures show the evolution of temperature, water intake and relative humidity measured during the mock-up experiment with the corresponding

model predictions. Figure 5.19 shows the evolution of temperature in sections A5 & B5 for a period of 6000 days. It can be observed how well the model fits the measurements in all the positions within the section. The range of values goes from 32 °C in the position close to the external part of the system (r = 0.77 m) to 85 °C near the heater (r = 0.22 m).

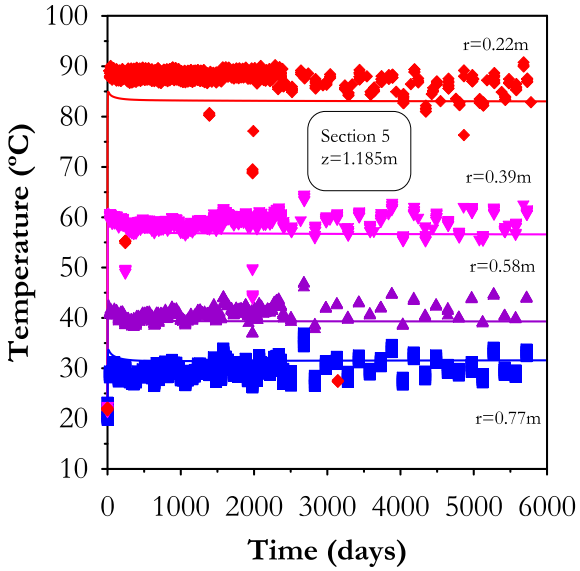

Figure 5.19 Evolution of temperature in sections A5 and B5 during the mock-up test. Measurements (scatter points) and DS model predictions up to 6000 days.

The hydraulic results obtained from the simulations are shown in the following figures. Concerning the evolution of water intake presented in Figure 5.20, the model predicts satisfactorily the trend observed by the measured values up to the first 3500 days. After this time, some discrepancies are observed between the observations and model predictions. However, a notable improvement was achieved in the numerical results when we compare them with the ones obtained by the OBC model.

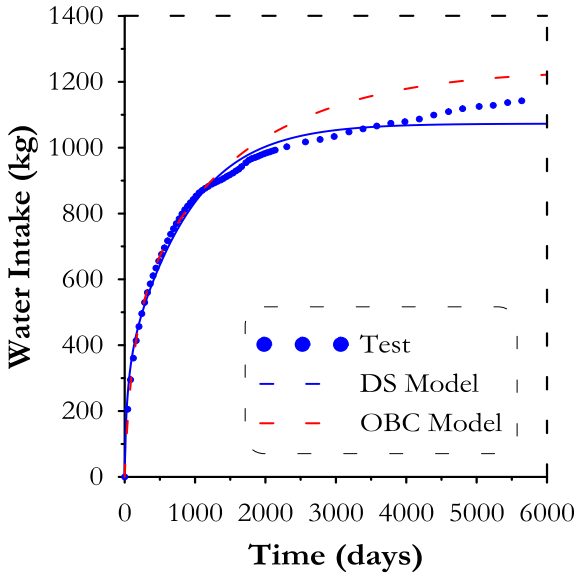

Figure 5.20 Evolution of water intake during the mock-up test. Measurements (scatter points), DS and OBC model predictions up to 6000 days.

The results of relative humidity for sections A4 & B4 are presented in figure 5.21. According to the figure, it can be noted the improvement in the numerical results compared to the ones obtained with the OBC model, especially in the zones close to the heater (r = 0.22 m and r = 0.37 m). The model was able to slow down the hydration rate, resulting in a better agreement with the measured values. Another important observation is that after 6000 days, the bentonite will still be unsaturated with relative humidity values around 66 %. On the other hand, regarding the numerical results for sections A10 & B10 (sections located outside the heater zone), there is not a significant difference between the two model predictions as figure 5.22 shows.

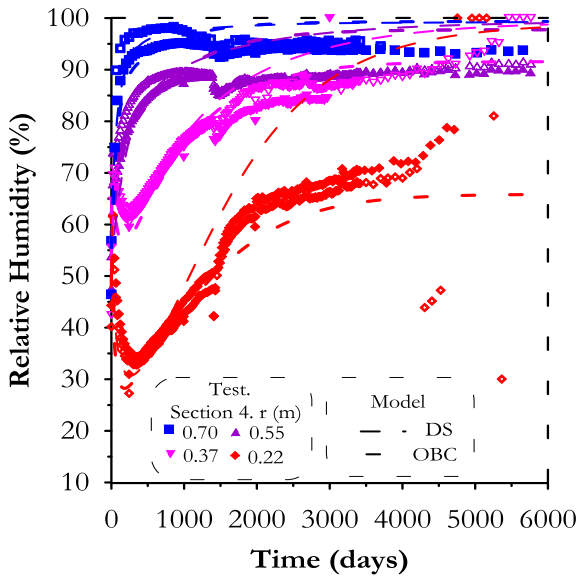

Figure 5.21 Evolution of relative humidity in sections A4 and B4 during the mock-up test. Measurements (scatter points), DS and OBC model predictions up to 6000 days.

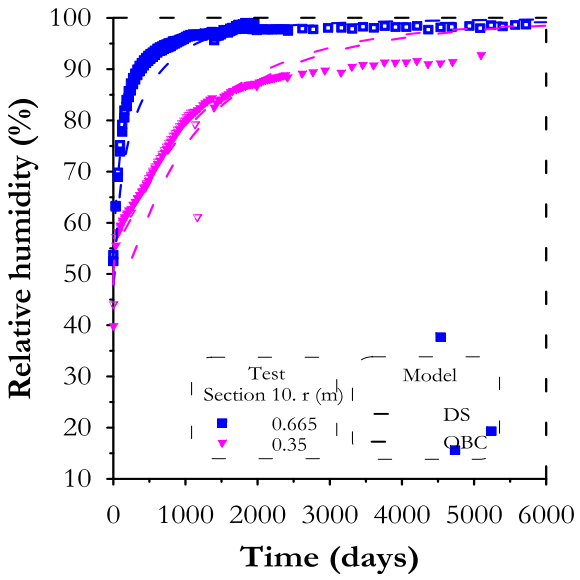

Figure 5.22 Evolution of relative humidity in sections A10 and B10 during the mock-up test. Measurements (scatter points), DS and OBC model predictions up to 6000 days.

In order to find a way to improve the predictions obtained from the double structure model, the parameters in the retention curve of the bentonite were changed. The new double structure model (DS-new) has the retention curve parameters used in the numerical analysis for the infiltration tests. Tables 5.11, 5.12 and 5.13 show the general, mechanical and hydraulic parameters respectively, considered in this new model.

Table 5.11 General parameters for the DS-new model.

Parameter	Value	Parameter	Value
ρ_{db}	**1.65**	$\mathbf{e_{micro}}$	**0.450**
ρ_{dg}	**1.77**	$\mathbf{e_{macro}}$	**0.198**
ω	**14.00**	$\boldsymbol{\varphi}_{\mathbf{micro}}$	**0.273**
G_S	**2.72**	$\boldsymbol{\varphi}_{\mathbf{macro}}$	**0.120**
e_{total}	**0.648**	$\boldsymbol{\varphi}_{\mathbf{total}}$	**0.393**

Table 5.12 Mechanical parameters for the DS-new model.

Parameter	Value	Parameter	Value
ki0	**0.005**	xlam0	**0.08**
ks0	**0.001**	r	**0.90**
K_min	**0.1**	beta	**0.2**
phimin	**0**	roh	**0.2**
xnu	**0.499**	k	**0.1**
alphass	**0**	pc	**0.5**
alphais	**0**	M	**1.0**

Table 5.12 Continued

Parameter	Value	Parameter	Value
alphasp	**0**	alpha	**0.53**
pref	**0.01**	e0	**0.20**
alph0	**1.00E-05**	p0ast	**5.4**
tref	**20**		

Table 5.13 Hydraulic parameters for the DS-new model.

Parameter	Value	Parameter	Value
p0d (MPa)	**28**	**psec**	**1100**
sigma0	**0.072**	**lambda2**	**1.1**
lamdad	**0.18**	**Kxx int. perm.**	**3.0E-21**
srl	**0.01**	**Kyy int. perm.**	**3.0E-21**
sls	**1**	**Kzz int. perm.**	**3.0E-21**
p	**0**	**Initial porosity**	**0.12**
d	**0**	**Minimum**	**0.001**
sd	**0**	**b**	**12**

The following figures show the numerical results of relative humidity obtained with the DS-new model. Figure 5.23 presents the results of relative humidity for sections A3 & B3, A4 & B4, A6 & B6, A7 & B7 and AB corresponding to a radius of 0.70 m

from the heater. Figure 5.24 shows the long term evolution of relative humidity for the same position up to 10950 days (30 years).

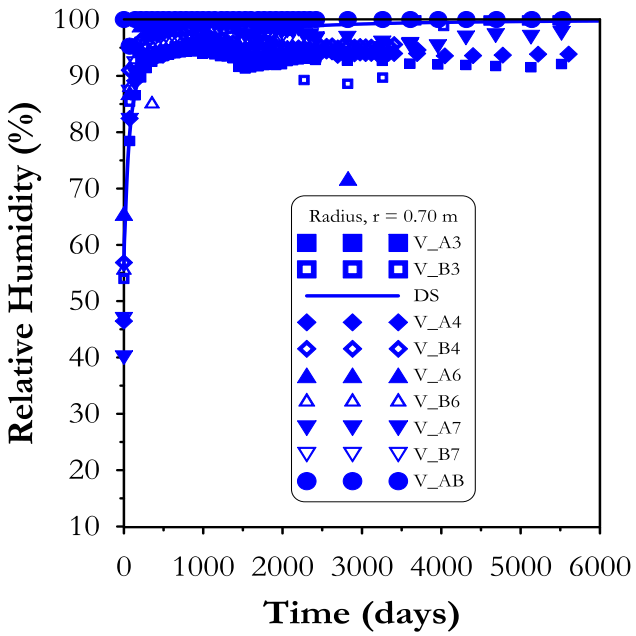

Figure 5.23 Evolution of relative humidity for a radius, r = 0.70 m. Measurements (scatter points) and DS-new model prediction (solid line) up to 6000 days.

Figure 5.25 shows the results of relative humidity for sections A3 & B3, A4 & B4, A6 & B6, A7 & B7 and AB corresponding to a radius of 0.55 m from the heater. Figure 5.26 presents the long term evolution of relative humidity for the same position up to 10950 days (30 years).

The results corresponding to a radius of 0.37 m from the heater are shown in Figure 5.27. Figure 5.28 shows the long term evolution of relative humidity for the same position up to 10950 days (30 years).

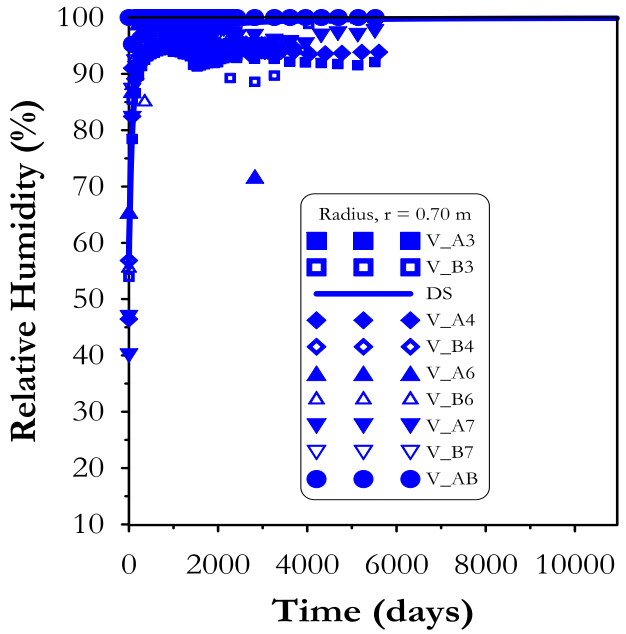

Figure 5.24 Evolution of relative humidity for a radius, r = 0.70 m. Measurements (scatter points) and DS-new model prediction (solid line) up to 10950 days.

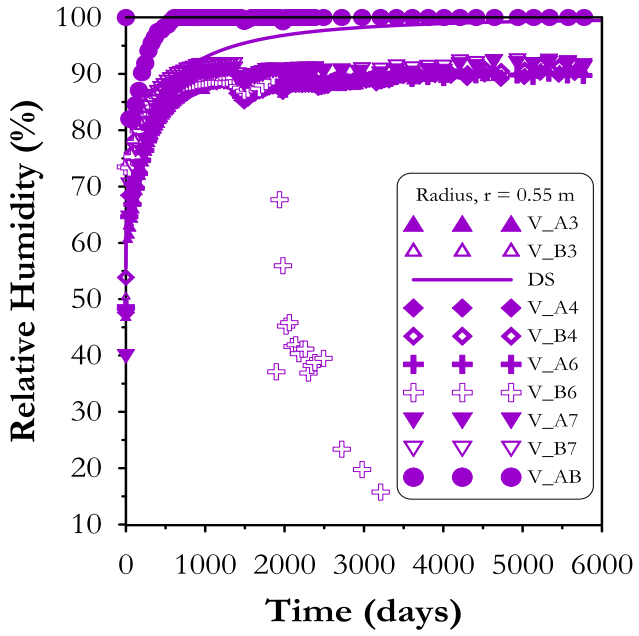

Figure 5.25 Evolution of relative humidity for a radius, r = 0.55 m. Measurements (scatter points) and DS-new model prediction (solid line) up to 6000 days.

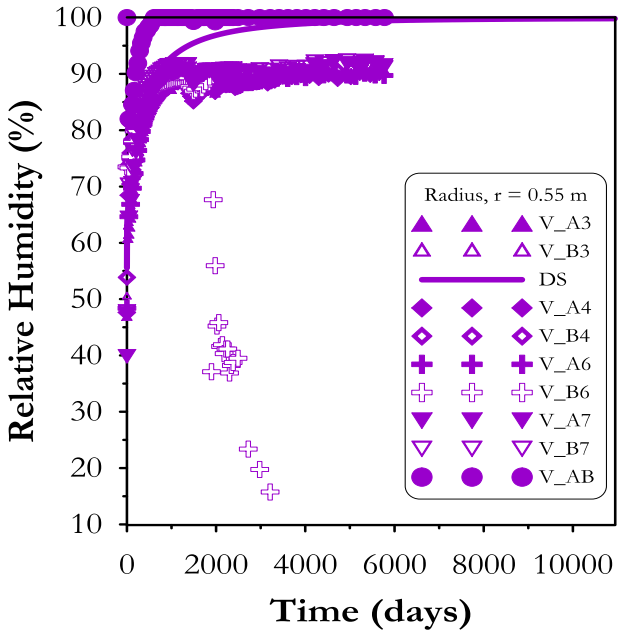

Figure 5.26 Evolution of relative humidity for a radius, r = 0.55 m. Measurements (scatter points) and DS-new model prediction (solid line) up to 10950 days.

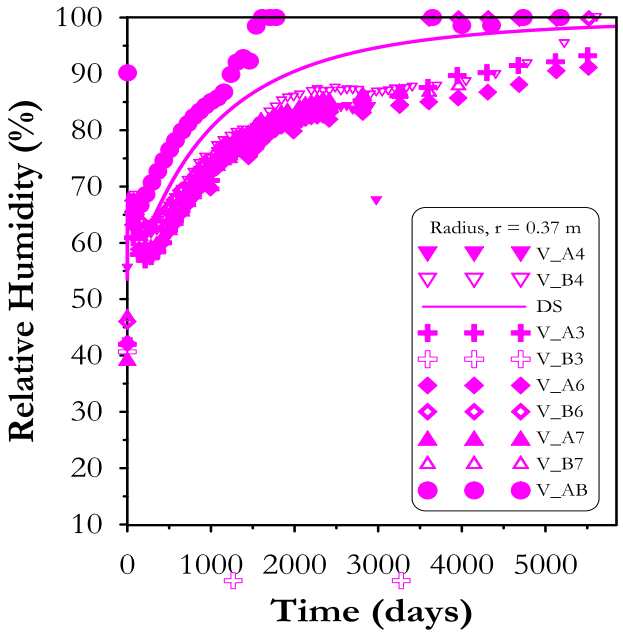

Figure 5.27 Evolution of relative humidity for a radius, r = 0.37 m. Measurements (scatter points) and DS-new model prediction (solid line) up to 6000 days.

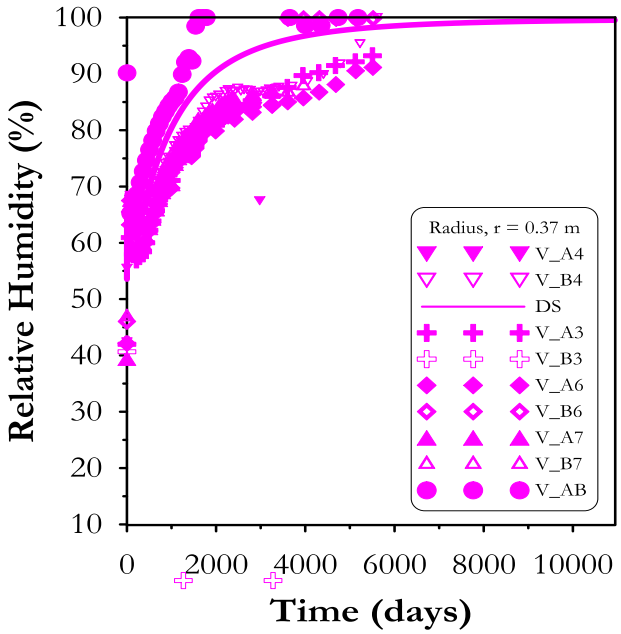

Figure 5.28 Evolution of relative humidity for a radius, r = 0.37 m. Measurements (scatter points) and DS-new model prediction (solid line) up to 10950 days.

Figure 5.29 shows the results of relative humidity for sections A3 & B3, A4 & B4, A6 & B6, A7 & B7 and AB corresponding to a radius of 0.22 m from the heater. Figure 5.30 presents the long term evolution of relative humidity for the same position up to 10950 days (30 years).

In summary, the DS-new (DS-new) model predicted quite well the values of relative humidity at all radii. The change in the hydraulic parameters, especially the ones related to the retention curve allowed to achieve more accurate results.

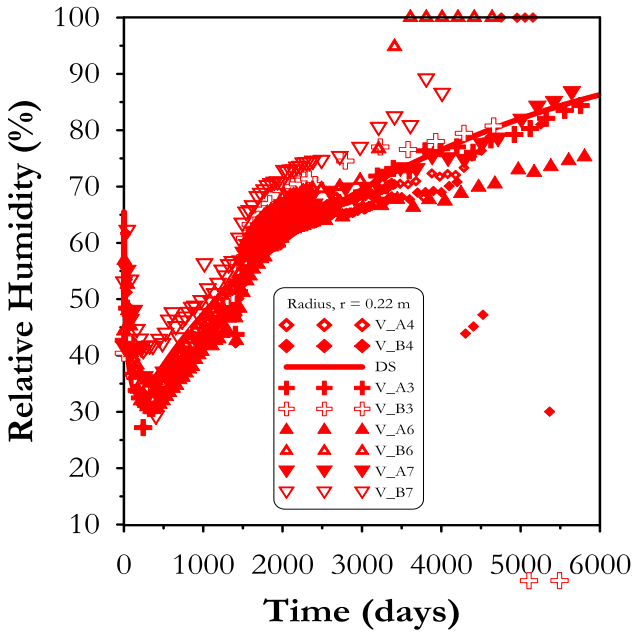

Figure 5.29 Evolution of relative humidity for a radius, r = 0.22 m. Measurements (scatter points) and DS-new model prediction (solid line) up to 6000 days.

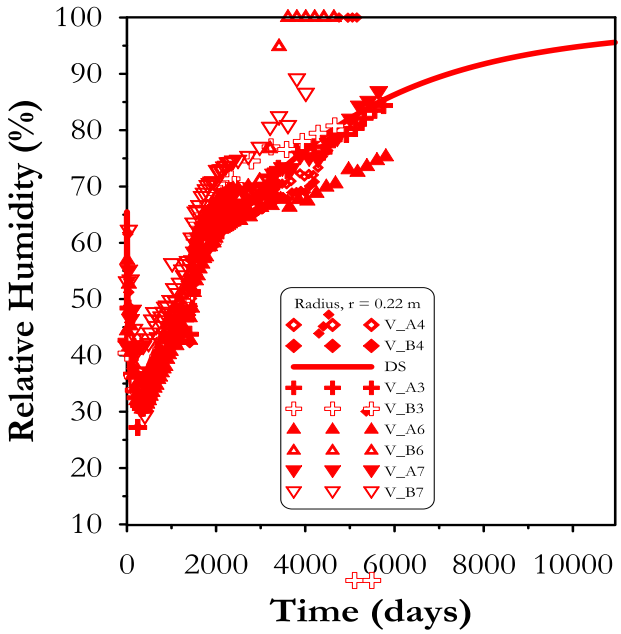

Figure 5.30 Evolution of relative humidity for a radius, r = 0.22 m. Measurements (scatter points) and DS-new model prediction (solid line) up to 10950 days.

6. THERMO-HYDRO-MECHANICAL EVOLUTION OF AN IN SITU SYNTHETIC CASE

In addition to the presented numerical analysis performed on the small scale infiltration tests and on the almost full scale mock-up experiment, it is important to carry out a similar study on a full scale natural environment. In this way, the numerical simulations are based on in-situ measurements that can be more representative of the conditions observed in the setting under study. The study presented in this section also involves very long term predictions (up to 1000 years). The analyses below were performed in the context of the PEBS project founded by the European Commission.

This section presents the Spanish nuclear disposal system in granitic rock with a complete description of the main safety functions of each component. The analysis presented in this section has been performed based on the information obtained from the Grimsel experiment and the R&D program on bentonite material (ENRESA, 2000). The simulations were carried out with the OBC and thermo-osmosis models through the finite element computer program CODE_BRIGHT up to 1000 years to determine the evolution of the main THM variables in different positions along the system. It is important to mention that the results presented should be considered as an exercise due to the lack of experimental data available to calibrate the model. However, these results can be used as hypothesis values in a future in-situ test with similar conditions.

6.1 Spanish Repository Concept

The Spanish repository concept is based on the disposal of spent fuel in carbon steel canisters in horizontal disposal drifts. The repository can be accessed by three shafts and a ramp that lead to the central underground area where the main drafts are located. The access to the canisters is achieved by the main drifts that run orthogonal to the disposal drifts. Figure 6.1 shows a schematic representation of the underground facilities.

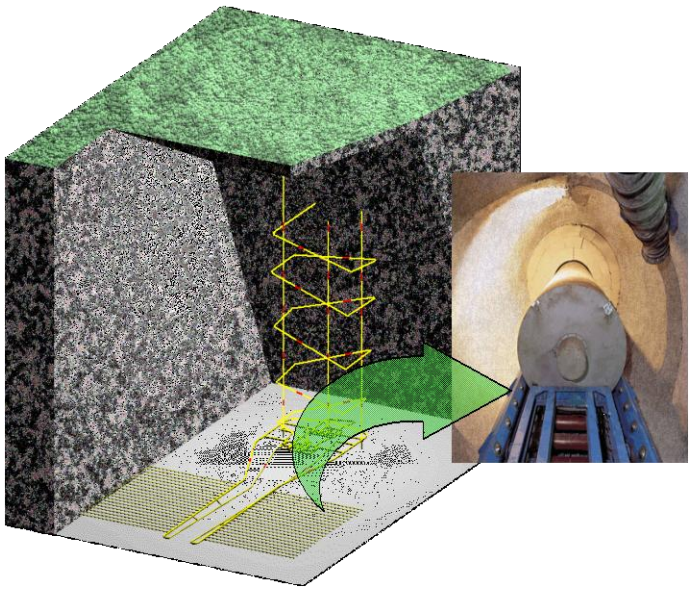

Figure 6.1 Underground facilities based on the Spanish repository concept. (ENRESA, 2000).

The canisters measure 4.54 m in length and 0.90 m in diameter with a wall thickness of 0.10 m and 0.12 m at the ends as Figure 6.2 and 6.3 showed. The canisters are capable to support the pressures to which they are subjected and provide a

containment period of 1000 years. The fuel elements are temporary stored inside the canisters for their thermal power to decay to a level at which they can be disposed. Each canister contains 4 PWR or 12 BWR fuel elements with a total power of 1200 W.

The canisters are placed inside cylindrical disposal cells constructed with blocks of compacted bentonite with a dry density of 1.7 g/cm^3 and a degree of saturation of 66 %. The disposal drifts of 500 m in length and 2.4 m in diameter are located at a depth of 500 m in the granite formation. A separation of 2 m has been established between heaters and 35 m between disposal cells due thermal constraints. The idea is to not exceed a temperature of 100°C in the bentonite.

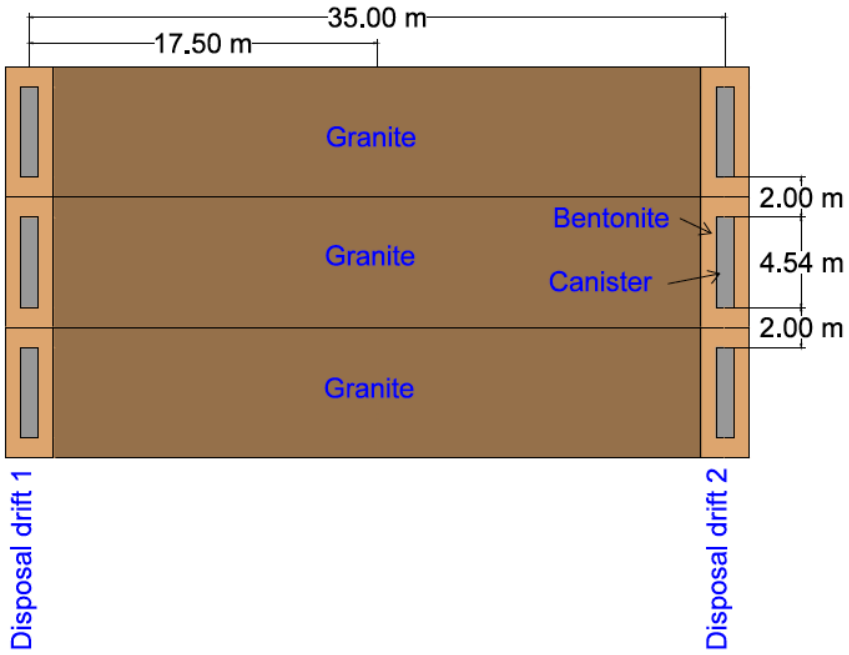

Figure 6.2 Top view of disposal drifts in the repository system.

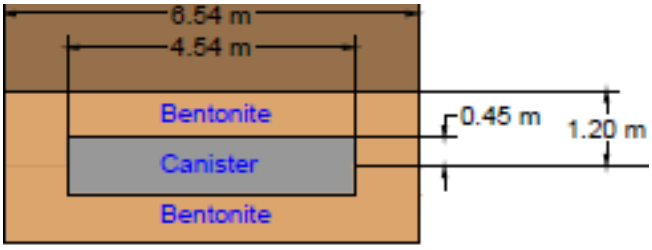

Figure 6.3 Individual disposal cell.

6.1.1 Safety Functions

The two basic safety functions of a repository system are the containment and isolation. The containment consists in avoiding the transport and release of the hazardous materials disposed in the repository. This function is accomplished by a physical barrier which cannot be crossed by the contaminants. This is called absolute containment and is provided by the canister wall. Another type of containment is the retention of contaminants which hinders their transport, reducing fluxes and release rates. This form of containment is achieved by the bentonite barrier. On the other hand, isolation consists in the protection of the components of the repository against environmental conditions that may affect their performance. This is associated with providing suitable boundary conditions to the inner barriers by enhancing their longevity. The isolation is provided by the host rock that protects the engineered barriers against thermal, hydraulic, mechanical and biological conditions in the vicinity of the system.

The bentonite buffer is required to maintain a variety of safety functions which can only be achieved once the bentonite saturates and swells. This expansion in the buffer permits to close the construction gaps between the bentonite blocks and the drift wall or the canister wall. In the outer parts of the drift, this function can be fulfilled in the first weeks or months once the groundwater made contact with the bentonite blocks. However, the main concern is if the buffer can preserve its properties during the resaturation.

In order to meet with the safety criteria for the repository, the buffer material is required to achieve the following long term safety functions:

- Isolate the waste from the geosphere by limiting the advective transport of corroding agents to the canister.
- Isolate the canister from shear displacements in the disposal drift walls.
- Avoid excessive swelling pressures that may contributed to total pressures that the canister cannot support.
- Avoid excessive temperatures (higher than 100°C) that result in chemical alterations of the bentonite.

6.2 Numerical Results

The main goal of the numerical analysis is to determine the evolution of the bentonite buffer in terms of its thermal, hydraulic and mechanical behavior under natural

repository conditions for a period of 1000 years. All simulations were carried out with the finite element program CODE_BRIGHT based on the OBC and thermo-osmosis models to calculate the evolution of temperature, liquid degree of saturation, liquid pressure and stresses inside the bentonite buffer. The problem was approached using a 2D axis-symmetric section of an individual disposal cell that contains the host rock (granite) and the buffer (bentonite). In order to simplify the problem, the steel canister has not been considered and the heat emitting by this component has been incorporated in the analysis by a thermal boundary condition. Due to symmetry, only one half of the problem is analyzed with a mesh of 936 quadrilateral elements as Figure 6.5 shows. Figure 6.4 presents the geometry of the problem.

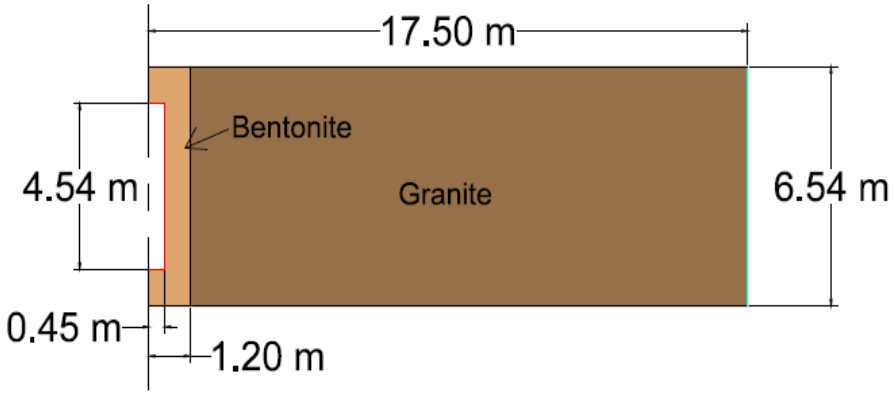

Figure 6.4 Dimensions of the individual disposal cell.

Figure 6.5 Model mesh.

6.2.1 Initial Conditions

The bentonite buffer was initially unsaturated with degree of saturation of 66 %, a suction of around 44 MPa (liquid pressure of -43.9 MPa) and initial porosity of 41 %. On the other hand, the granite has an initial liquid pressure of 0.7 MPa and a porosity of 1 %. Initial isothermal conditions were assumed and a temperature of 30.5 °C was adopted for the entire domain. As for the mechanical conditions, initial stresses of 0.2 MPa and 28 MPa were considered for the bentonite and granitic rock, respectively.

6.2.2 Boundary Conditions

Regarding the hydraulic boundary conditions, a liquid pressure of 0.7 MPa was applied at a distance of 17.50 m from the center of the canister (blue line in figure 6.4) at a temperature of 30.5 °C for a period of 30 days to simulate the initial groundwater flow from the granitic rock. After 30 days, the hydration continues but now a thermal gradient

is applied at the contact between the canister and the bentonite (red lines in figure 6.4) by increasing the temperature to 100 °C. During the rest of the simulation, the temperature remained at 100 °C. As for the mechanical boundary conditions, the entire domain has been fixed to perform the analysis under constant volume conditions.

6.2.3 Operational Base Case

Tables 6.1, 6.2 and 6.3 present the main mechanical, hydraulic and thermal parameters respectively, for the bentonite. Tables 6.4, 6.5 and 6.6 show the mechanical, hydraulic and thermal parameters respectively, for the granitic rock considered in the numerical analysis. Additional results can be found in section A.2 of the appendix.

Table 6.1 Mechanical parameters used for the bentonite in the OBC case to perform the numerical analysis in the buffer exercise.

Parameter	Value	Parameter	Value
ki0	**0.05**	xlam0	**1.5**
ks0	**0.25**	r	**0.75**
K_min	**0.1**	beta	**0.05**
phimin	**0**	roh	**0.2**
xnu	**0.4**	k	**0.1**

Table 6.1 Continued

Parameter	Value	Parameter	Value
alphass	**0**	pc	**0.1**
alphais	**-0.003**	M	**1.5**
alphasp	**-0.1609**	alpha	**0.395**
pref	**0.01**	e0	**0.5881**
alph0	**1.50E-04**	p0ast	**50**
tref	**20**		

Table 6.2 Hydraulic parameters used for the bentonite in the OBC case to perform the numerical analysis in the buffer exercise.

Parameter	**Value**
p0d (MPa)	**30**
sigma0	**0.072**
lamdad	**0.39**
srl	**0**
sls	**1**
p	**0**
d	**0**
sd	**0**

Table 6.2 Continued

Parameter	Value
Kxx int. perm.	**6.00E-21**
Kyy int. perm.	**6.00E-21**
Kzz int. perm.	**6.00E-21**
Initial porosity	**0.399**
Minimum	**0.001**

Table 6.3 Thermal parameters used for the bentonite in the OBC case to perform the numerical analysis in the buffer exercise.

Parameter	**Value**
λ_{dry}	**0.47**
λ_{wet}	**1.15**

Table 6.4 Mechanical parameters used for the granitic rock in the OBC case to perform the numerical analysis in the buffer exercise.

Parameter	**Value**
K_bulk_p	**29166.70**
k_bulk_s	**1.0E+09**
xnu	**0.3**
alpha_T	**23.4E-06**

Table 6.4 Continued

Parameter	Value
Ps0	**1.0E+05**
pc	**1.0**
M	**1.0**
e0	**0.5**
p0ast	**1.0E+05**

Table 6.5 Hydraulic parameters used for the granitic rock in the OBC case to perform the numerical analysis in the buffer exercise.

Parameter	**Value**
p0d (MPa)	**2.1**
sigma0	**0.072**
lamdad	**0.70**
srl	**0.01**
sls	**1**
p	**0**
d	**0**
sd	**0**
Kxx int. perm.	**8.00E-18**
Kyy int. perm.	**8.00E-18**
Kzz int. perm.	**8.00E-18**
Reference porosity	**0**
Minimum	**0**

Table 6.6 Thermal parameters used for the granitic rock in the OBC case to perform the numerical analysis in the buffer exercise.

Parameter	Value
λ_{dry}	**3.6**
λ_{wet}	**3.6**

The following figures show the evolution of temperature, liquid degree of saturation, liquid pressure and stresses at different locations along the system determined with the OBC model.

Figure 6.6 shows the evolution of temperature inside the buffer for a period of 1 year (365 days) at different positions from the canister. It is observed an increase in the temperature values in all the positions up to the first 30 days. After this time, it can be noted that the values start to stabilize, reaching a steady state condition. This can be seen in the long term predictions (Figure 6.7) where the model predicts a constant temperature up to 1000 years. As expected, the value of temperature in the heat source reaches a maximum value of 100 °C. On the other hand, the location at 0.75 m from the canister shows the minimum temperature in the barrier after 1000 years with a value of 60 °C.

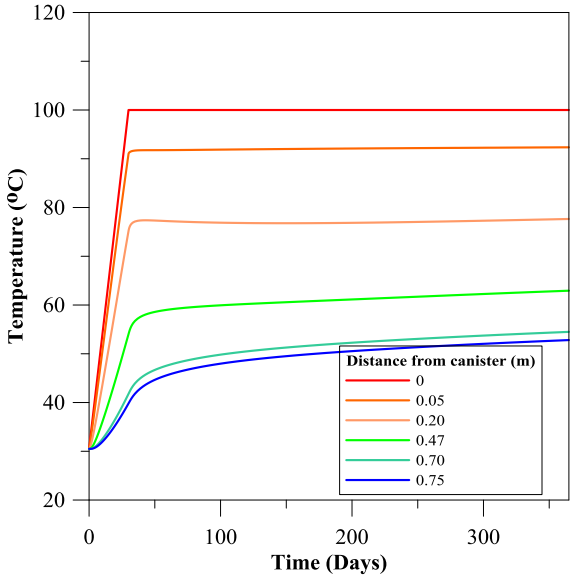

Figure 6.6 Evolution of temperature inside the bentonite buffer up to 365 days (1 year) at different positions from the canister.

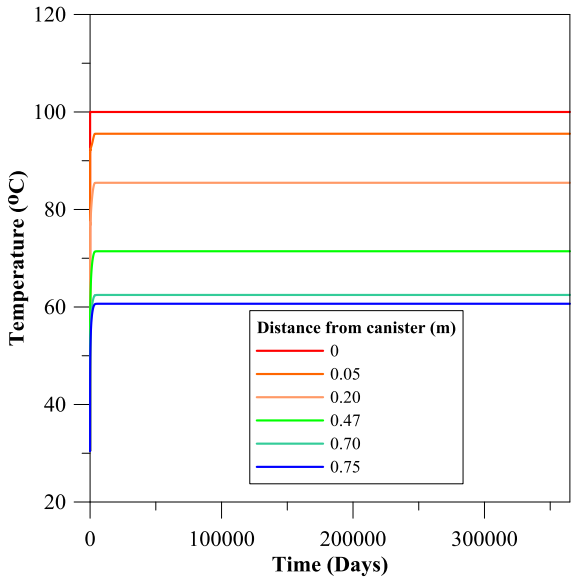

Figure 6.7 Evolution of temperature inside the bentonite buffer up to 365000 days (1000 years) at different positions from the canister.

Figure 6.8 shows the evolution of temperature in the granitic rock for a period of 1 year (365 days) at different positions from the canister. It is observed an increase in the temperature values in all the positions up to the first 30 days. After this time, it can be noted that the values start to stabilize, reaching a steady state condition. This can be seen in the long term predictions (Figure 6.9) where the model predicts a constant temperature up to 1000 years. According to the plot, the range of temperature expected in the granite is between 35 °C and 60 °C. This means that in general, the minimum temperature expected after 1000 years in the repository is around 35 °C.

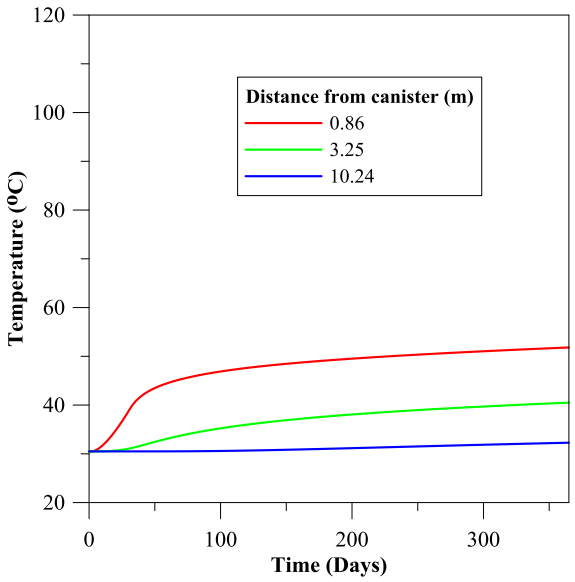

Figure 6.8 Evolution of temperature inside the granitic rock up to 365 days (1 year) at different positions from the canister.

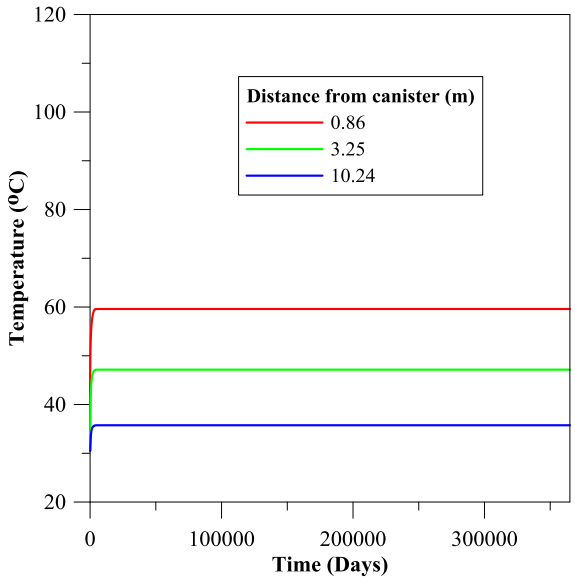

Figure 6.9 Evolution of temperature inside the granitic rock up to 365000 days (1000 years) at different positions from the canister.

The results of liquid degree of saturation are shown in the following figures. Figure 6.10 shows the predicted values of the degree of saturation for different positions inside the buffer. In the positions close to the hydration front (away from the canister), an increase in the values can be observed as saturation continues. The saturation rate in these positions is very high and as a result, they achieve a fully saturation condition in a considerable short time (around 4 years). However, as we moved closer to the canister, we can see a decrease in the hydration rate that leads to longer periods of time to reach fully saturation. Another important observation regarding the sections close to the heat source is the drying experienced in these locations at early stages of the simulations. This episode starts with a reduction in the values of degree of saturation up to the first year (365 days). After that period of time, the values start to increase and saturation is achieved at the first 10 years. As we can see, the model is predicting that the buffer will

be fully saturated after 10 years of hydration. Considering the time required for the complete decay of the thermal power of the stored fuel elements, that can be in the range of millions of years, the saturation time is not enough to provide the adequate safety functions for the repository.

Regarding the results obtained from the positions inside the granitic rock, it can be noted from Figure 6.11 that a fully saturation condition was achieved in a very short time. The position closer to the canister, reached full saturation in around 50 days.

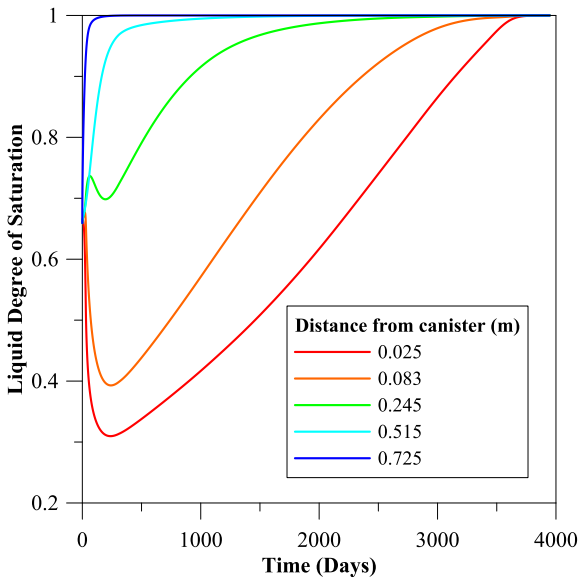

Figure 6.10 Evolution of liquid degree of saturation inside the bentonite buffer up to 3650 days (10 years) at different positions from the canister.

Liquid pressure is another variable that can be used to study the hydraulic behavior inside the repository system. Figure 6.12 shows the numerical results of liquid pressure inside the bentonite buffer at different positions from the canister. The positions close to the hydration source, experience an increase in the liquid pressure because of the

progressive saturation occurring in this boundary. A value of zero liquid pressure is achieved due to a fully saturation condition. On the other hand, the locations near to the canister experienced a reduction in the values of liquid pressure because of the drying taking place in this area. The drying process starts when there is a desaturation in the pore space. In this scenario, the liquid water inside the pores is transformed to vapor, resulting in an increase of gas pressure that leads to a decrease in the liquid pressure. After a period of time this process is reversed and the liquid pressure starts to increase until it reaches a fully saturation condition where it has a value equal to zero. The time at which this condition occurs is around 10 years. This confirms the time to reach fully saturation conditions, determined previously. The results from the points located inside the granite are shown in Figure 6.13.

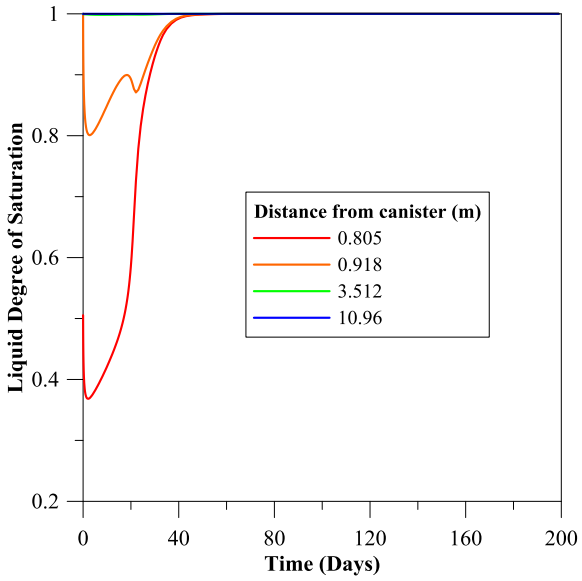

Figure 6.11 Evolution of liquid degree of saturation inside the granitic rock up to 200 days at different positions from the canister.

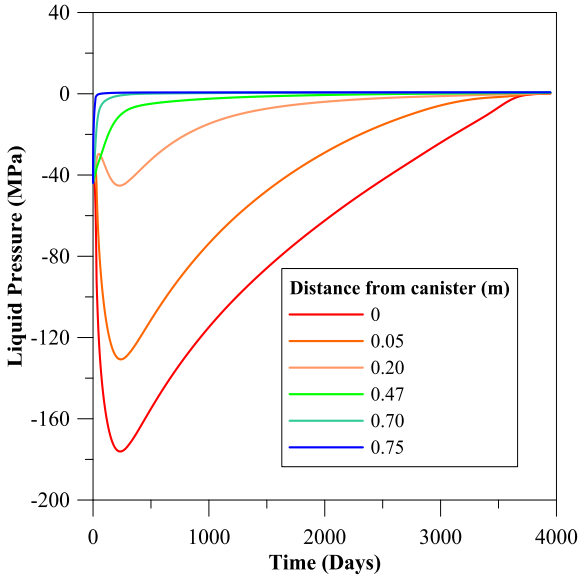

Figure 6.12 Evolution of liquid pressure inside the bentonite buffer up to 3650 days (10 years) at different positions from the canister.

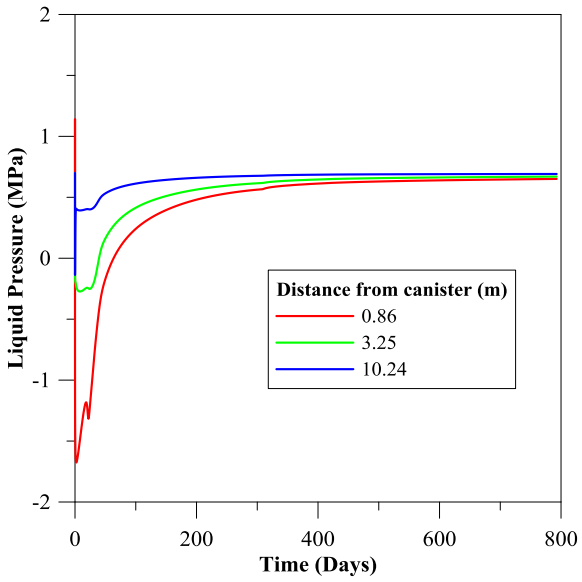

Figure 6.13 Evolution of liquid pressure inside the granitic rock up to 800 days at different positions from the canister.

The mechanical behavior of the repository can be analyzed by determine the evolution of normal stress on each component of the system. Figure 6.14 presents the numerical results of normal stress at different points along the buffer. It can be observed that the stresses in all the positions are increasing as the saturation in the buffer progresses. Since this is a constant volume exercise, the stresses represent the swelling pressures generated by the bentonite expansion. As we can see from the figure, the point closest to the hydration front is the one with the maximum value of stress close to 5.60 MPa. Once saturation is achieved, the swelling pressure remains constant until the end of the simulation. Figure 6.15 shows the results of the evolution of stress obtained from different positions along the granite.

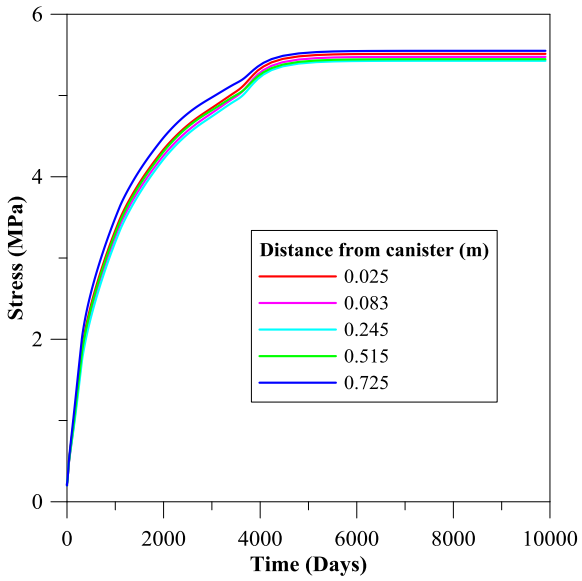

Figure 6.14 Evolution of normal stress inside the bentonite buffer up to 10000 days at different positions from the canister.

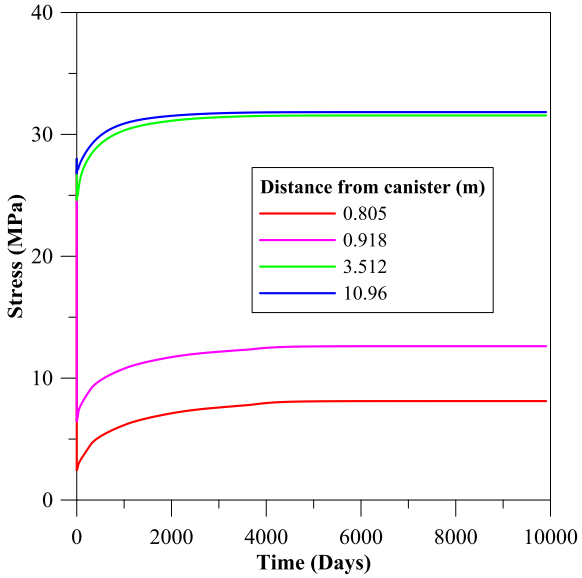

Figure 6.15 Evolution of normal stress inside the granitic rock up to 10000 days at different positions from the canister.

6.2.4 Thermo-Osmosis

The following figures show the evolution of temperature, liquid degree of saturation, liquid pressure and stresses at different locations along the system determined with the thermo-osmosis model. Additional results can be found in section A.2 of the appendix.

Figure 6.16 shows the evolution of temperature inside the buffer for a period of 1 year (365 days) at different positions from the canister. It is observed an increase in the temperature values in all the positions up to the first 30 days. After this time, it can be noted that the values start to stabilize, reaching a steady state condition. This can be seen in the long term predictions (Figure 6.17) where the model predicts a constant

temperature up to 1000 years. As expected, the value of temperature in the heat source reaches a maximum value of 100 °C. On the other hand, the location at 0.75 m from the canister shows the minimum temperature in the barrier after 1000 years with a value close to 57 °C.

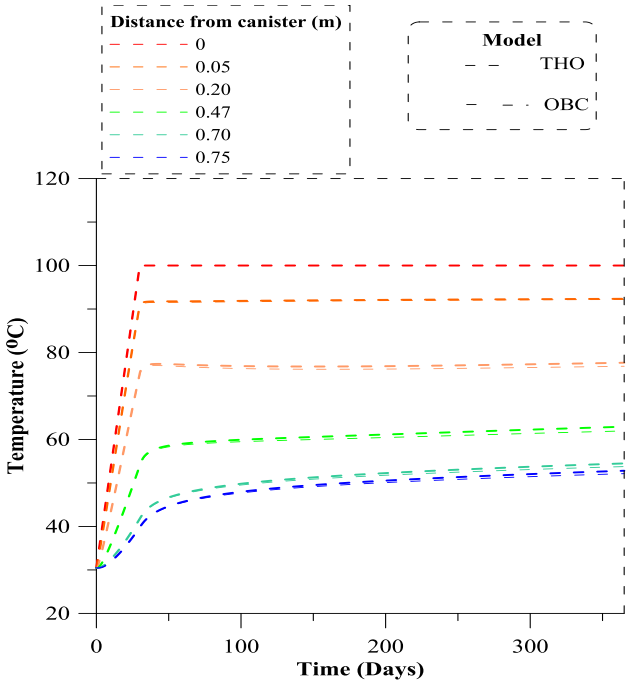

Figure 6.16 Evolution of temperature inside the bentonite buffer up to 365 days at different positions from the canister.

The two models showed similar predictions of temperature at early stages of the exercise. However, as the hydration progresses, the long term predictions obtained from the thermo-osmosis were lower than those determined with the OBC. It is possible that the decrease in temperature is related to the movement of water as liquid from the hot zone to other locations inside the barrier.

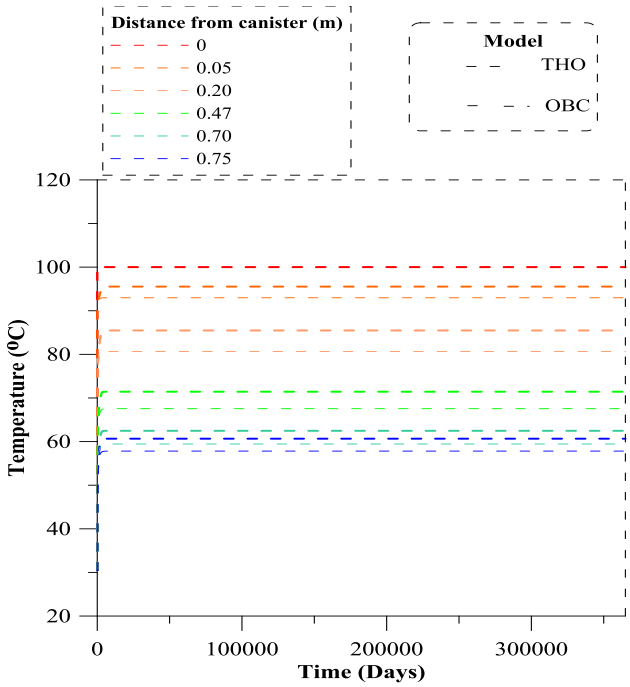

Figure 6.17 Evolution of temperature inside the bentonite buffer up to 365000 days (1000 years) at different positions from the canister.

Figure 6.18 shows the evolution of temperature in the granitic rock for a period of 1 year (365 days) at different positions from the canister. It is observed an increase in the temperature values in all the positions up to the first 30 days. After that time, it can be noted that the values start to stabilize, reaching a steady state condition. This can be seen in the long term predictions (Figure 6.19) where the model predicts a constant temperature up to 1000 years. According to the plot, the range of temperature expected in the granite is between 35 °C and 57 °C. This means that in general, the minimum temperature expected after 1000 years in the repository is around 35 °C.

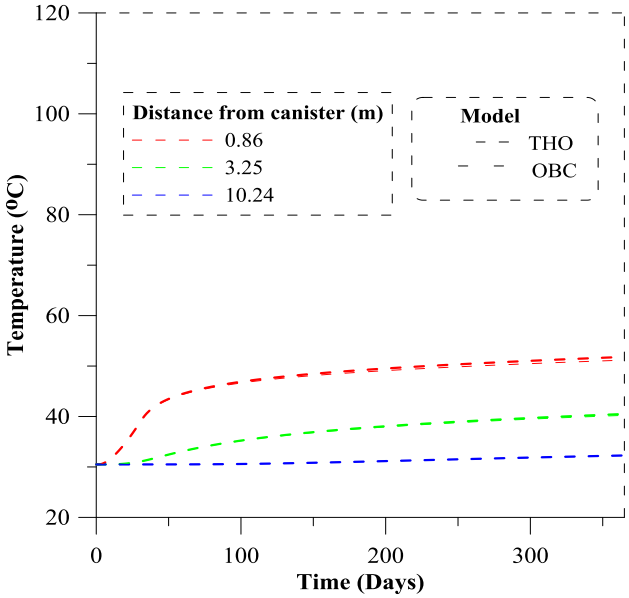

Figure 6.18 Evolution of temperature inside the granitic rock up to 365 days at different positions from the canister.

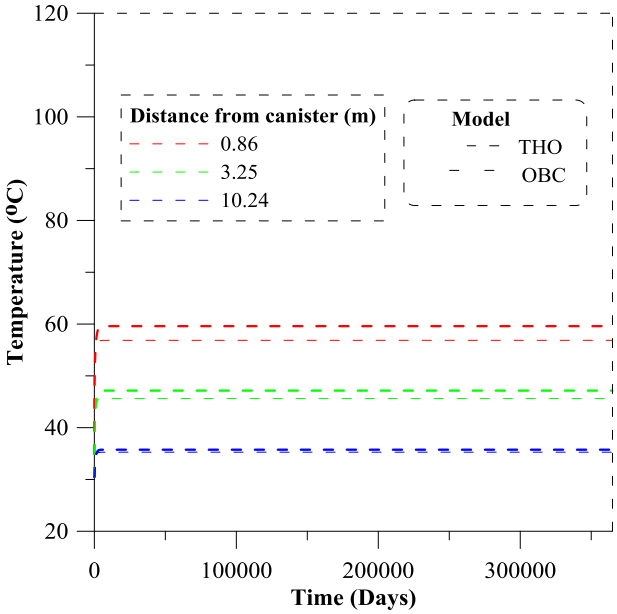

Figure 6.19 Evolution of temperature inside the granitic rock up to 365000 days (1000 years) at different positions from the canister.

The results of liquid degree of saturation are shown in the following figures. Figure 6.20 shows the predicted values of degree of saturation with the thermo-osmosis and OBC models for different positions inside the buffer. It can be observed from the figure how the thermo-osmosis model was able to slow down the hydration rate inside the buffer in a significant way, especially in the positions closer to the canister. This reduction in the hydration of the bentonite is mainly due to the thermo-osmotic flux that transfers the water in the liquid phase from the zones close to the heater to those with lower temperature. The incorporation of this model to the analysis delayed the time require to reach fully saturation giving rise to more realistic results in which the barrier remains unsaturated.

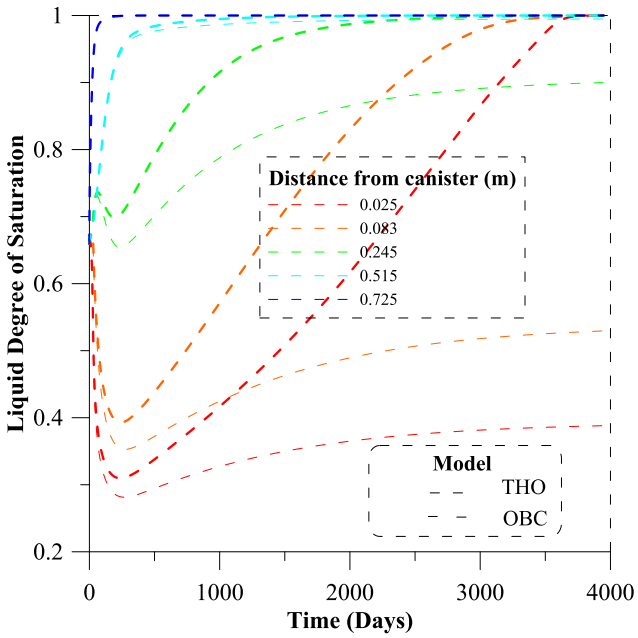

Figure 6.20 Evolution of liquid degree of saturation inside the bentonite buffer up to 3650 days (10 years) at different positions from the canister.

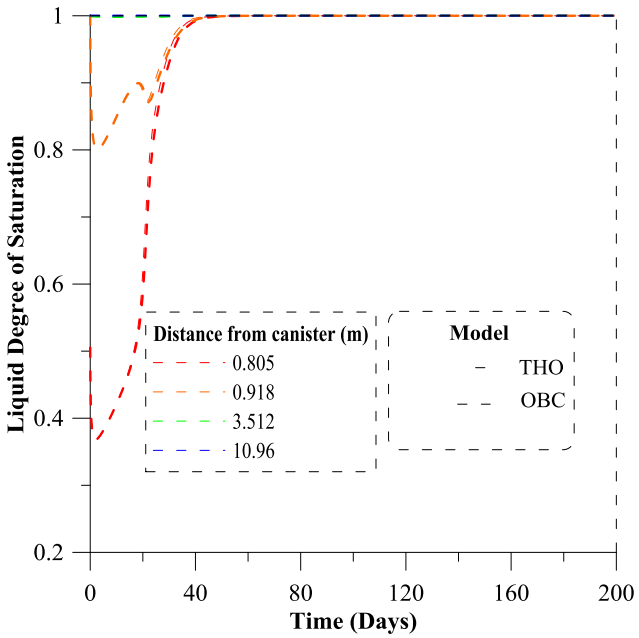

Figure 6.21 Evolution of liquid degree of saturation inside the granitic rock up to 200 days at different positions from the canister.

Regarding the liquid degree of saturation in the granitic rock, it can be seen that both models gave similar predictions. According to Figure 6.21, the predicted time for fully saturation in the rock is around 50 days.

Figure 6.22 shows the numerical results of liquid pressure inside the bentonite buffer at different positions from the canister determined by the thermo-osmosis model. The positions close to the hydration source, experience an increase in the values of liquid pressure because of the progressive saturation occurring in this boundary. These locations are barely affected by the thermo-osmotic flow and as a result, similar predictions are obtained from the two models. On the other hand, the locations near to the canister experienced an important reduction in the values of liquid pressure because

of the drying taking place in this area. The results from the points located inside the granite are shown in Figure 6.23.

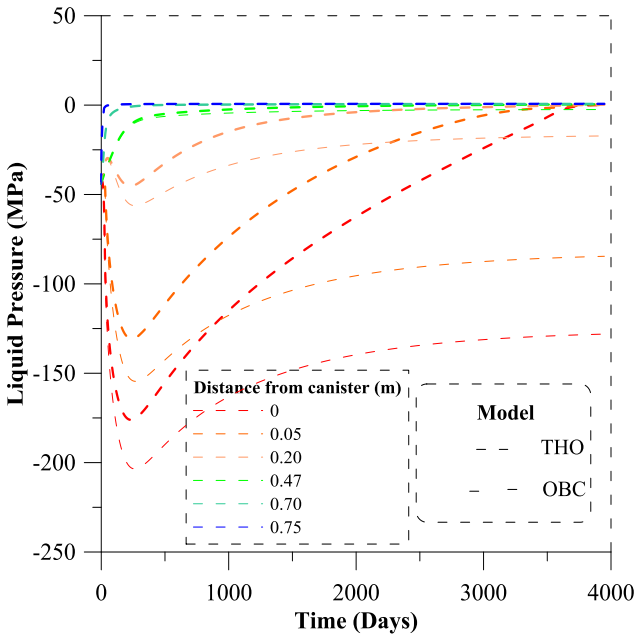

Figure 6.22 Evolution of liquid pressure inside the bentonite buffer up to 3650 days (10 years) at different positions from the canister.

The mechanical behavior of the repository can be analyzed by determine the evolution of normal stress on each component of the system. Figure 6.24 presents the numerical results of normal stress at different points along the buffer determined with the thermo-osmosis OBC models. It can be observed that the stresses in all the positions are increasing as the saturation in the buffer progresses. Since this is a constant volume exercise, the stresses represent the swelling pressures generated by the bentonite expansion. As we can see from the figure, the point closest to the hydration front is the one with the maximum value of stress close to 3.40 MPa. This value is much lower to the one obtained from the OBC model. This reduction in the swelling pressures is related

to the reduction in the hydration rate inside the barrier. Figure 6.25 shows the results of the evolution of stress obtained from different positions along the granite.

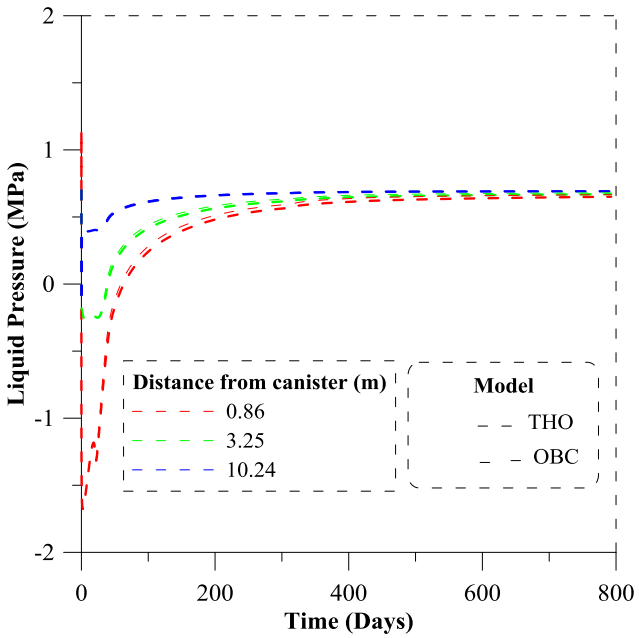

Figure 6.23 Evolution of liquid pressure inside the granitic rock up to 800 days at different positions from the canister.

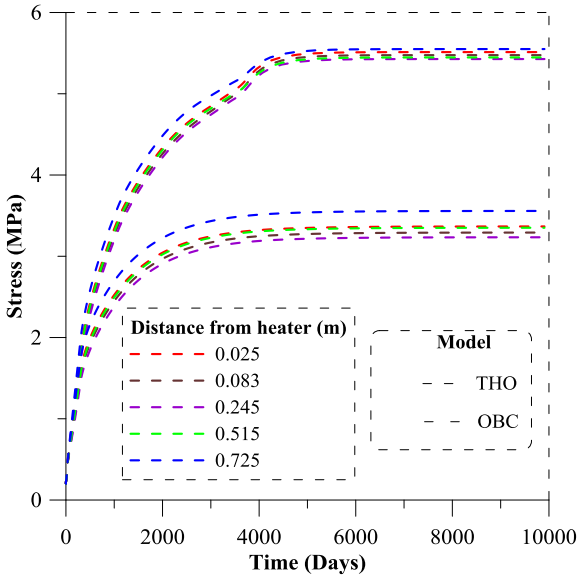

Figure 6.24 Evolution of normal stress inside the bentonite buffer up to 10000 days at different positions from the canister.

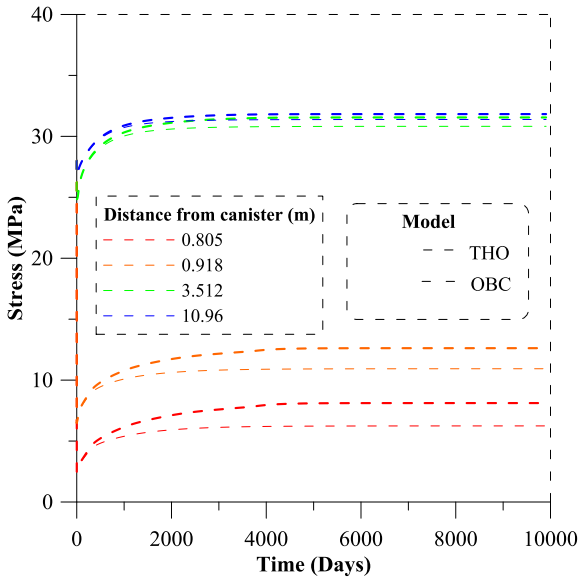

Figure 6.25 Evolution of normal stress inside the granitic rock up to 10000 days at different positions from the canister.

7. CONCLUSION

The aim of this thesis focused on the explanation of the reduction in the hydration rate of the bentonite engineered barrier subjected to THM coupled phenomena under nuclear repository conditions. The coupled phenomena occurring in this low permeability environment makes the behavior of these materials quite complex. Therefore, it is important to use a complete mathematical formulation suitable for dealing with this type of problem. In addition, it is relevant to provide sufficient experimental data that can be used to calibrate the proposed models. The following summarizes the main conclusions from the work presented in the previous sections.

In order to solve the problem of low permeability media, it was necessary to present a complete mathematical formulation that considered the phenomena in this environment. Section 2 presented a complete multiphase, multispecies THM formulation proposed by Olivella et al., 1994 consisted of balance equations, constitutive equations and equilibrium restrictions. However, as it was discussed previously, THM models based on this formulation were not able to reproduce the hydraulic behavior observed in expansive clays used as engineered barriers. The main differences between the experimental data and model predictions were related to the hydration rate of these materials. The hydration rate was reduced at advanced stages during infiltration experiments, leading to an overestimation of model predictions. In order to find an explanation for the reduction in the hydration rate observed in these tests, additional phenomena have been incorporated. For instance, the threshold hydraulic gradient that is

associated with the non-Darcian behavior found on expansive clays when small hydraulic gradients are applied. Another phenomenon considered was the thermo-osmosis. This phenomenon occurs when the hydraulic gradient becomes smaller and a thermal gradient is present. The flow of liquid due to coupled phenomena could have an effect in the hot sections causing a tendency to slow down the hydration in these areas. The last phenomenon incorporated to this formulation is related to the change in material fabric occurring inside the bentonite. The double structure model proposed by Sánchez et al., 2005 considers two structural levels in the FEBEX bentonite and the interaction between them. The model suggests that the swelling taking place at the particle level blocks the pores between particles, reducing the space for water to flow.

In order to measure the performance of the proposed mathematical formulation and the non-traditional models, experimental data of temperature and relative humidity from two small scale laboratory infiltration tests under isothermal and non-isothermal conditions were used. In general terms, all the models performed very well predicting the temperature values along the cells. On the other hand, regarding the results of relative humidity, the Operational Base Case (OBC) model was not able to capture the trend of the observations especially the ones near the heater. The model overestimated the measurements, predicting a faster hydration in the barrier. Once the other models were incorporated to the analysis, there was a significant improvement in the numerical results by reducing the hydration rate in the bentonite resulting in more accurate predictions. The model predictions obtained from the threshold hydraulic gradient (THG) approach were satisfactory under isothermal and non-isothermal conditions.

However, some discrepancies were observed in the long-term predictions in which the model underestimates the measurements at isothermal conditions and showed a tendency to maintain constant values for the non-isothermal case. Regarding the results obtained from the thermo-osmosis (THO) model, as expected, this phenomenon had no effect during isothermal conditions due to the absence of a thermal gradient. On the other hand, when the cell was subjected to non-isothermal conditions, an improvement in the model predictions was observed. The model was able to reproduce the general trend of the observations by reducing the measured values of relative humidity, especially in the position closest to the heater. This reduction in relative humidity is due to the movement of water in the liquid phase from the heat source at advanced stages of the test. Concerning the double structure approach, the model was capable to reproduce the behavior showed by the observations, predicting values closer to the actual measurements. The model showed first class results, especially in the long-term, where the predicted rate was very close to the one observed from the measurements. In general terms, the double structure model was the one with the best agreement between the measurements and the computed results. In addition to the presented models, a combination of the double structure and thermo-osmosis approach was proposed to study the effect on the numerical predictions. The combination of these two models resulted in a very good prediction of the observed values. In summary, the numerical results obtained from the analysis performed to study the hydraulic behavior in the small infiltration tests imply that the fabric changes taking place inside the bentonite is the phenomenon with the most influence in the hydraulic behavior of this material.

The mock-up test performed by CIEMAT was another experiment used to measure the performance of the proposed models. In this almost full scale experiment, the main THM variables were measured: temperature, water intake, relative humidity and total pressures. In general, all the models were able to reproduce the thermal behavior inside the barrier by predicting very good values of temperature along the system. However, as expected, not all the models were able to capture the hydraulic behavior showed by the bentonite. The OBC model was not able to properly predict the measurements of water intake and relative humidity especially in zones close to the heater. On the other hand, the threshold hydraulic gradient was capable to reproduce very well the measured values of relative humidity in sections inside and outside the heater zone. This model also predicted very well the observed values of water intake, showing an improvement in the numerical results. As expected, the thermo-osmosis model did not have an effect in the numerical results for the sections located outside the heater area. However, an improvement in the predictions was achieved in sections inside the heater zone. The model was able to reduce the values of relative humidity in the positions close to the heater. Nevertheless, an overestimation of the measurements was observed in this particular area. Regarding the water intake, the numerical results obtained with this model overestimated the measured values. These discrepancies between the measurements and model predictions of the water intake result in the overestimation observed on the computed values of relative humidity. Concerning the numerical results of relative humidity determined by the double structure model, a good agreement with the measured values was achieved especially for the sections inside the

heater zone. However, a small under estimation was observed in the position closest to the heater. This small underestimation is also observed in the predictions of water intake measurements, predicting a higher reduction in the hydration rate. In order to improve the predictions of the hydraulic behavior in the barrier, a modified version of the double structure was incorporated. The parameters of this model were based on those used in the infiltration tests. The change in the intrinsic permeability and the retention curve of the bentonite significantly influenced the hydraulic behavior predicted by the model. The modified model predicted very well the observations of relative humidity in all sections especially those located inside the heater zone.

The THM evolution of a bentonite buffer in a real repository was also studied. In this particular case, no experimental data was available and the analysis was purely numerical. The analysis was carried out with a two dimensional mesh and with the typical initial and boundary conditions found in a repository. The numerical simulations were performed with the OBC and thermo-osmosis (THO) model to determine the evolution of temperature, liquid degree of saturation, liquid pressure and total stresses for a period of 1000 years. The OBC model reproduced the typical hydraulic behavior observed under repository conditions by showing the common trends of drying in the zones close to the heat source and wetting in the areas close to the hydration front. However, it is believed that the model overpredicted the hydration rate in the buffer by estimating a saturation time of 10 years. On the other hand, regarding the mechanical results, the model predicted a maximum stress of 5.6 MPa in the buffer. This value of stress corresponds to the swelling pressure experienced inside the bentonite. Regarding

the results obtained from the THO model, it was observed a significant reduction in the hydration rate inside the barrier. After the long term predictions up to 1000 years, the positions close to the canister still unsaturated with values of degree of saturation around 40 %. On the other hand, regarding the mechanical results, the model predicted a maximum swelling pressure of 3.4 MPa, lower than value predicted by the OBC. These results should be considered as preliminary to have a better idea of the behavior of a bentonite buffer under real repository conditions. In order to have a more complete analysis, other models like the threshold hydraulic gradient and double structure need to be considered.

The presented work was able to study the THM evolution of the FEBEX bentonite under nuclear repository conditions. The reduction in the hydration rate inside the bentonite barrier observed during experimental infiltration tests was approached with the proper THM mathematical formulation incorporating the appropriate phenomena affecting the flow inside this material. Two experimental tests and one synthetic case were used to assess the performance of the models and to determine which of the phenomena explain better the hydraulic behavior observed in these tests. It is important to highlight the remarkable results obtained from the double structure in the small infiltration tests and the threshold hydraulic gradient model in the mock-up test.

REFERENCES

Alonso, E. E. (1998). "Modelling expansive soil behavior". Second International Conference on Unsaturated Soils. Beijing, China. **1:** 37-70.

Chapman, N. A. a. M. K., I. G. (1987). The geological disposal of nuclear waste. Chichester, John Wiley.

Cui, Y. J., Tang, A. M. , Loiseau, C. , Delage, P. (2008). "Determining the unsaturated hydraulic conductivity of a compacted sand-bentonite mixture under constant volume and free-swell conditions." Phys. Chem. Earth **33**: S462-S471.

Dixon, D. A., Gray, M. N. , Hnatiw, D. (1992). "Critical gradients and pressures in dense swelling clays." Canadian Geotechnical Journal **29**: 1113-1119.

Dixon, D. A., Graham, J. , Gray, M. N. (1999). "Hydraulic conductivity of clays in confined tests under low hydraulic gradients." Canadian Geotechnical Journal **36**(5): 815-825.

Dixon, D. A., Chandler, N. , Graham, J. , and Gray, M. N. (2002). "Two large-scale sealing tests conducted at Atomic Energy of Canada's underground research laboratory: the buffer–container experiment and the isothermal test." Canadian Geotechnical Journal **39**: 503-518.

Djeran, I. (1993). "Étude des duffusions thermique et hydraulique dans una argile soumise á un champ de température". Sciences et techniques nucléaires rapport. Luxembourg, Commission des Communautés européennes.

ENRESA (1998). "Preoperational Thermo-Hydro-Mechanical (THM) modelling of the 'mock-up' test. FEBEX Report". Madrid, ENRESA.

ENRESA (2000). "Full-scale engineered barriers experiment for a deep geological repository for high level radioactive waste in crystalline host rock". Brussels, European Commission.

Fernández, A. M., Baeyens, B., Bradbury, M. & Rivas, P. (2003). "Analysis of the pore water chemical composition of a Spanish compacted bentonite used in an engineered barrier." Phys. Chem. Earth **29**(1): 105-118.

Gens, A., Alonso, E. E. (1992). "A framework for the behaviour of unsaturated expansive clays." Canadian Geotechnical Journal **29**: 1013-1032.

Gens, A., Olivella, S. (2000). "Vapour Transport in Low Permeability Unsaturated Soils with Capillary Effects." Transport in Porous Media **40**: 219-241.

Gens, A. (2003). "The role of geotechnical engineering for nuclear energy utilization". Proceeding of XIII European Conference of Soils Mechanics and Geotechnical Engineering. Prague.

Gens, A., Alonso, E.E. (1992). "A framework for the behaviour of unsaturated expansive clays." Canadian Geotechnical Journal **29**: 1013-1032.

Gurr, C. G., Marshall, T. J. , and Hutton, J. T. (1952). "Movement of water in soil due to a temperature gradient." Soil Science **74**(5): 335-345.

Hansbo, S. (2001). "Consolidation equation valid for both Darcian and non-Darcian flow." Géotechnique **51**(1): 51-54.

Hueckel, T., Borsetto, M. (1990). "Thermoplasticity of Saturated Soils and Shales: Constitutive Equations." Journal of Geotechnical Engineering **116**(12): 1765-1777.

Liu, H., Birkholzer, J. (2012). "On the relationship between water flux and hydraulic gradient for unsaturated and saturated clay." Journal of Hydrology **475**: 242-247.

Liu, H., Lianchong, L. , Birkholzer, J. (2012). "Unsaturated properties for non-Darcian water flow in clay." Journal of Hydrology **430**: 173-178.

Neuzil, C. E. (1986). "Groundwater flow in low permeability environments." Water Resources Research **22**(8): 1163-1195.

Olivella, S., Carrera, J. , Gens, A. , and Alonso, E. E. (1994). "Nonisothermal Multiphase Flow of Brine and Gas Through Saline Media." Transport in Porous Media **15**: 271-293.

Sánchez, M., Gens, A. (2001). "Report on THM modelling results FEBEX II". Barcelona, Universitat Politecnica de Catalunya (UPC).

Sánchez, M., Gens, A. , Guimaraes, L. , and Olivella, S. (2005). "A double structure generalized plasticity model for expansive materials." International Journal for Numerical and Analytical Methods in Geomechanics **29**: 751-787.

Sánchez, M., Villar, M. V. , Lloret, A. , Gens, A. (2007). "Analysis of the expansive clay hydration under low hydraulic gradient." Experimental Unsaturated Soil Mechanics **112**: 309-318.

Sánchez, M., Gens, A. , and Olivella, S. (2010). "Effect of thermo-coupled processes on the behaviour of a clay barrier submitted to heating and hydration." Annals of the Brazilian Academy of Sciences **82**(1): 153-168.

Sánchez, M., Gens, A. and Olivella, S. (2012). "THM analysis of a large scale heating test incorporating material fabric changes." International Journal for Numerical and Analytical Methods in Geomechanics **36**: 391-421.

Sears, F., Zemansky, S. (1966). Física. Madrid, Aguilar.

Soler, J. (1999). "Coupled transport phenomena in the opalinus clay: implications for radionuclide transport". Wettingen, Paul Scherrer Institut.

Steefel, C., Rutqvist, J. , Tsang, C. , Liu, H. , Sonnenthal, E. , Houseworth, J. , Birkholzer, J. (2010). "Reactive Transport and Coupled THM Processes in Engineering Barrier Systems (EBS)". California, Lawrence Berkeley National Laboratory.

Thomas, H., Cleall, P., Chandler, N., Dixon, D., & Mitchell, H. (2003). "Water infiltration into a large-scale in-situ experiment in an underground research laboratory." Géotechnique **53**: 207-224.

Villar, M. V., Martín, P., Lloret, A. & Romero, E. (2004). "Final Report on Thermo-Hydro-Mechanical Laboratory Test FEBEX II". Madrid, ENRESA.

Villar, M. V., Gómez-Espina, R. (2009). "Report on Thermo-Hydro-Mechanical Laboratory Tests Performed by CIEMAT on Febex Bentonite 2004-2008". Madrid, CIEMAT

Villar, M. V., Martín P. L. , Bárcena, I. , García-Siñeriz, J. L. , Gómez-Espina, R. , Lloret, A. (2012). "Long-term experimental evidences of saturation of compacted bentonite under repository conditions " Engineering Geology **149**: 57-69.

Wu, Y., Pruess, K. (1998). "A numerical method for simulating non-Newtonian fluid flow and displacement in porous media." Advances in Water Resources **21**: 351-362.

Zheng, L., Samper, J. (2008). "A coupled THMC model of FEBEX mock-up test." Phys. Chem. Earth **33**: S486-S498.

Zheng, L., Samper, J. , Montenegro, L. , Fernández, A. M. (2010). "A coupled THMC model of a heating and hydration laboratory experiment in unsaturated compacted FEBEX bentonite." Journal of Hydrology **386**: 80-94.

Zou, Y. (1996). "A non-linear permeability relation depending on the activation energy of pore liquid " Géotechnique **46**(4): 769-774.

APPENDIX

This appendix includes supplemental information to the analysis presented in sections 5 and 6 regarding the Mock-up test and bentonite buffer exercise, respectively.

A.1Mock-Up Test

In order to have a better understanding on the performance of the models, the following plots are presented. These plots show the evolution of relative humidity in all sections where the measurements were taken at different radii with the corresponding model prediction (OBC, THG, THO, DS) for a period of 6000 and 10950 days.

A.1.1 Operational Base Case

The following figures show the numerical results of relative humidity obtained with the OBC model. Figure A.1 presents the results of relative humidity for sections A3 & B3, A4 & B4, A6 & B6, A7 & B7 and AB corresponding to a radius of 0.70 m from the heater. Figure A.2 shows the long term evolution of relative humidity for the same position up to 10950 days (30 years). It is important to mention that up to this point, the bentonite still unsaturated with a maximum model prediction around 99 %.

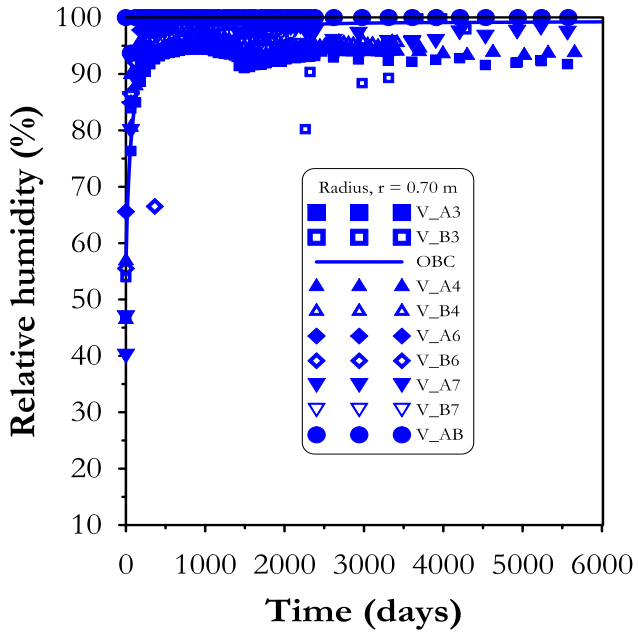

Figure A.1. Evolution of relative humidity for a radius, r = 0.70 m. Measurements (scatter points) and OBC model prediction (solid line) up to 6000 days.

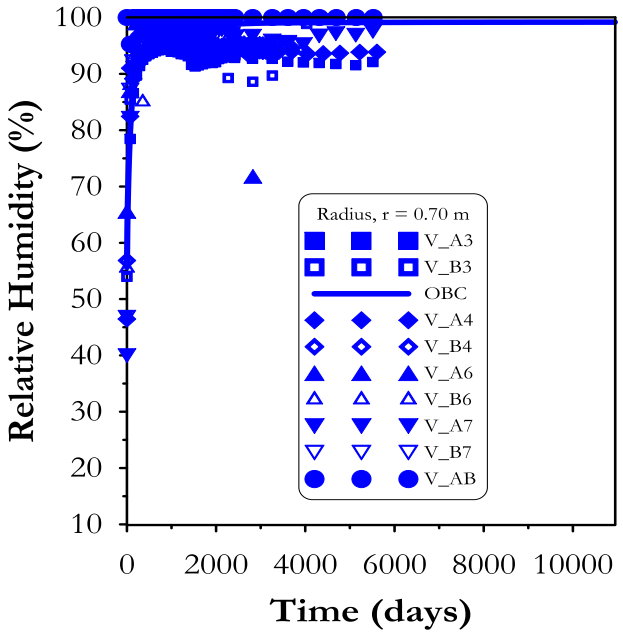

Figure A.2. Evolution of relative humidity for a radius, r = 0.70 m. Measurements (scatter points) and OBC model prediction (solid line) up to 10950 days.

Figure A.3 shows the results of relative humidity for sections A3 & B3, A4 & B4, A6 & B6, A7 & B7 and AB corresponding to a radius of 0.55 m from the heater. Figure A.4 presents the long term evolution of relative humidity for the same position up to 10950 days (30 years).

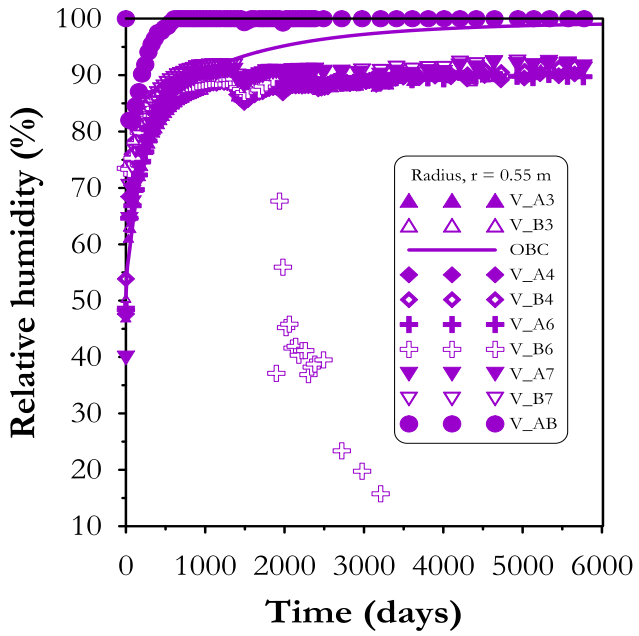

Figure A.3. Evolution of relative humidity for a radius, r = 0.55 m. Measurements (scatter points) and OBC model prediction (solid line) up to 6000 days.

Figure A.5 presents the results of relative humidity for sections A3 & B3, A4 & B4, A6 & B6, A7 & B7 and AB corresponding to a radius of 0.37 m from the heater. Figure A.6 shows the long term evolution of relative humidity for the same position up to 10950 days (30 years).

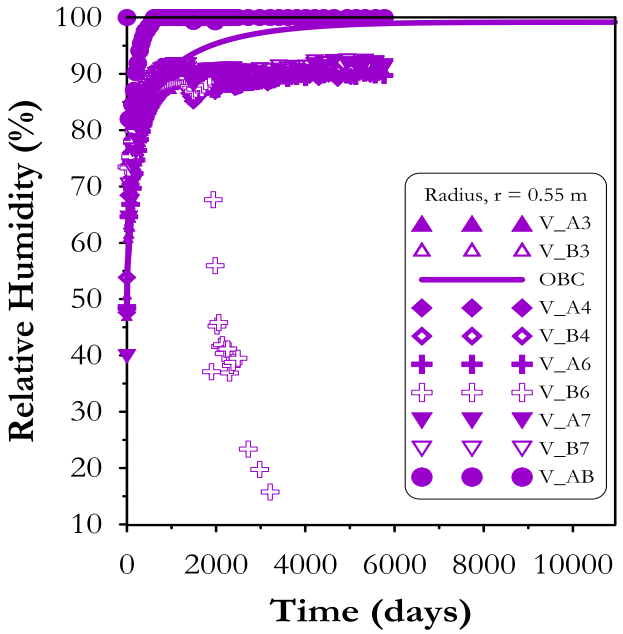

Figure A.4. Evolution of relative humidity for a radius, r = 0.55 m. Measurements (scatter points) and OBC model prediction (solid line) up to 10950 days.

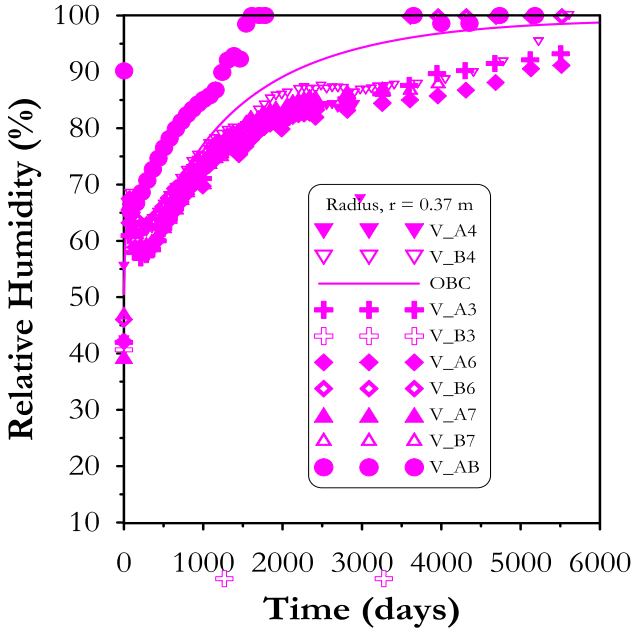

Figure A.5. Evolution of relative humidity for a radius, r = 0.37 m. Measurements (scatter points) and OBC model prediction (solid line) up to 6000 days.

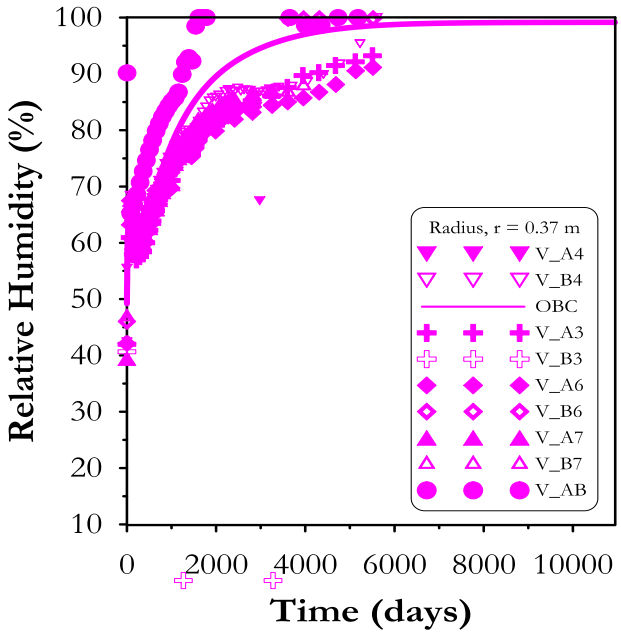

Figure A.6. Evolution of relative humidity for a radius, r = 0.37 m. Measurements (scatter points) and OBC model prediction (solid line) up to 10950 days.

Figure A.7 presents the results of relative humidity for sections A3 & B3, A4 & B4, A6 & B6, A7 & B7 and AB for the closest location to the heater. This location corresponds to a radial distance of 0.22 m. Figure A.8 shows the long term evolution of relative humidity for the same position up to 10950 days (30 years).

In general, the OBC model overestimates the measured values of relative humidity in all sections at different radial distances. The most significant difference between measurements and model predictions was observed in the closest position to the heater.

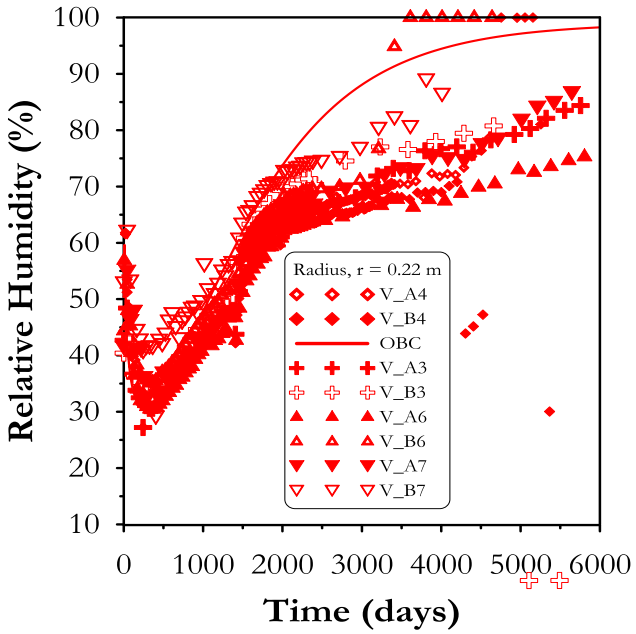

Figure A.7. Evolution of relative humidity for a radius, r = 0.22 m. Measurements (scatter points) and OBC model prediction (solid line) up to 6000 days.

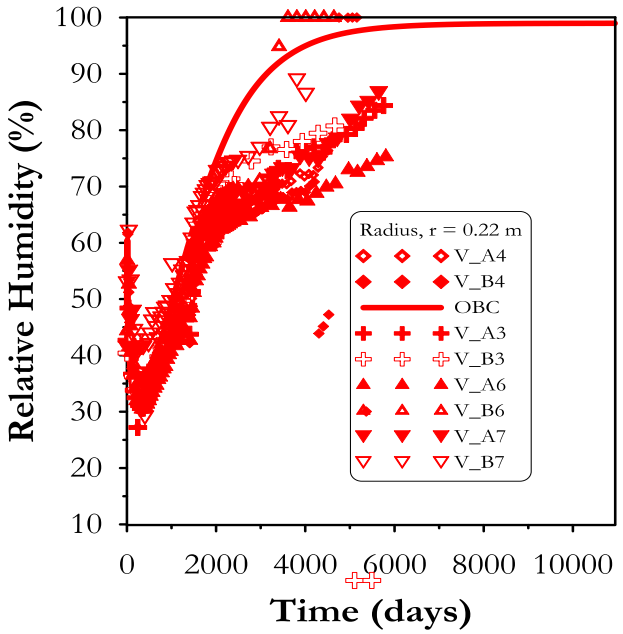

Figure A.8. Evolution of relative humidity for a radius, r = 0.22 m. Measurements (scatter points) and OBC model prediction (solid line) up to 10950 days.

A.1.2 Threshold Hydraulic Gradient

The following figures show the numerical results of relative humidity obtained with the THG model. Figure A.9 presents the results of relative humidity for sections A3 & B3, A4 & B4, A6 & B6, A7 & B7 and AB corresponding to a radius of 0.70 m from the heater. Figure A.10 shows the long term evolution of relative humidity for the same position up to 10950 days (30 years).

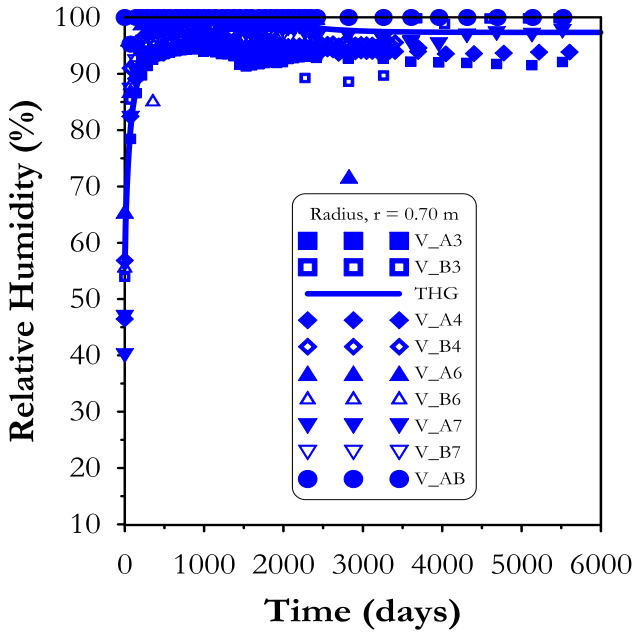

Figure A.9. Evolution of relative humidity for a radius, r = 0.70 m. Measurements (scatter points) and THG model prediction (solid line) up to 6000 days.

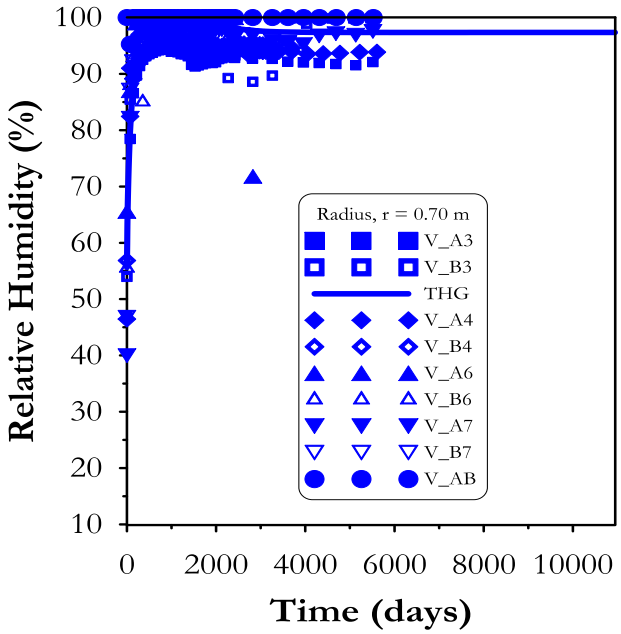

Figure A.10. Evolution of relative humidity for a radius, r = 0.70 m. Measurements (scatter points) and THG model prediction (solid line) up to 10950 days.

Figure A.11 shows the results of relative humidity for sections A3 & B3, A4 & B4, A6 & B6, A7 & B7 and AB corresponding to a radius of 0.55 m from the heater. Figure A.12 presents the long term evolution of relative humidity for the same position up to 10950 days (30 years).

The results corresponding to a radius of 0.37 m from the heater are shown in Figure A.13. Figure A.14 shows the long term evolution of relative humidity for the same position up to 10950 days (30 years).

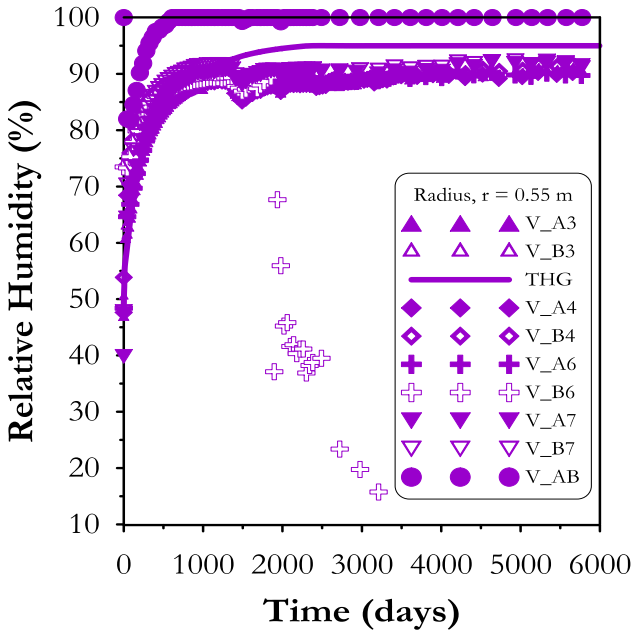

Figure A.11. Evolution of relative humidity for a radius, r = 0.55 m. Measurements (scatter points) and THG model prediction (solid line) up to 6000 days.

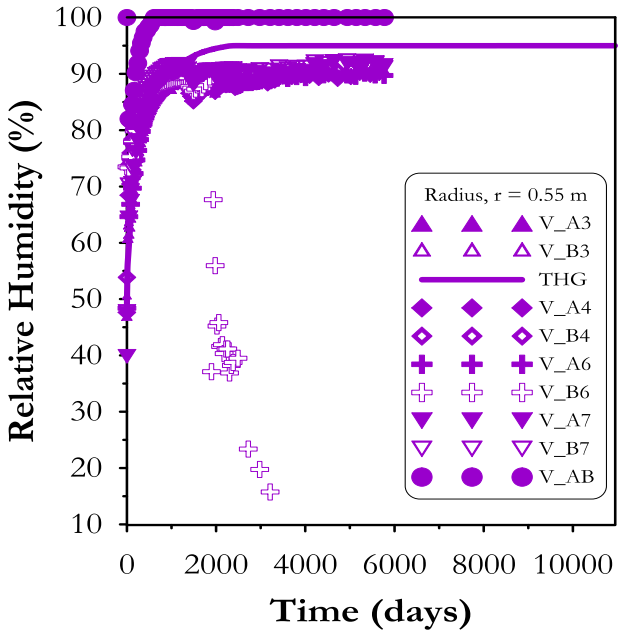

Figure A.12. Evolution of relative humidity for a radius, r = 0.55 m. Measurements (scatter points) and THG model prediction (solid line) up to 10950 days.

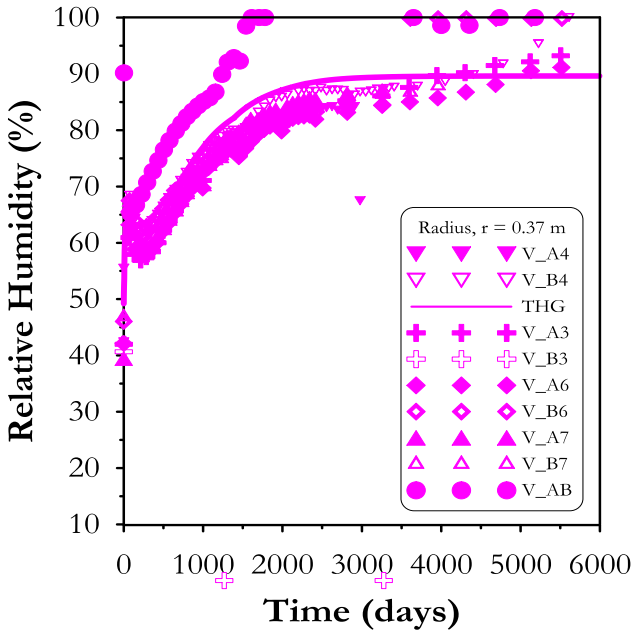

Figure A.13. Evolution of relative humidity for a radius, r = 0.37 m. Measurements (scatter points) and THG model prediction (solid line) up to 6000 days.

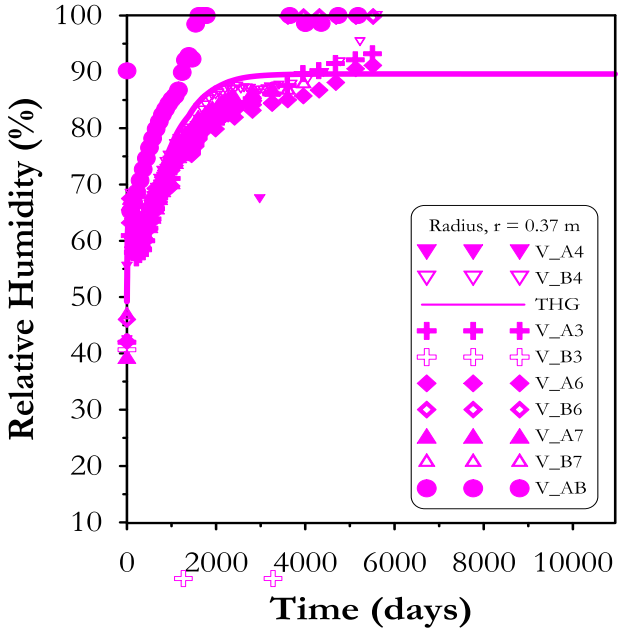

Figure A.14. Evolution of relative humidity for a radius, r = 0.37 m. Measurements (scatter points) and THG model prediction (solid line) up to 10950 days.

Figure A.15 shows the results of relative humidity for sections A3 & B3, A4 & B4, A6 & B6, A7 & B7 and AB corresponding to a radius of 0.22 m from the heater. Figure A.16 presents the long term evolution of relative humidity for the same position up to 10950 days (30 years).

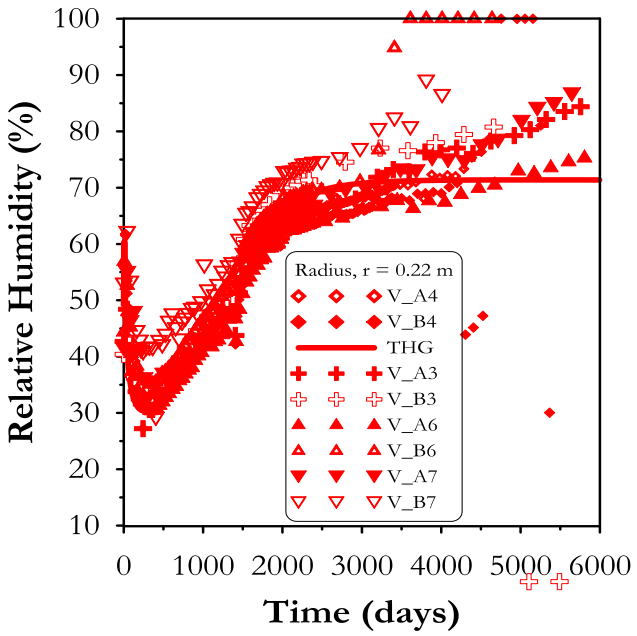

Figure A.15. Evolution of relative humidity for a radius, r = 0.22 m. Measurements (scatter points) and THG model prediction (solid line) up to 6000 days.

In summary, the threshold hydraulic gradient (THG) model predicted quite well the values of relative humidity at all radii. However, the model tends to steady state after 3000 days. This behavior results in an underestimation of the observed values especially the ones measured near the heat source.

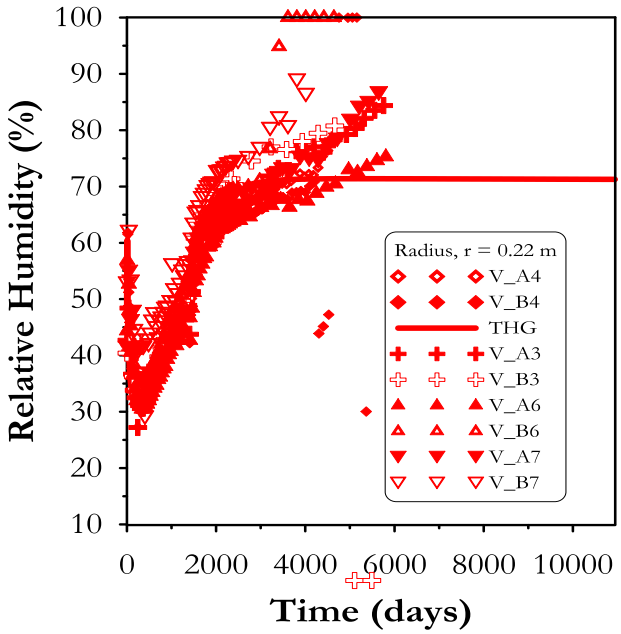

Figure A.16. Evolution of relative humidity for a radius, r = 0.22 m. Measurements (scatter points) and THG model prediction (solid line) up to 10950 days.

A.1.3 Thermo-Osmosis

The following figures show the numerical results of relative humidity obtained with the THO model. Figure A.17 presents the results of relative humidity for sections A3 & B3, A4 & B4, A6 & B6, A7 & B7 and AB corresponding to a radius of 0.70 m from the heater. Figure A.18 shows the long term evolution of relative humidity for the same position up to 10950 days (30 years).

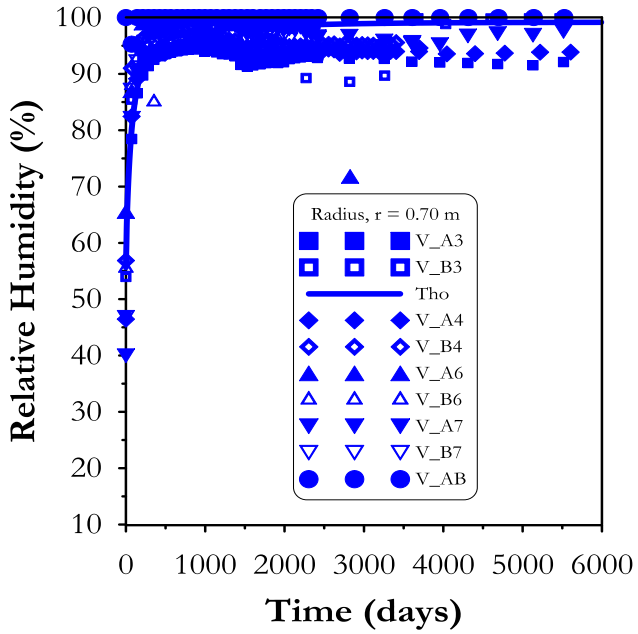

Figure A.17. Evolution of relative humidity for a radius, r = 0.70 m. Measurements (scatter points) and THO model prediction (solid line) up to 6000 days.

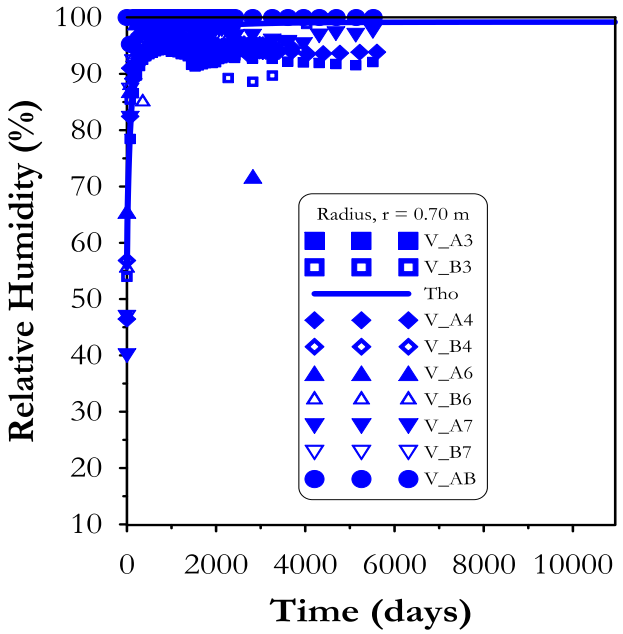

Figure A.18. Evolution of relative humidity for a radius, r = 0.70 m. Measurements (scatter points) and THO model prediction (solid line) up to 10950 days.

Figure A.19 shows the results of relative humidity for sections A3 & B3, A4 & B4, A6 & B6, A7 & B7 and AB corresponding to a radius of 0.55 m from the heater. Figure A.20 presents the long term evolution of relative humidity for the same position up to 10950 days (30 years).

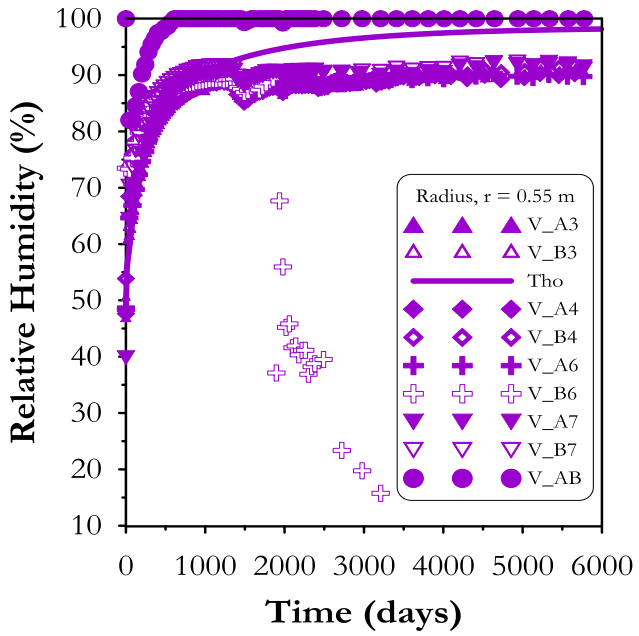

Figure A.19. Evolution of relative humidity for a radius, r = 0.55 m. Measurements (scatter points) and THO model prediction (solid line) up to 6000 days.

The results corresponding to a radius of 0.37 m from the heater are shown in Figure A.21. Figure A.22 shows the long term evolution of relative humidity for the same position up to 10950 days (30 years).

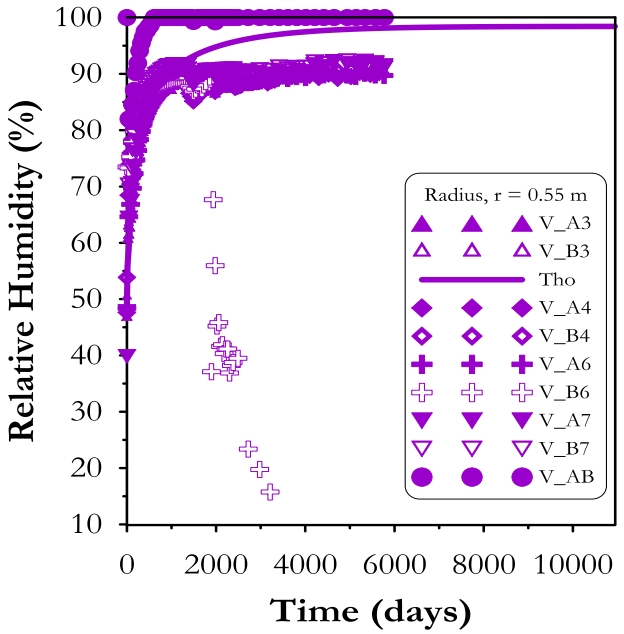

Figure A.20. Evolution of relative humidity for a radius, r = 0.55 m. Measurements (scatter points) and THO model prediction (solid line) up to 10950 days.

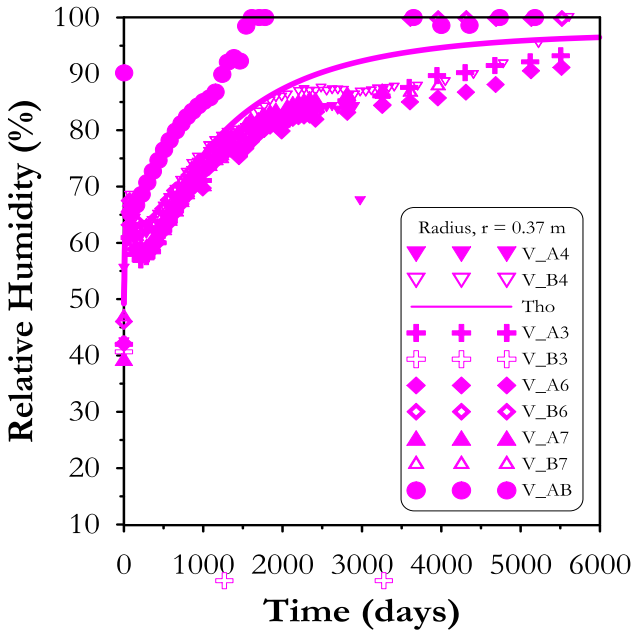

Figure A.21. Evolution of relative humidity for a radius, r = 0.37 m. Measurements (scatter points) and THO model prediction (solid line) up to 6000 days.

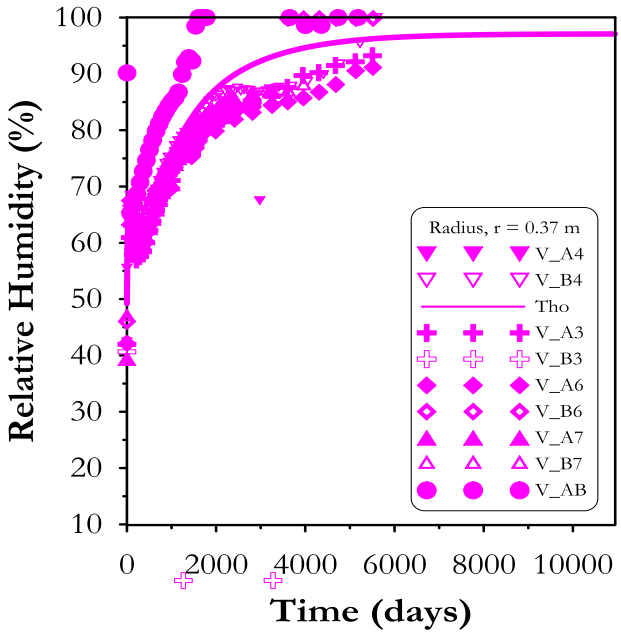

Figure A.22. Evolution of relative humidity for a radius, r = 0.37 m. Measurements (scatter points) and THO model prediction (solid line) up to 10950 days.

Figure A.23 shows the results of relative humidity for sections A3 & B3, A4 & B4, A6 & B6, A7 & B7 and AB corresponding to a radius of 0.22 m from the heater. Figure A.24 presents the long term evolution of relative humidity for the same position up to 10950 days (30 years).

In summary, the thermo-osmosis (THO) model predicted quite well the values of relative humidity at all radii. However, in the long-term, the model overestimates the measurements close to the heater.

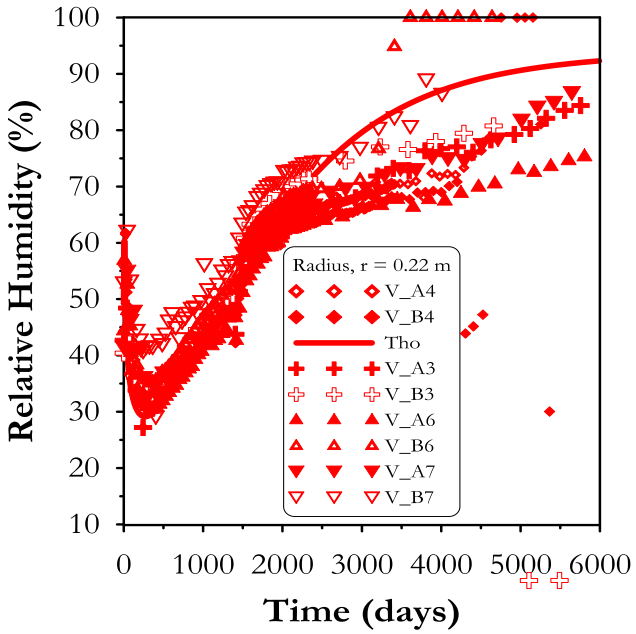

Figure A.23. Evolution of relative humidity for a radius, r = 0.22 m. Measurements (scatter points) and THO model prediction (solid line) up to 6000 days.

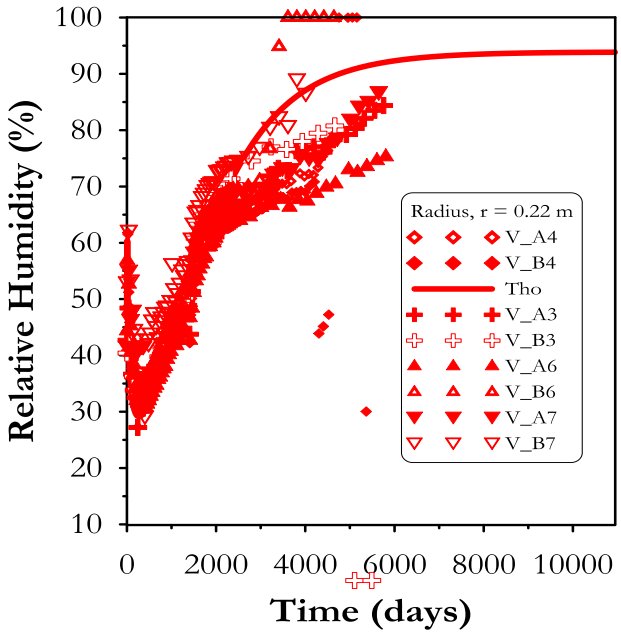

Figure A.24. Evolution of relative humidity for a radius, r = 0.22 m. Measurements (scatter points) and THO model prediction (solid line) up to 10950 days.

A.2 THM Evolution Of An In-Situ Synthetic Case

The following figures show the results of temperature, liquid degree of saturation, liquid pressure and stresses at time 0, 1, 10, 100 and 1000 years for the Operational Base Case (OBC).

Figure A.25. Distribution of temperature along the repository system at time, t = 0 years.

Figure A.26. Distribution of temperature along the repository system at time, t = 1 year.

Figure A.27. Distribution of temperature along the repository system at time, t = 10 years.

Figure A.28. Distribution of temperature along the repository system at time, t = 100 years.

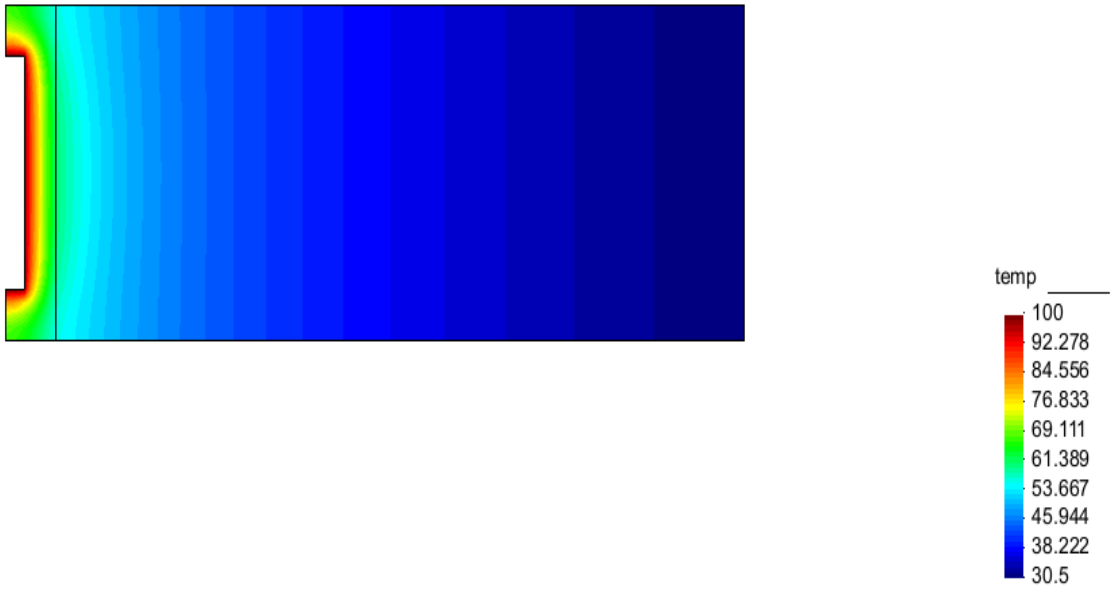

Figure A.29. Distribution of temperature along the repository system at time, t = 1000 years.

Figure A.30. Distribution of liquid degree of saturation along the repository system at time, t = 0 years.

Figure A.31. Distribution of liquid degree of saturation along the repository system at time, t = 1 year.

Figure A.32. Distribution of liquid degree of saturation along the repository system at time, t = 10 years.

Figure A.33. Distribution of liquid degree of saturation along the repository system at time, t = 100 years.

Figure A.34. Distribution of liquid degree of saturation along the repository system at time, t = 1000 years.

Figure A.35. Distribution of liquid pressure along the repository system at time, t = 0 years.

Figure A.36. Distribution of liquid pressure along the repository system at time, t = 1 year.

Figure A.37. Distribution of liquid pressure along the repository system at time, t = 10 years.

Figure A.38. Distribution of liquid pressure along the repository system at time, t = 100 years.

Figure A.39. Distribution of liquid pressure along the repository system at time, t = 1000 years.

Figure A.40. Distribution of normal stress along the repository system at time, t = 0 years.

Figure A.41. Distribution of normal stress along the repository system at time, t = 1 year.

Figure A.42. Distribution of normal stress along the repository system at time, t = 10 years.

Figure A.43. Distribution of normal stress along the repository system at time, t = 100 years.

Figure A.44. Distribution of normal stress along the repository system at time, t = 1000 years.

The following figures show the results of temperature, liquid degree of saturation, liquid pressure and stresses at time 0, 1, 10, 100 and 1000 years for the Thermo-osmosis model (THO).

Figure A.45. Distribution of temperature along the repository system at time, t = 0 years.

Figure A.46. Distribution of temperature along the repository system at time, t = 1 year.

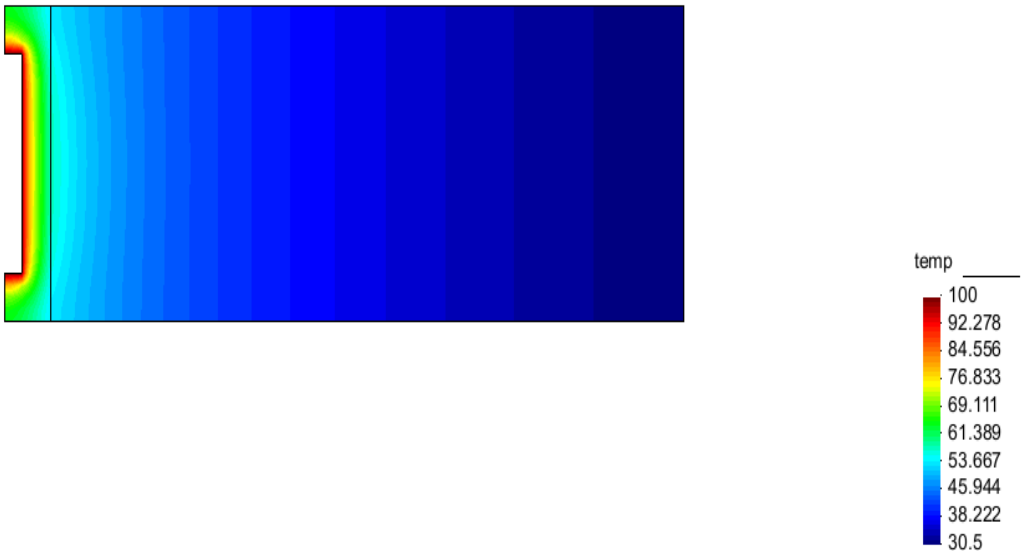

Figure A.47. Distribution of temperature along the repository system at time, t = 10 years.

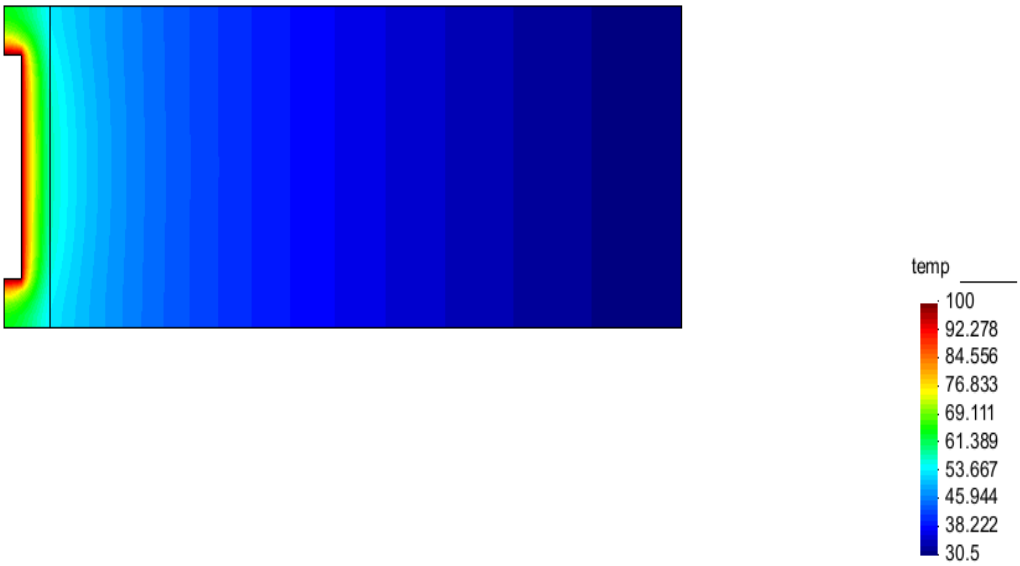

Figure A.48. Distribution of temperature along the repository system at time, t = 100 years.

Figure A.49. Distribution of temperature along the repository system at time, t = 1000 years.

Figure A.50. Distribution of liquid degree of saturation along the repository system at time, t = 0 years.

Figure A.51. Distribution of liquid degree of saturation along the repository system at time, t = 1 year.

Figure A.52. Distribution of liquid degree of saturation along the repository system at time, t = 10 years.

Figure A.53. Distribution of liquid degree of saturation along the repository system at time, t = 100 years.

Figure A.54. Distribution of liquid degree of saturation along the repository system at time, t = 1000 years.

Figure A.55. Distribution of liquid pressure along the repository system at time, t = 0 years.

Figure A.56. Distribution of liquid pressure along the repository system at time, t = 1 year.

Figure A.57. Distribution of liquid pressure along the repository system at time, t = 10 years.

Figure A.58. Distribution of liquid pressure along the repository system at time, t = 100 years.

Figure A.59. Distribution of liquid pressure along the repository system at time, t = 1000 years.

Figure A.60. Distribution of normal stress along the repository system at time, t = 0 years.

Figure A.61. Distribution of normal stress along the repository system at time, t = 1 year.

Figure A.62. Distribution of normal stress along the repository system at time, t = 10 years.

Figure A.63. Distribution of normal stress along the repository system at time, t = 100 years.

Figure A.64. Distribution of normal stress along the repository system at time, t = 1000 years.